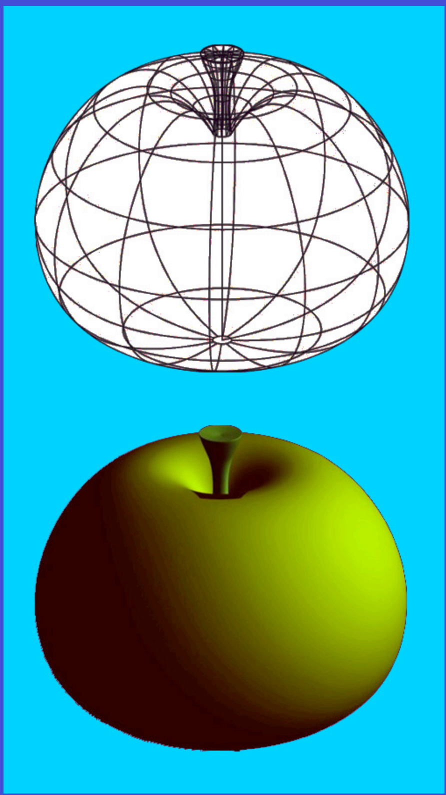

Bureau Gravimétrique International
International Geoid Service
Joint Bulletin

Newton's Bulletin

Issue n°3, December 2005

International Association of Geodesy
and
International Gravity Field Service

ISSN 1810-8555

Summary

Pages

SECTION I - "Reviewed Papers" -

BGI Papers:

IGeS Papers:

A full color issue is available at
http://bgi.cnes.fr:8110 and at http://www.iges.polimi.it/

SECTION I : "Reviewed Papers"

Calibration of a 3-accelerometer inertial gravimetry system for moving gravimetry

B. de Saint-Jean, J. Verdun, H. Duquenne
email : desaintjean@ensg.ign.fr
Institut Géographique National/LAREG, 6/8 av. Blaise Pascal, Champs sur Marne, 77455 Marne la vallée cedex 2, France
J.P. Barriot
Centre National d'Études Spatiales (CNES), 18 av. E. Belin, 31401 Toulouse cedex 9, France
J. Cali
École Supérieure des Géomètres Topographes (ESGT), 1, Bd. Pythagore,72000 Le Mans, France

Abstract. A moving inertial gravimetric system is being developed, consisting of three high precision accelerometers measuring accelerations along three non parallel axes. The signal delivered by each accelerometer is an electric current, the intensity of which is proportional to the acceleration experienced by the test mass of the accelerometric sensor. This sensor is also very sensitive to temperature variations which are continuously monitored by an internal temperature sensor. The current given by each accelerometer is transformed into a voltage sampled at 31.25 Hz, that is one sample every 32 ms, while the temperature is sampled at a rate of one sample every 4.096 s.

Our aim is to carry out the calibration of this system in order to derive the relationship between each digitalized value given by the accelerometers and the actual acceleration, taking into account temperature variations. Our calibration system permits to tilt simultaneously the three accelerometers above a point where gravity has been precisely determined. Thus, the accelerometers can sense any acceleration value between 0 and the value of gravity at the measuring point (accelerometer axis is then vertical).

We discuss the results of the calibration by looking at the residuals between observed values and those coming from different theoretical calibration functions. We particularly focus on the perturbing phenomena such as temperature or misalignment of the sensitive axis.

Keywords. Vector gravimetry, calibration, accelerometers, least squares.

---

1 Introduction

Since about a decade, gravimetry has significantly evolved and several techniques can now be used with different precisions and resolutions (Bruton, 2000). There is however a gap affecting medium resolutions, ranging from 5 to 100 km, which cannot be filled by ground-based gravimetry or space gravimetry (Boedecker, 1994, Verdun et al., 2003). The miniaturization of both accelerometers and GPS receivers made possible the design of small size apparatus for moving gravimetry. Such apparatus are used to cover hard access continental regions like mountains, margins, deserts or rivers like Amazon, with a resolution within the range 5 to 100 km.

Three accelerometers, coupled with a 4-antennae GPS system can be used as a cheap and handy instrument to measure the three spatial components of the gravity vector (vector gravimetry).

Such a gravimetry system is now being developed in our laboratory consisting of three high precision accelerometers (type QA3000-20, Honeywell) supported by a triad. Each accelerometer delivers an electric current, the intensity of which is proportional to the acceleration sensed onto its sensitive axis. The current is then transformed into a voltage which is digitalized at a frequency up to 250 Hz by means of a 24 bits A/D converter. The internal accelerometer temperature is also measured by a sensor, and digitalized with a sampling rate of 0.244 Hz (1 sample every 4.096 s). Our approach consists of finding a calibration procedure in order to estimate the relationship between the actual acceleration value and its digitalized value. The effects of temperature have also to be carefully investigated since the electronic system is likely to be very sensitive to temperature variations.

We develop and discuss in this paper the calibration procedure including the materials and the processing of calibration function. A first calibration carried out in February 2005 is analysed, and a first calibration function is derived. We also propose some recommendations in order to improve the reliability of the calibration procedure.

2 Calibration principle

Deriving the calibration function requires the acquisition of a set of accelerometer data at points where the acceleration has been already measured by means of another method. Our calibration system permits to tilt simultaneously the three accelerometers above a point where gravity has been measured beforehand using an absolute gravimeter. By so doing, each accelerometer can sense any acceleration value between 0 (accelerometer sensitive axis is horizontal) and the gravity value at the point (980 855.8 mGal).

Indeed, if the accelerometer is tilted by an angle *α* from the vertical (fig. 1), the accelerometer measurement F consists of the projection of gravity vector $\vec{g}_{\text{abs}}$ onto its sensitive axis, that is

$$F = g_{\text{abs}} * \cos(\alpha - \beta) \qquad (1)$$

where *β* is the projection of *θ* (the angle between the geometric axis and the sensitive axis of the accelerometer) on the plan of *α* formed between the geometric axis of the mirror and the sensitive axis of the accelerometer (fig. 2).

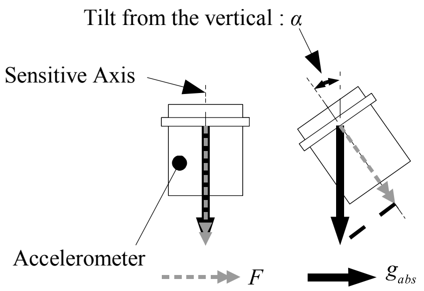

Fig. 1 Tilt of accelerometer sensitive axis

The angle *θ* is designed by the manufacturer to be less than 1 mrad. As a first approximation, we chose to neglect this angle because so far measurements for calibration do not permit to define this angle. So, the sensitive axis is assumed to be aligned with the geometric axis of each accelerometer. Let *Dz* be the zenithal distance of the accelerometer axis (fig. 2), then we obtain

$$F = -g_{\text{abs}} * \cos(Dz) \quad . \qquad (2)$$

Equation (2) allows to determine the acceleration *F* sensed by each accelerometer for any zenithal distance *Dz*. In the meantime, the A/D converter provides the digitalized value *Ng* of the acceleration *F*. Our aim is now to obtain, for each accelerometer, a set of N observations (Ng_i , F_i), $i=1,...,N$, in order to estimate the calibration function

$$Am = f_T(Ng) \qquad (3)$$

of each accelerometer, for a given temperature.

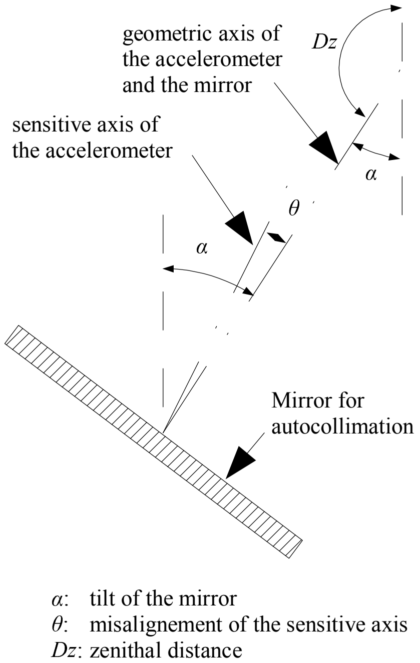

Fig. 2 Measurement of *Dz*

3 Practical determination of acceleration *F*

The three accelerometers are mounted on a platform which can rotate around a horizontal axis, and enclosed in a thermally isolated box where temperature is maintained constant. The platform's rotation is controlled by a screw which can be overtightened in order to maintain the platform in a fixed direction. The platform is also equipped with a mirror placed outside the isolated box by means of an axis. The axes of respectively the mirror and the three accelerometers have been previously yielded parallel by autocollimation with an optical plummet. By so doing, the zenithal distance of the mirror axis corresponds exactly to the geometrical axes of the three accelerometers. The zenithal distance can then be precisely measured by means of autocollimation using a theodolite.

4 Result of the calibration

The calibration was carried out in the laboratory of ESGT (Ecole Supérieure des Géomètres et Topographes) during two days.

4.1 Acceleration measurements and precision

Accelerations were measured for about 20 zenithal distances *Dz* ranging from 109° to 140°, and for two different temperatures. We systematically acquired about 15 measurements for each zenithal distance, so as to estimate the standard deviation σ_{Dz}. Then, assuming that the errors on *Dz* and g_{abs} are uncorrelated, and the error on g_{abs} is negligible, the standard deviation σ_{Am} of *F* can be calculated as:

$$\sigma_{Am} = g_{\text{abs}} |\sin(Dz)| \sigma_{Dz} \quad . \tag{4}$$

The resulting standard deviations have proved to range between 0.8 mGal and 4.5 mGal with a median at 2.1 mGal.

4.2 Digitalizing of accelerations and precision

For a given tilt, acceleration was continuously digitalized with a sampling rate of 31.25 Hz, i.e. one sample every 32 ms. By so doing, we acquired on average 80 digitalized values *Ng* of *F* for each measurement at zenithal distance *Dz*. As a result, using 15 zenithal distance measurements, we obtained 15 * 80 = 1200 digitalized values *Ng* of the same acceleration. The standard deviations of the digitalized acceleration mean values range between 0.5 and 2.5 bits with a median at 1.0 bit. Given the fact that accelerometers range extends over 4 *g* (±*2 g*), coded on 24 bits, the resulting resolution is given by:

$$\frac{4 \times 10 \times 10^5}{2^{24}} = 0.24 \quad mGal/bit$$

These findings indicate that the errors on digitalized acceleration values cause an error on acceleration ranging between 0.12 mGal and 0.60 mGal.

The synchronisation of both the theodolite and the A/D converter was ensured by means of GPS time delivered by a dedicated GPS receiver.

5 Estimation of the calibration function

Following the manufacturer recommendation, the calibration function for a given temperature has to be chosen as a polynomial function. Since the temperature does not vary very much and the range of accelerations is not wide, we chose a first order polynomial function as a model:

$$f_T(Ng) = b + k\, Ng \tag{5}$$

where *b* and *k* are the bias and the scale factor of the calibration function, respectively.

Let b^0 and k^0 be approximate values of parameters b and k, then the calibration function for each observation (Dz_i , Ng_i) may be expressed as

$$g \cos(Dz_i + v_{Dz_i}) + (b^0 + \Delta b) + (k^0 + \Delta k)(Ng_i + v_{Ng_i}) = 0 \tag{6}$$

where v_{Dzi} and v_{Ngi} correspond to the residuals of the observations Dz_i and Ng_i, respectively, and Δb, Δk are the correction to be applied to the parameters *b* and *k*. By keeping only first order terms in the previous equation, we obtain

$$\begin{aligned} & g\cos(Dz_i) - g\sin(Dz_i)\, v_{Dz_i} \\ & \quad + b^0 + \Delta b + k^0\, Ng_i + Ng_i \Delta k + k^0\, v_{Ng_i} = 0 \end{aligned} \tag{7}$$

By denoting

$$A = \begin{bmatrix} \vdots & \vdots \\ 1 & Ng_i \\ \vdots & \vdots \end{bmatrix},\ X = \begin{bmatrix} \Delta b \\ \Delta k \end{bmatrix},\ W = \begin{bmatrix} \vdots \\ g\cos Dz_i + b^0 + k^0\, Ng_i \\ \vdots \end{bmatrix}$$

$$V = \begin{bmatrix} \vdots \\ -g\sin Dz_i\, v_{Dz_i} + k^0 \;\; v_{Ng_i} \\ \vdots \end{bmatrix} \tag{8}$$

equation 7 can be rewritten in matrix form as

$$W + V + A\,X = 0 \tag{9}$$

Estimates for *b* and *k* parameters can be found by means of the least squares method which consists in minimizing the quadratic form

$$\Phi(V, \Lambda, X) = V^T P_V V - 2\ \Lambda^T (W + V + A\,X) \tag{10}$$

where P_V is the weight matrix of residual vector V and Λ is the vector of Lagrange's multipliers. The solution can be easily determined using the following relations (Leick, 1990)

$$
\begin{aligned}
X &= -(A^T P_V A)^{-1} A^T P_V W \\
\Lambda &= -P_V (W + A X) \\
V &= P_V^{-1} \Lambda
\end{aligned}
\tag{11}
$$

The variance-covariance matrix of the parameters is the given by

$$C_X = (A^T P_V A)^{-1} \tag{12}$$

The weight matrix P_V can be deduced from the Cv covariance matrix of vector $V = [v_{Dz}^T, v_{Ng}^T]^T$ by (Fotopoulos, 2005)

$$P_V = (E\,Cv\,E^T)^{-1} \quad with$$

$$
Cv = \begin{bmatrix}
\sigma_{v_{Dz_1}} & & & & & \\
& \ddots & & & (0) & \\
& & \sigma_{v_{Dz_N}} & & & \\
& & & \sigma_{v_{Ng_1}} & & \\
& (0) & & & \ddots & \\
& & & & & \sigma_{v_{Ng_1}}
\end{bmatrix}
\tag{13}
$$

$$
E = \begin{bmatrix}
-g\sin(Dz_1) & & & -k^0 & & \\
& \ddots & & & \ddots & \\
& & -g\sin(Dz_N) & & & -k^0
\end{bmatrix}
$$

σ_{Dz_i} and σ_{Ng_i} for $i=1,..,N$ can be estimated from the measurements described in § 4.1 and 4.2. The above-mentioned calculation can be performed by iteration starting from an arbitrary solution (b_0 , k_0) and testing the sum of squared normalized residuals $V^T P_V V$.

The results obtained for our two-days calibration are tabulated in table 1 for two different temperatures (24.8°C for the first day and 31.0°C for the second).

Table 1 Results of least squares estimation ; the second accelerometer was disconnected during the 2nd day

		b	k	σb	σk	So
		mgal	mgal/kbit	mgal	mgal/Mbit	mgal
Day 1	acc. 1	-29497.03	243.05	4.58	1.83	0.03
222 values	acc. 2	-34476.42	241.77	4.62	1.82	0.03
T°=24.8°C	acc. 3	-23802.24	242.20	4.55	1.83	0.07
Day 2	acc. 1	-29410.07	242.85	2.31	0.95	0.03
413 values	acc. 2	---	---	---	---	---
T°= 31.0°C	acc. 3	-24061.45	242.18	2.29	0.95	0.24

The relative uncertainties on the bias are very small, which gives confidence in its determination. The scale factor has proved to be nearly constant (variation less than 2 mGal/kbits) for all accelerometers and all temperatures which confirms of the reliability of the accelerometer for tracking acceleration variations. The results suggest that the bias might increase with the temperature, which has to be validated by exploring a wider range of temperatures.

6 Conclusions

The calibration procedure proved to be very efficient to estimate the calibration functions of each individual accelerometer. But, the misalignment θ and its direction cannot be defined with this calibration process. Further experiments have to be held in order to determine this angle.

The bias is likely to be significantly influenced by the temperature variations ; thus some additional experiments have to be carried out in order to explore a wider temperature range.

Clearly more work needs to be done particularly in testing higher order calibration functions.

References

Boedecker, G., Leismüller, F., Spohnholtz, T., Cuno, J., and Neumayer, K. H. (1994). Accelerometer / gps integration for strapdown airborne gravimetry : First test results. In Sunkel, H. and Marson, I., editors, *Gravity and Geoid – IAG Symposium*, volume 113, pages 177–186. Springer.

Bruton, M. A. (2000). *Improving the Accuracy and Resolution of SINS/DGPS Airborne Gravimetry*. PhD thesis, University of Calgary.

Fotopoulos, G. (2005). Calibration of geoid error models via a combined adjustment of ellipsoidal, orthometric geoid height data. *Journal of Geodesy*, 79 :11-123.

Leick, A. (1990). *GPS Satellite Surveying* John Wiley and Sons (Eds).

Verdun, J., Klingelé, E., Bayer, R., Cocard, M., Geiger, A., and Kahle, H.-G. (2003). The Alpine Swiss-French airborne gravity survey. *Geophysical Journal International*, 152 :8–19.

Application of a least square spectral filter in correcting abnormal meteorological drift of a LaCoste-Romberg Gravimeter

Okechukwu K, Nwofor and T Chidiezie, Chineke

Department of physics, Imo State University, P.M.B 2000 Owerri, Nigeria

ABSTRACT

The performance of a least square spectral filter in removing abnormal meteorological drifting earlier reported for a Lacoste-Romberg gravimeter is evaluated. A short (3-days) drift curve of the instrument was compared with tidal data for the location that is derived from theoretical Earth parameters before and after application of the filter. The filter was effective in remove noise registrations above 4 cycles per day in the gravimeter record. A large amplitude disparity at frequencies < 2 cycles per day between the two time series were found after application of the filter. This is attributed to temperature induced creeps in the meter spring, which resulted in phase shifts in the gravimeter series. It is concluded that a combination of "Optimum Operating Procedures" as earlier published and appropriate filtering and phase adjustments may increase gravimeter precision for measurements requiring mGal accuracy. μGal precision data would however require instruments with better temperature compensation. The procedure presented here is suggested for routine assessment of gravimeter precisions prior to field deployment, against the background of scarcity of new gravimeters for fieldwork in Nigeria.

Key words: *Spectral filter, least square, LCR gravimeter, meteorological drift, and synthetic Earth tide.*

1.0 INTRODUCTION

The Lacoste Romberg (LCR) gravimeter is useful in mapping geologic structures of anomalous densities associated with ore and hydrocarbon accumulation (Ojo, 1992). In geodesy, it is useful in the monitoring of elevation changes (Woollard, 1980) and surface deformations (Kiviniemi, 1974); and in geodynamics for monitoring tectonic stresses (Honkassalo, 1975). One of the major advantages in using the Lacoste-Romberg gravimeter for fieldwork is that it records minimal drift when stationary. This facility is reduced as a consequence of aging and mechanical faults, (Osazuwa & Ajakaiye, 1982; Nwofor, 1994; Nwofor & Chineke, 2003). Since the few available LCR gravimeters in Nigeria are mostly very old and as such have lost most of the in-built compensations making them highly susceptible to meteorological effects. There is the need to continue to assess the reliability of the available instruments for various applications. Since synthetic tides of the Earth can be determined to a very high level of precision (such as nano-Gals), via software: (http://www.gik.uni-karlsruhe.de/Forschung/eterna33.htm), one of the problems presently encountered is to measure to this accuracy using instruments. Synthetic Earth tide data can therefore provide a facility for routine investigation of abnormal drifting of a gravimeter. This work introduces this method. It involves the comparison of a short series of ground based gravity tidal observation of a LaCoste-Romberg gravimeter in Jos Nigeria with a synthetic tide derived from wave groups that are based on theoretical Earth parameters. The LCR gravimeter is among the very old ones commonly found in the country whose several compensations were suspect, making it highly susceptible to meteorological influences. "Optimum Operating Principles" for reducing these impacts some of which can interfere in the tidal band, have been studied for the system as reported by Nwofor and Chineke (2003). The present method is an appraisal of the effectiveness a low pass least square filter in reducing these abnormal drifts.

2. 0 METHODS

The gravimeter tide is a 72 hours ground based data beginning at 08,30 hours local time (UTC) on October 10, 1992, obtained with a LaCoste Romberg (LCR) using the optical method. The gravimeter model G.468 was positioned in Jos, Nigeria at a longitude of 8^{o} 53' E, latitude of 9^{o} 57' N, elevation of 1159 meters above sea level (Macleod et al., 1971); and about 1000 km from the southern coastline. The gravimeter measures to 1 part in 100 million or 0.01 mGal (1 mGal $=10^{-5}$ ms^{-2}), which suites the limit of sensitivity for the major tides, if instrumental and interference errors are removed. Two major errors are however encountered with the use of the instrument. The first is due to spring response to dial turns which may not be simply accurate and the other due to spring hysteresis. This second error type is easily associated to loading, aging and meteorological effects.

The gravimeter tidal record is superimposed on the linear drift, which agrees in value with the normal specification (0.0079 mGals/hour) (figure 1). The amplitudes h of the gravimeter series were then obtained by fitting a linear trend d to the gravimeter readings G according to the equation

$$h = G - d \qquad (1)$$

Fig. 1a

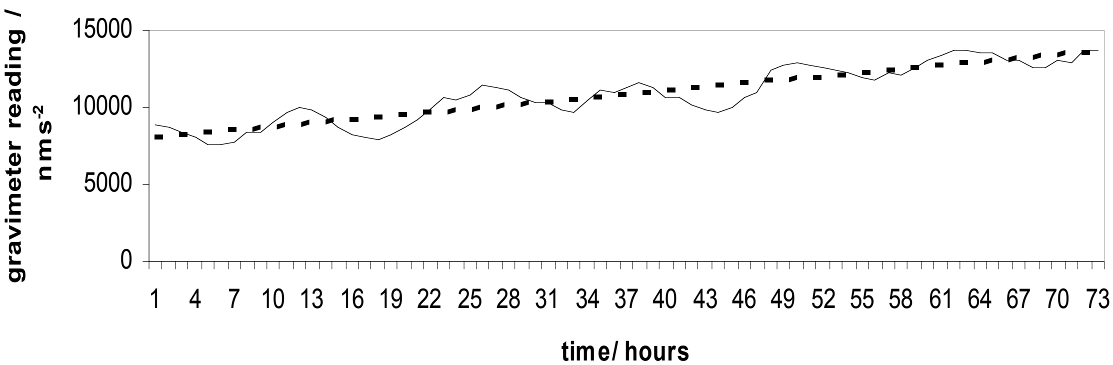

Fig 1b

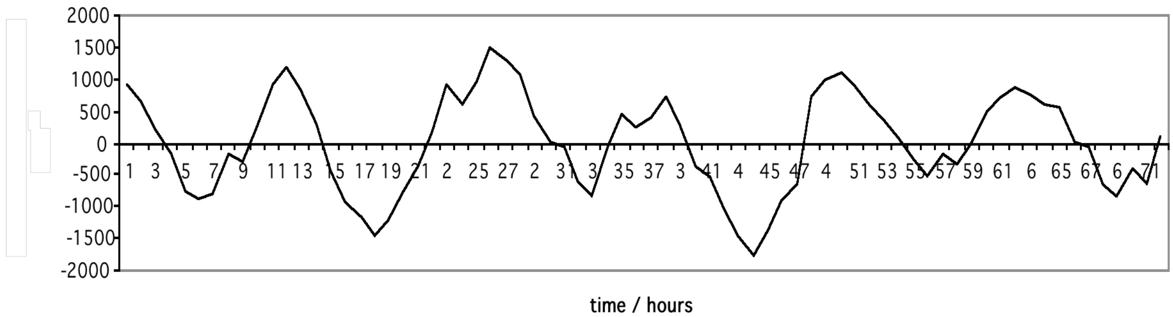

Figure 1: (a) Observed gravimeter drift (solid lines) with fitted linear trend (dashed lines)

(b) Gravimeter drift corrected for linear trend trend

The gravimeter data has a high signal to noise ratio, and therefore required appropriate filtering. Some criteria for choosing frequencies to be removed have been explained by Mishra and Rao (1997). In their work, temporal variations in the gravity field recorded at a station were classified into six major types; very large period (100 – 10000 years); large period (10 – 100 years); medium period (days – years); short period (hours – days); shorter period (hours) and shortest period (seconds – minutes). In the present case the noise registrations are obviously shorter period events, which are found to be mainly meteorological i.e. changes in atmospheric pressure (Durcame et al., 1999) and perhaps fluctuations in the tropical temperatures (Nwofor 1994, Nwofor and Chineke, 2003).

We applied a low pass least square filter at a cut off frequency of 4 cycles per day in other to preserve signals in the tidal band. The filter is implemented in the model tide programme Tsoft (Van Camp &

Vauterin, (2005)) which was also used to compute the synthetic tide for the station using a wave group table.

The Least Square Spectral Filter (LSSF) is found to be particularly suitable for the data series. This is because the Discrete Fourier Transform (DFT), which is an alternative (Scales, 1997), may not be suitable for analyzing data with gaps in the series (Vanicek, 1971), and is generally not convenient for short data series since it assumes signals to be limited in both time and frequency (Ozaktas et al., 1996). Algorithms for implementing the DFT such as The Fast Fourier Transform (FFT) are equally inappropriate, as these do not estimate DFT with high accuracy (Becker and Morrison, 1996). Unlike the DFT and FFT, the LSSF, models short periodicities that contain periodic or systematic signals, which may contain either random or systematic errors or both (Vanicek, 1971). The performance of this filter in removing the interference effects in the gravimeter data is deduced from comparison of the spectral series for the gravimeter drift contaminated with noise (figure 2a), the filtered gravimeter tides (figure 2b) and the synthetic tide (Figure 2c). The outputs of the filter for figures 2b and 2c are similar. Noise registrations, above the white noise threshold are minimized by application of the filter.

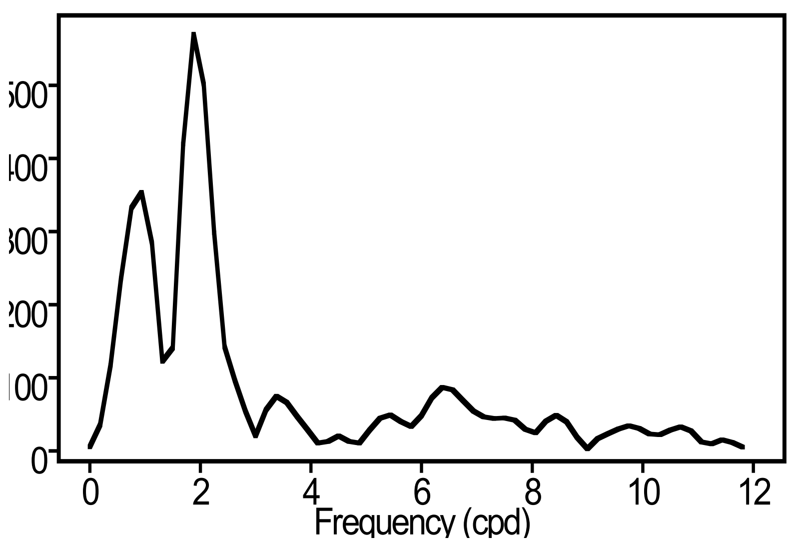

Figure 2 a: Spectrum of gravimeter drift before application of the LSSF showing high frequency noise registrations

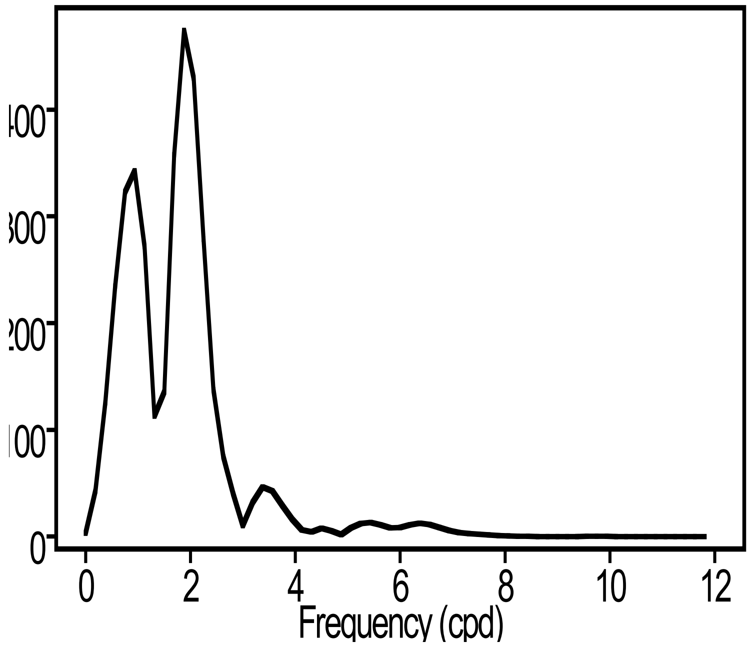

Figure 2b: Spectrum of gravimeter drift after application of the LSSSF

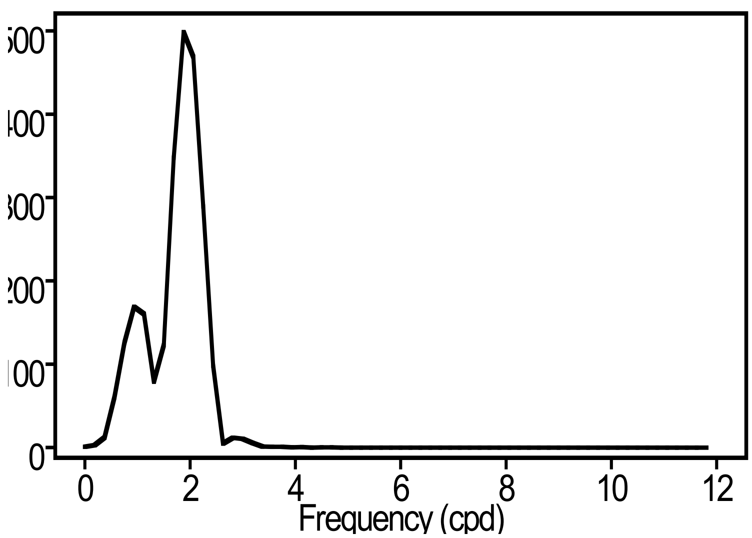

Figure2c: Spectrum of the synthetic tide

3.0 DATA ANALYSIS AND DISCUSSIONS

A rough comparison of some of the properties of the gravimeter and synthetic tide series is carried out in *table 1* to test the assumption of linearity in the propagation of the two tides. The properties are the periodicity, and the amplitude and phase evolution ratios in the two data series. Where the ratios are evaluated for the i^{th} crest to the preceding (ith – 1) crest. For the amplitudes these are given as

$$\frac{h_i}{h_{i-1}};\frac{H_i}{H_{i-1}} \tag{2}$$

Where h and H stand for the amplitudes of the gravimeter and synthetic tides respectively. And for the phases as

$$\frac{\Phi_{hi}}{\Phi_{hi-1}};\frac{\Phi_{Hi}}{\Phi_{Hi-1}} \tag{3}$$

Where Φ_h and Φ_H are the phases for the gravimeter and synthetic tides respectively. With Φ_H - Φ_h defined as the phase shift and h /H, the amplification. (Amplitude increase of gravimeter series over the synthetic series).

The amplitudes and phase evolution of the series have been evaluated using the highest and the lowest points of the envelopes in the filtered data and the shift is assessed from the correlation. (Figure 3)

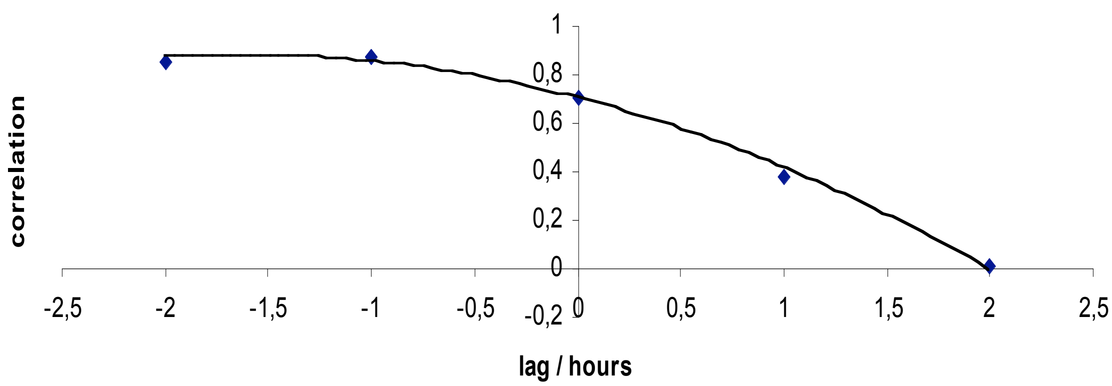

Figure 3: Correlation between gravimeter and synthetic tides for different time lags(hours)

Table 1: *Comparison of period, amplitude and phase evolution ratios of the gravimeter and synthetic tides*.

	Gravimetric tide	Synthetic tide	Discrepancy
Average period (hours)	1180	11.80	0
Average amplitude evolution ratios	0.980	1.000	0.02
Average phase evolution ratios	1.04	1.05	0.01

The amplitude and phase ratios for the two series are close from Table 1. Hence there is a marked linearity in the evolution of the two tides. Based on this established linearity we determined the lag in hours by calculating the cross correlation coefficients at different adjusted values of the time lag, taking the point of maximum correlation to imply zero lag (based on the linearity test) between the two tides (with the synthetic tide taken as reference), i.e. we correlated *H (t)* and *h (t + lag)*. Figure 3 is a plot of the correlations calculated for different lags. Since the data points were sampled at 1-hour intervals, a second-order polynomial ($0.0676\ t^2 + 0.288t + 0.7011$), where t is the lag/ hours, which fitted the correlation curve properly, enables a more precise determination of the points of maximum correlation (at the turning point of the curve). This we found to be at a time lag of about 1.4 hours. Indicating that the gravimeter tide propagates with a time lag of about 1.4 hours behind the synthetic tide. This of course introduces a phase lag of $-\Omega t_0$, ($\sim 43^0$) for the gravimeter series with respect to the synthetic tide, where Ω is the frequency ($\Omega = 2\pi/T$; T = period in hours) and t_0 the time lag. The amplitude variations given by the residuals (*h-H)* are also remarkable. They are higher by over 50% when the time lags in the tides are not corrected (Figure 4), than when they are adjusted for lag even only slightly (figure 5). Figure 5 is a lag-adjustment of only 1 hour, since data was sampled at 1-hour intervals. This is less than the optimum lag-shift by 0.4 hours, but shows the effect of the shift in reducing the residual amplitudes.

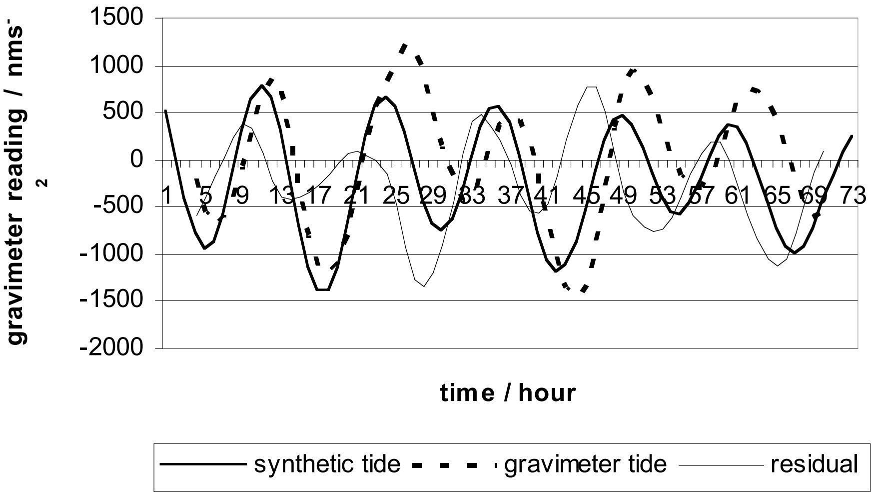

Figure 4: Comparison of gravimeter record with the synthetic tide

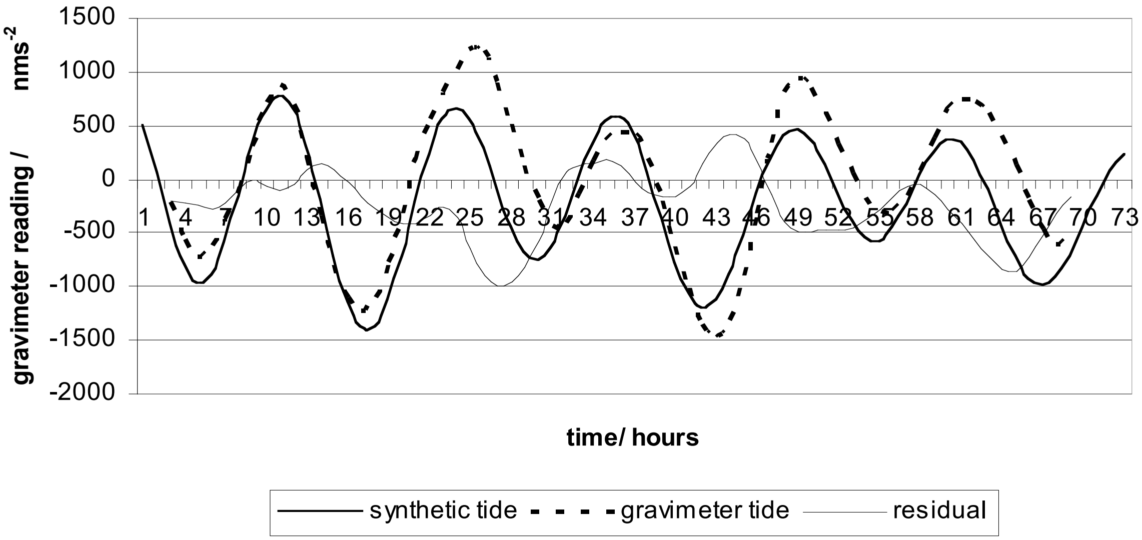

Figure 5: The two time series corrected for time lag by 1 hour and the residuals

3.1 Comments on the Amplitude Disparity

The amplification in the gravimeter data with respect to the synthetic tide has an average value of 0.65. Examination of the spectra for the gravimeter and synthetic tides (fig 4 & 5) indicates that the observed tide has more energy than the synthetic tide in all the frequencies represented. The broadening in the tidal band in the gravimeter spectrum especially between 2 and 4 cycles/day may imply at first sight that more wave groups are contained in the gravimeter series but this is most unlikely. Rather a meteorological artifact, most likely temperature is a strong factor that increased the gravimeter spectral response in the tidal band. A temperature-induced systematic response of the spring is by far the closest periodic signal that can fit this behavior. It shows evidence of growth with time.

3.2 Comments on the Phase Lag

Astatised spring gravimeters such as the LCR gravimeter are known to record appreciable amplitude damping and instrumental phase shift between the gravity sensor and the recording unit (Melchior, 1983; Torge, 1989). For short-time (< 1 day) tidal spectrum, Torge (1989) has reported damping factors of 0.995 for the semidiurnal (m^2) tidal wave and 1^0 and more for the phase lag. This is much lower than the value we observed. The observed maximum cross correlation at lag 1.04 hr indicates a hysteresis response of the gravimeter. A temperature based systematic error component is therefore the most likely explanation for this creeping behavior.

4.0 CONCLUSIONS

The drift patterns of an old LCR gravimeter have been studied at a location in Nigeria to ascertain the reliability of applying a LSSF for reducing abnormal drifting. Our results show a phase lag of the gravimeter record as compared to an appropriate synthetic data due to instrumental response to temperature changes. These resulted in very spurious signals that may limit the use of the instrument for high precision work and tidal studies. Since surveying and static gravity observations require accuracies of ~ 1mGal, this study implies that a LaCoste Romberg gravimeter that looses its temperature compensation may be used under controlled conditions and with appropriate temperature modeling for monitoring static gravity. It is however apparent that such precautions are over simplifications, when the instrument is to be applied for monitoring geodynamic phenomena requiring higher precision (μGal). For this second use there would be need for instruments with better temperature compensations, perhaps new ones. The method adopted here is a fast way of to test the LCR gravimeter response prior to field deployment. It does not represent a study of tidal phenomena owing to the short period of the time series used.

ACKNOWLEDGEMENTS

This work was concluded during the authors' research visit at the Abdus Salam International Center for Theoretical Physics, Trieste Italy. The authors are grateful to Professor D.E. Ajakaiye, formally of the University of Jos, Nigeria for providing the LCR gravimeter used for this study.

REFERENCES

Becker R I and Morrison N (1996) The errors in the FFT estimation of the Fourier Transform. *IEEE transactions on signal processing,* Vol **44,** No 8, pp 2073-2077.

Durcame B, Sun H P, d'Oreye N, Van Ruymbeke M, Menajara I, (1999) Interpretation of the tidal residuals during the 11 July 1991 total solar eclipse. *Journal of Geodesy,* **73**,2, 53-55, 119 – 2357.

Honkassalo T (1975) Report on the application of geodetic measurements in the determination of recent crustal movements in Finland. *Tectonophysics,* **29,** Netherlands.

Kiviniemi A (1974) High precision measurements for studying the secular variations of Gravity in Finland. Publications of the Finnish Geodetic Institute, No **60**, Helsinki.

Macleod W, Turner D, Wright E (1971) The geology of the Jos plateau, *Geological Survey of Nigeria bulletin*, Vol **1,** No 32, pp 2 – 6.

Melchior P (1983) *The Tides of the Planet Earth*. Second Edition. Pergamon London, pp 10 – 20.

Mishra DC and Rao MBS (1997) Temporal variations in gravity field during solar eclipse on 24 October 1995. *Current science,* **72** (11) (763).

Nwofor O K (1994) *An experimental study of some factors affecting precision gravimetry using the Lacoste Romberg gravimeter*. Unpublished MSc thesis university of Jos Nigeria.

Nwofor O K and Chineke T C (2003) Abnormal temperature- drift responses of LaCoste Romberg gravimeter and procedures in the tropical utilization. *Newton's bulletin,* Vol **1,** No 1 (http: bgi.cnes.fr: 8110/bgi.iges, html).

Ojo S. B (1994) Applications of Gravity method in Groundwater and mineral Exploration and the study of crustal Deformation, Tectonics and d Geodynamics. Proceedings of an International Research Workshop on physics of the solid Earth with special Reference to gravimetry, held in Jos – Nigeria May 19-21 (1992).

Osazuwa I.B and Ajakaiye D.E (1982) The effect of chamber temperature variations on a Lacoste-Romberg gravity meter. Nigerian *Journal of mining and geology,* Vol **19,** No1, pp 261-271.

Ozaktas H.M, Arikan, O Kutlay A, and Bozdagi G (1996) Digital computation of the fractal Fourier Transform**.** *IEEE transactions on signal processing,* Vol **44,** No 9, pp 2141-2150.

Scales J A (1997) *Theory of Seismic Imaging*. Samizdat Press, Center for wave Phenomena, Department of Geophysics Colorado School of Mines. White River Junction Vermont, 05001.

Torge W (1989) *Gravimetry*. Publ. Walter deGruyter Berlin. P 371.

Vanicek P (1971) Further development and properties of the spectral Analysis by least squares fit. *Astrophys. space. Sci,* **12,** 10-33.

Van Camp M and Vauterin P (2005) Tsoft: Graphical and interactive software for the analysis of time series and Earth tides. Computers and Geosciences, 31(5), 631-640, 2005

Woollard G (1980) Crustal structure from gravity and seismic measurements *Journ. of Geophys Research,* Vol **64,** No 16, pp 1521-1543.

A gravimetric quasi-geoid evaluation in the Northern region of Algeria using EGM96 and GPS/Levelling

Mohamed Aissa MESLEM

Laboratory of geodesy
Department of Research and Development
National Institute of Cartography and Remote Sensing
123, Rue de Tripoli, BP 430, Hussein Dey, Algiers, Algeria

Abstract

The use of GPS for the estimation of orthometric heights in a given region, with the help of existing levelling data requires the determination of a local geoid and the bias between the local levelling and the one implicitly defined when the geoid is calculated which is generally based on the gravity anomalies data. The heights of new data can be collected swiftly without using the orthometric heights from levelling; it is what one calls commonly levelling by GPS.

In this framework, the Least Squares Collocation method (LSC) has been used to evaluate the quality of the available GPS-Levelling data, to determine a gravimetric geoid in the North region of Algeria and to estimate the constant datum bias.

The data used in the setting of this study are: The geopotential model EGM96, a total number of 2534 gravity anomalies, as well as 43 GPS points connected to the geodetic network levelling present on the whole North part of Algerian.

Keywords: Least Squares Collocation, GPS-Levelling, gravimetric Data, local geoid.

1. Introduction.

The use of the GPS for the determination of the orthometric heights in regions where the levelling exist requires the determination of a local geoid and the estimation of the height constant bias between the gravimetric datum and local levelling since the local geoid will have its own zero level, whereas the data of levelling can be local, or national.

The bias constant is estimated while calculating the mean of discrepancies between the differences of the GPS-Levelling and geoid. However, these values can have some irregularities in the spatial distribution; we must therefore counterbalance these discrepancies while taking in account their spatial correlations, this problem can be handled by the use of the Least Squares Collocation method (LSC).

In the present paper this work is described by the use of the available data in Northern Algeria spreads from 32° in 37° N in Latitude and -4° in 10° E in Longitude.

The main problem in this region is the one of the quality of the gravity data used and of GPS-Levelling. It has been necessary to withdraw the erroneous gravity values and to make a selection of GPS-Levelling points after a comparison between the observed values and those predicted by gravity.

2. Gravity data and GPS-Levelling.

In practice, when one determine a gravimetric geoid locally, one must represent the neighbourhood of the gravity field by the use of a geopotential model of superior degree and order, in our case of study the harmonic spherical EGM96 has been used. Its contribution must be subtracted from the local data and must be restored thereafter.

During the realization of this work, the only gravity data that were available were those provided by the International Gravimetric Bureau (BGI). We withdrew from the data file the duplicated gravity values as well as those appeared doubtful.

As Digital Elevation Model (DTM), we had used the GTOPO30, the thinnest DTM that was available, of 1kmx1km resolution.

43 GPS-Levelling points with accuracy of ±50 cm have been used; these points have the advantage to be well distributed on the zone of study, however after a comparison between the observed values and those predicted by gravity, some points gave a difference up to the doorstep fixed beforehand according to the accuracy of the GPS-Levelling and the density of points. These points have been rejected before redoing another comparison.

The EGM96contribution has been subtracted from the local gravity data. The statistics of the differences are presented in the table1.

Table 1. Statistics of the EGM96 contribution on the 2534 free air anomalies.

mGal	Mean	Std. Deviation
Observations	**28.77**	**30.18**
EGM96	**34.14**	**23.90**
Differences	**-5.37**	**23.64**

A substantial agreement between EGM96 and the local gravity data have been obtained.

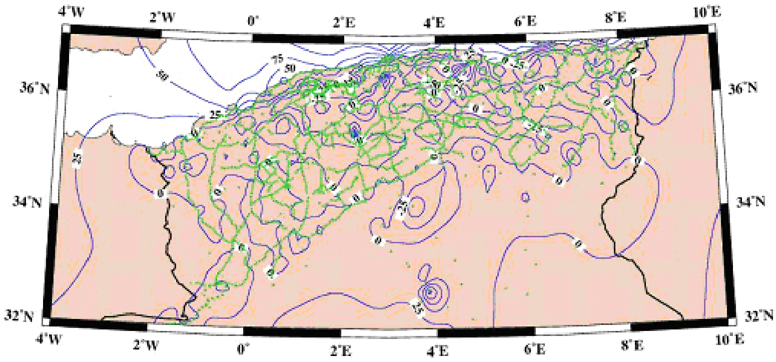

Fig.1 Free air anomalies after subtraction of the EGM96 contribution. Units mGal.

The RTM terrain effect reduction has been computed using a detailed 30"x30" grid and the outer zone height grid 5'x5' from the reference height grid 30'x30'.

After the subtraction of the EGM96 contribution and RTM terrain effect we obtain the residual anomalies by the following relation:

$$\Delta g_{Rés} = \Delta g_{fa} - \Delta g_{EGM96} - \Delta g_{RTM} \quad \textbf{(1)}$$

Table2. Statistics of the RTM subtraction from the reduced anomalies. Units mGal.

#	Min	Max	Mean	Std. Dev.
$\Delta g_{Residual}$	**-112.66**	**102.32**	**0.79**	**22.48**

3. Least Squares Collocation.

The LSC solution is gotten under the following shape:

$$T(P) = \sum_{i=1}^{N} b_i \cdot \mathrm{cov}(T(P), L_i),$$
$$(b_i) = (\mathrm{cov}(L_i, L_j) + \sigma_{ij})^{-1} \cdot (x_j) = \overline{C}^{-1} \cdot x_j \quad \textbf{(2)}$$

Where T is the local approximation of the anomalous potential, x_j are the observations and σ_{ij} are the errors of covariance. The covariance is represented by the expression that follows in which the constant R (Radius of the Bjerhammar sphere), ***a*** and ***A*** are determined from the local gravity data.

$$\begin{aligned}\mathrm{cov}(P,Q) &= \mathrm{cov}(r,r',\psi) \\ &= a\cdot\sum_{k=2}^{K}\sigma_{EGM}^{2}\left(\frac{R^2}{rr'}\right)^{k+1}P_k(\cos\psi)+\sum_{k=K+1}^{+\infty}\frac{A}{(k-1)(k-2)(k+4)}\left(\frac{R^2}{rr'}\right)^{k+1}P_k(\cos\psi)\end{aligned} \quad \textbf{(3)}$$

P and Q are two points between a spherical distance, and r, r' are the distances of the two points from the origin.

Initially an empiric covariance function has been determined of the reduced gravity anomalies.

The estimated values have been adapted in that case to a covariance model by an iterative adjustment with the 3 parameters R, $\boldsymbol{a}$ and $\boldsymbol{A}$.

The limit summation has been fixed to 250, the coefficients bigger than 250 didn't give reliable information in the region. The depth of the Bjerhammar sphere ($R - R_B$) has been estimated to -3.736 km and the total variance of gravity anomalies to 603.36 mgal².

The Figure2 shows the empirical and analytical covariance functions.

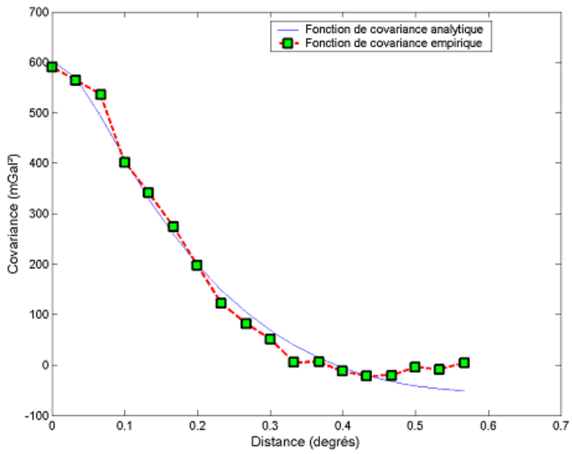

Figure 2. Covariance functions of reduced gravity anomalies.

The empirical covariance function of the residual gravity anomalies has as well been determined and the empirical values have been adapted to a covariance model.

The limit summation for this time has been fixed to 260, The depth of the Bjerhammar sphere ($R - R_B$) has been estimated to -9.961 km and the total variance of gravity anomalies to 432.83 mgal².

The figure 3 shows the empirical and analytical covariance functions.

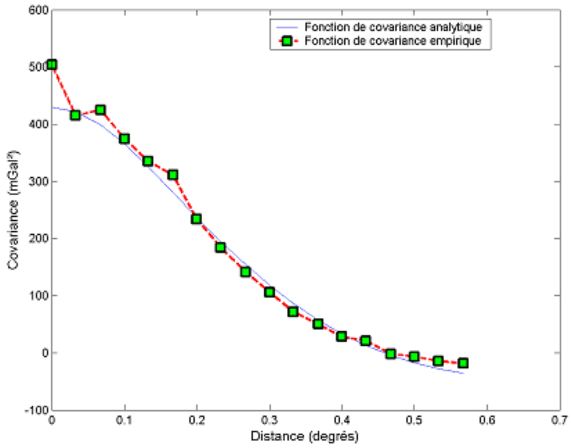

Figure 3. Covariance functions of residual gravity anomalies.

The 2534 reduced and residual gravity anomalies have been used therefore to determine an estimated of T, from which the estimates of the geoid heights on the 43 benchmarks of GPS-Levelling have been computed. The results of the differences between observed values and predicted are presented in the table3.

Table 3. Statistics of the differences between predicted and observed values. Units m.

43 points	Min	Max	Mean	Std.Dev.
GPS-Levelling	**32.48**	**49.82**	**44.53**	**3.93**
Prediction by reduced gravity	**32.24**	**50.60**	**44.09**	**4.12**
Differences	**-1.40**	**3.05**	**0.44**	**1.10**

Table 4. Statistics of the differences between predicted and observed values. Units m.

43 points	Min	Max	Mean	Std.Dev.
GPS-Levelling	**32.48**	**49.82**	**44.53**	**3.93**
Prediction by residual gravity	**33.09**	**50.68**	**44.66**	**4.07**
Differences	**-2.54**	**2.93**	**-0.13**	**1.35**

The observation must be rejected if:

$$\left| N_{GPS} - N_{\Delta g} \right| \geq 3 \cdot (C_{pp} - C_{pi}{}^{T} \left\{ \overline{C}_{ij} + Err_{ij}{}^{2} \right\}^{-1} C_{pj})^{1/2} \text{ and } \geq \text{ to the fixed doorstep.}$$

This has given several suspected errors, six observations have been rejected, the results of differences between the retained observed values and predicted are presented in the tables 5 and 6.

Table 5. Statistics of the differences between predicted and observed values. Units m.

37 points	Min	Max	Mean	Std.Dev.
GPS-Levelling	32.48	49.82	44.41	4.13
Prediction by reduced gravity	32.24	50.60	44.27	4.35
Differences	-1.40	1.47	0.14	0.85

Table 6. Statistics of the differences between predicted and observed values. Units m.

37 points	Min	Max	Mean	Std.Dev.
GPS-Levelling	32.48	49.82	44.41	4.13
Prediction by residual gravity	32.27	50.74	44.28	4.31
Differences	-1.52	1.68	0.12	0.92

The residual geoid undulations were determined by LSC, where the required auto and cross-covariance functions are computed by covariance propagation from the modelled local covariance function.

The residual quasi-geoid is represented in the figure 4.

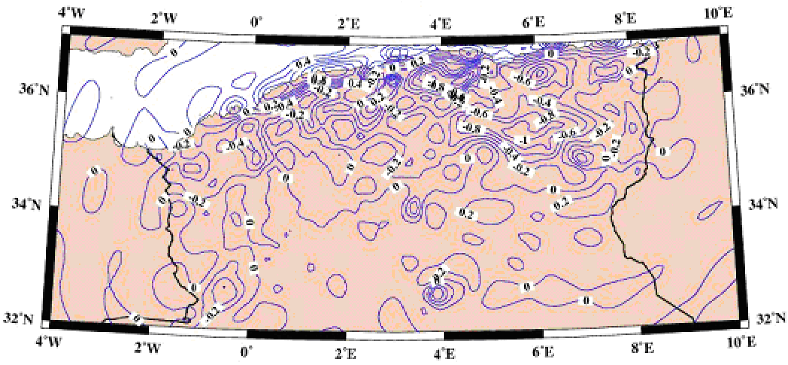

Figure 4. Residual quasi-geoid. Units m.

After restoring the long and short wavelength signals we obtain the final quasi-geoid presented below in the figure 5.

$$N = N_c + N_{EGM96} + N_{RTM} \quad \textbf{(4)}$$

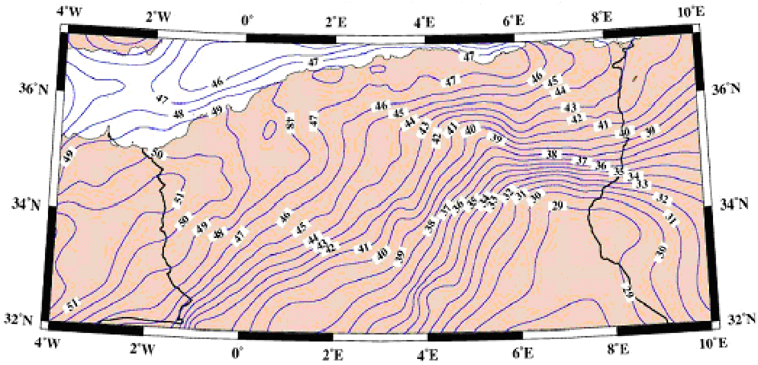

Figure 5. Final quasi-geoid. Units m.

4. Constant bias.

The parameters of which depend the used data, as the difference between the datum of the geoid and the local levelling, can be determined by LSC. The observations are tied to T and the vector of the X parameters by the following equation:

$$x_k = L_k(T) + A_K X + \varepsilon_k \tag{5}$$

Where L_k is associated to the observation, A_k is a vector with the elements 0 or 1, X is the vector parameter and ε_k is the error of observation.

So :

$$X = (A^T \overline{C}^{-1} A)^{-1} \cdot A^T \overline{C}^{-1} x_i \tag{6}$$

The constant bias between the gravimetric datum and the local levelling has been estimated, using residual data.

The results are presented in the tables below.

Table 7. Statistics of differences between the residual gravimetric quasi-geoid undulations and GPS-levelling at 37 control points (in meters) before fitting.

Differences ζ rtm observed – ζ rtm predicted (m)	Before fitting
Mean	-.382
Std.Dev	1.079

Table 8. The parameter transformation model.

Data	Parameter		
Units : m		**Values**	**Error estimates**
No	Constant bias	.128	.108

Table 9. statistics of differences between the residual gravimetric quasi-geoid undulations and GPS-levelling at 37 control points (in meters) after fitting.

Differences ζrtm observed – ζ rtm predicted (m)	After fiting
Mean	.000
Std.Dev	.244

4. Conclusion.

The gravimetric geoid has been computed by the Least Squares Collocation method.

The subtraction of EGM96 gave the expected results, the variance and the mean value decreased significantly. The gravity RTM subtraction didn't reduce the variance a lot on the other hand the mean value has been reduced. This is due probably to the quality of the DTM used.

The expected errors of the GPS-Levelling data are (±0.5 m), due mainly to the errors in the levelling.

However, after the EGM96 subtraction and prediction by gravity, large differences (around 3 m) have been obtained between observed and predicted values for six stations. It might be antenna height problems or erroneous identification of the levelling points. It might also be due to tectonic movements in the period between the levelling and the GPS.

Through this study we could see that the Least Squares Collocation method offers an important alternative to achieve an optimal evaluation in a stochastic process and to detect subsequently the gross errors of gravity data and GPS-Levelling.

In addition and at last, the constant bias No between the gravimetric datum and the local levelling has been estimated to (0.128 m) with error estimate of (0.108 m).

The local gravimetric geoid determined in the setting of this study deserves to be improved, by a densification of the gravimetric cover, the use of a more precise DTM and GPS-Levelling data with better quality.

5. References.

[1] C.C. Tscherning, Geophysical Institute, University of Copenhagen, Haraldsgage 6, DK-2200 Copenhagen N, July 1990. The Use of Optimal Estimation for Gross-error Detection in Databases of Spatially Correlated Data.

[2] C.C.Tscherning, Geophysical Institute, University of Copenhagen, Haraldsgage 6, DK-2200 Copenhagen N. Mathematical and statistical methods in physical geodesy, Spring semester 1991. Revised July 1992.

[3] C.C. Tscherning. The Ohio State University, Department of Geodetic Science, July 1974. A FORTRAN IV Program for the Determination of the Anomalous Potential Using Stepwise Least Squares Collocation.

[4] C.C.Tscherning, Department of Geophysics, Juliane Maries Vej 30, DK-2100 Copenhagen Ø, Denmark. Datum-shift, error-estimation for geoid determination, prepared for the International School on the Determination and Use of the Geoid. Draft, July 2002.

[5] C.C.Tscherning (Department of Geophysics, Juliane Maries Vej 30, DK-2100 Copenhagen Ø, Denmark) , Anwar Radwan, A.A.Tealeb, S.M.Mahmoud, Abd El-monum Mohamed, Ramdan Hassan, El-Syaed Issawy and K. Saker (all at National Research Institute of Astronomy and Geophysics, Helwan, Cairo, Egypt). Local geoid determination combining gravity disturbances and GPS/levelling A case study in the Lake Naser area, Aswan, Egypt.

[6] Gravsoft – A System for Geodetic Gravity Field Modelling. C.C. Tscherning, Department of Geophysics, Juliane Maries Vej 30, DK-2100 Copenhagen N. R. Forsberg and P. Knudsen, Kort og Matrikelstyrelsen, Rentemestervej 8, DK-2400 Copenhagen NV.

[7] S.A. Ben Ahmed Daho, S. Kalouche. Centre National des Techniques Spatiales, Arzew-31200, Algérie. Validation des Mesures Gravimétriques Par la Méthode de Collocation. Revue International des Technologies Avancées, janvier 2003.

[8] H. Moritz, 1980. Advanced Physical Geodesy, H. Press, Karlsruhe-Tundridge Wells.

[9] The Generic Mapping Tools (GMT), Paul Wessel, School of Ocean and Earth Science and Technology, University Of Hawaii at Manoa, and Walter H. F. Smith, Laboratory for Satellite Altimetry, NOAA/NESDIS/NODC, March 2002.

[10] Lecture Notes, International School for the Determination and Use of the Geoid, Milan Oct. 1994, and Rio de Janeiro 1997.

[11] M.A. Meslem, Résultats préliminaires relatifs à la détermination d'un géoïde du Nord de l'Algérie, Bulletin des Sciences Géographiques N.12, INCT, Oct.2003.

Improvement of the gravimetric model of quasigeoid in Slovakia

Marcel Mojzeš, Juraj Janák, Juraj Papčo
Department of Theoretical Geodesy, Slovak University of Technology in Bratislava, Slovak Republic

Abstract. The paper presents two recent approaches of the quasigeoid modelling GMSQ03B and GMSQ03C in the area of Slovakia and their modifications after fitting by GPS/levelling method. The description of data sources follows the two different computational schemes. The statistical testing and fitting using 59 GPS/levelling points are presented. A brief discussion, conclusion and future perspective are summarized in the paper.

Keywords. Gravimetric quasigeoid, data sources, GPS/levelling

1 Introduction

Slovakia is predominantly mountainous country located in central Europe. There is the first part of the Carpathian belt. Slovakia had been systematically measured by detailed gravity measurements from 1956 to 1992 (Kubeš et al., 2001). All area of Slovakia had been covered by gravity observations with approximately homogeneous density varying from 3 to 6 points per square km, that represents more than 200, 000 gravity points. On this basis, using the generalized Molodensky's theory, we have been trying for last nine years to compile the most detailed and accurate model of the quasigeoid. The first attempt was done in 1995 followed by the versions 1996, 1998A and 1998B. Especially the version 1998B after fitting into national vertical datum, known as GMSQ98BF – Gravimetric Model of Slovak Quasigeoid 1998 (Mojzeš and Janák, 1998) and (Mojzeš and Janák, 1999), has frequently been used for various scientific and practical applications.

Since 1998 the gravity database has been revised as far as blunders and systematic errors are concerned (Kubeš et al., 2001). Moreover the wider area of the mean gravity data has meanwhile become available. Some progress in theory and technology of computation has also been made, especially in combining of the terrestrial gravity data with the global geopotential model. All these circumstances have led us to our two recent approaches of the quasigeoid model in Slovakia: GMSQ03B and GMSQ03C and their modifications after fitting GMSQ03BF and GMSQ03CF respectively.

2 Data sources

Three types of input data were used for computation: Terrestrial gravity data (point and mean), elevation data (detailed and global) and global geopotential models. One paragraph is dedicated to describe the sources of a particular data type. As far as the location of all data is concerned, the reference system ETRS89 was used. Normal gravity field applied in computation was GRS80.

We used two sources of gravity data: point refined Bouguer gravity anomalies (232, 280 values) mainly within the Slovakia and mean values of the refined Bouguer gravity anomalies with resolution of $5' \times 7.5'$ in the area $44° < \varphi < 56°$ and $12° < \lambda < 30°$. The first source comes from detailed gravity measurements 1956-1992 mentioned in introduction. Both data sets were transformed to the gravity system GrS-95 (Klobušiak and Pecár, 2004) based on 16 absolute gravity points.

In order to transform the refined Bouguer gravity anomalies into Faye gravity anomalies, the elevation data were needed. We used two digital terrain models (DTM): national DTM within Slovakia and global DTM elsewhere. The first DTM is known as DMR2/ETRS89 and its resolution is $3''$ in latitude and $5''$ in longitude (Mojzeš, 2002). This resolution approximately corresponds to distance 100 by 100 metres. The vertical datum of mentioned DTM is Kronstadt, Baltic Sea with the abbreviation Bpv. The global DTM we used is well known GTOPO30 (http://edcdaac .usgs.gov/gtopo30.gtopo30.asp). This model was used outside of Slovakia. The unsolved problem we still have with the elevation data is the optimal connection of both national and global DTMs.

The last data type used in our solutions was the global geopotential model. We used two different models. First, the satellite only model GGM01 coming from GRACE dedicated satellite mission in tide-free system (Rummel et al., 2002). The second was well known combined model EGM96 (Lemoine et al., 1998).

3 Computation schemes

Both solutions GMSQ03B and GMSQ03C were in principle computed as so-called gradient solution of the linear Molodensky's problem. Second term of the Molodensky series was approximated by terrain correction as recommended it by Moritz (1980). Correction of the part of the error coming from this approximation was applied in both solutions. The major differences between two solutions are in the manner of how the geopotential model is combined with the terrestrial data and how the integration of the residual gravity anomalies is performed.

The first step, similar in both solutions, was the compilation of the residual Faye anomalies in a regular geographical grid $\Delta\varphi$=20″ and $\Delta\lambda$=30″. First the refined Bouguer gravity anomalies had to be interpolated into mentioned grid. This was done using the Kriging interpolation technique, assuming the anisotropy in geographical coordinates. Then the interpolated refined Bouguer anomalies were transformed into Faye anomalies (free-air plus terrain correction) according to formula

$$\Delta g_F = \Delta g_{RB} + 2\pi G\rho H \tag{1}$$

where Δg_{RB} are the refined Bouguer gravity anomalies, G is the Newton gravitational constant, ρ is the density of topographical masses (we assumed constant value ρ=2670 kg/m^3) and H stands for normal height in particular grid nodes obtained from DTM. Then the long wavelength part of the free-air gravity anomaly, assuming it approximately identical with the long wavelength part of the Faye anomaly, was subtracted from the Faye anomaly in order to obtain the residual Faye anomaly. The long wavelength parts for particular solutions were computed from global geopotential models GGM01 or EGM96 up to degree and order 20 or 360.

Solution GMSQ03B was computed using a low degree (n=20) spheroid obtained from the geopotential model GGM01. The aim was to avoid the errors coming from the higher-degree geopotential coefficients. Residual Faye anomalies were integrated using modified spheroidal Stokes's function. Modification according to idea of Molodensky (1962) up to degree 20 was used. Integration of the residual Faye anomalies was performed using classical numerical integration up to spherical distance ψ=3°. The truncation bias was estimated by EGM96 geopotential model using coefficients from 21 to 360.

Solution GMSQ03C was computed using a high degree (n=360) spheroid obtained from the geopotential model EGM96. Residual Faye anomalies were integrated using Spherical Stokes's function. Applied integration technique was the Fast Fourier Transformation over the spherical rectangle integration domain identical with the area of input gravity data described above. The GRAVSOFT software package (Tcherning et al., 1992) was used for computation of residual part of the quasigeoid. The truncation bias was neglected.

Let us to describe both solutions mathematically and graphically. The quasigeoid model GMSQ03B consists of four terms

$$\zeta_{GMSQ03B} = \zeta_{GGM01} + \zeta_{res} + \zeta_{tb} + \zeta_{Moritz} \tag{2}$$

where the first term represents the reference spheroid, the second term is residual part of the quasigeoid obtained from numerical integration of residual Faye anomalies, the third term is estimation of the truncation bias correction and the last term is correction of approximation of the second term of Molodensky's series

$$\zeta_{Moritz} = \pi G\rho\gamma_P^{-1} H_P^2 \tag{3}$$

computed according to Moritz (1980, Eq.(48-29)). In Eq. (3) the symbols G and ρ are obvious and γ_P is normal gravity and H_P stands for normal height at the point of computation.

The quasigeoid model GMSQ03C consists of three terms

$$\zeta_{GMSQ03C} = \zeta_{EGM96} + \zeta_{res} + \zeta_{Moritz} \tag{4}$$

where the meaning of particular terms is analogous to Eq.(2). Of course the first two terms of the right hand side were computed from the different data and the second term using even different integration technique. The third term in Eq.(4) computed from Eq.(3) is identical with the last term of Eq.(2).

The final quasigeod model GMSQ03B is shown in Fig.1.

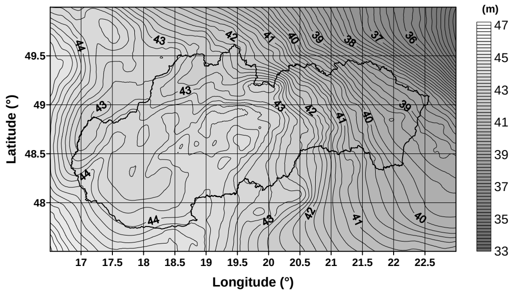

Fig.1 Quasigeoid model GMSQ03B

Another model is not plotted, because the figure would be very similar, rather the difference GMSQ03B-GMSQ03C between both solutions is depicted in Fig.2.

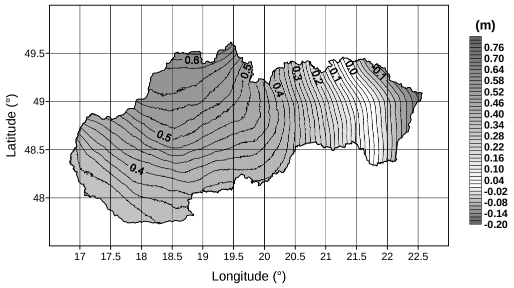

Fig.2 Difference between GMSQ03B and GMSQ03C

Both models are stored as a digital raster in geographical grid with the resolution of 20″×30″.

4 Testing and fitting

As the models of geoid or quasigeoid become more accurate because of the advanced theory and also the quality and quantity of the data, the choice of the verification method and quality of the testing points become very important task. Therefore we chose the independent verification method GPS and levelling. Within the area of Slovakia we chose the 59 testing points shown in Fig.3.

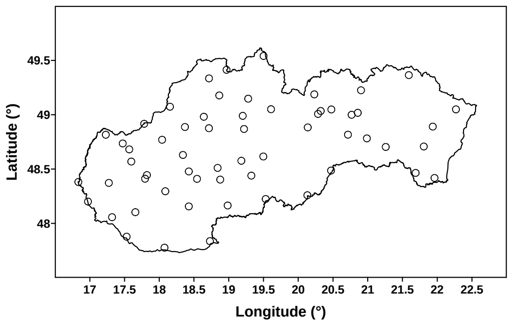

Fig.3 Distribution of the testing points

These points belong to either Central European Geodynamic Reference Network (CEGRN), see (Hefty and Gerhátová, 1997), or Slovak Geodynamic Reference Network (SGRN), see (Hefty, 1996). According to renowned estimates, e.g. (Stangl, 1998) and (Hefty and Mojzeš, 1999), the accuracy of the ellipsoidal height at these points in certain epoch is not worse then 2 centimetres. The accuracy of the normal heights determined by levelling over the Slovakia, in a relative sense, is also about 2 centimetres (ibid.).

The heights of quasigeoid models above the reference ellipsoid GRS80 were interpolated at the location of testing points and compared with the reference values obtained from the simple formula

$$\zeta_{ref} = h - H \tag{5}$$

where h is the ellipsoidal height and H is the normal height according to Molodensky. The basic statistics of the differences is presented in Tab.1.

Table 1 Basic statistics of the set of 59 differences

Quantity	$\zeta_{GMSQ03B} - \zeta_{ref}$	$\zeta_{GMSQ03C} - \zeta_{ref}$
Mean	0.334 m	0.711 m
St. dev.	0.190 m	0.076 m
Range	0.856 m	0.363 m

In order to use the quasigeoid model in geodetic practice, e.g. for estimation of normal heights from GPS measurements, the adaptation of quasigeoid into national vertical datum, so called fitting, is necessary. Incompatibility of the gravimetric models with the national vertical datum is mainly due to influence of global geopotential models in gravimetric solutions, but the differences reflect also other influences and also errors. The fitting is always a “dangerous” process where the original quasigeoid model can be deformed and getting worse, especially between the fitting points. Therefore such a process should be treated with a special care. The best case would be to use the constant shift only to unify the vertical datum. If this is not possible, because the differences show some clear long wavelength features, the fitting surface of lowest possible degree should be used.

For fitting process we used the surface polynomial regression and the fitting points were identical with the testing points (Fig.3). The differences $\zeta_{ref} - \zeta_{GMSQ03B/C}$ were modelled as follows

$$\Delta\zeta = \sum_{p=0}^{P} \sum_{q=0}^{Q} Q_{p,q} (\varphi - \varphi_0)^p \left((\lambda - \lambda_0) \cos\varphi \right)^q \tag{6}$$

In Eq. (6) the φ, λ are the ellipsoidal coordinates of fitting points, φ_0, λ_0 are chosen fixed coordinates and $Q_{p,q}$ are unknown coefficients estimated using the least squares method. The optimal degree of polynomial surface was chosen according to (Anděl, 1998)

$$A_k = \sigma_k^2 \left(1 + \frac{k}{\sqrt[4]{n}} \right) \tag{7}$$

where A_k is the criterion, n is the number of fitting points, k is the degree of polynomial surface and σ_k is the standard deviation of residuals. The optimal degree is the lowest one where the stop criterion A_k decreasing. For both models of quasigeoid in our case, the second degree polynomial surface with 6 coefficients was estimated as the optimal. The coefficient values are shown in Tab.2.

Table 2 Values and standard deviations of the fitting polynomial surfaces

Quasigeoid	GMSQ03B		GMSQ03C	
Coefficient	Value	St. dev.	Value	St. dev.
$Q_{0,0}$ (m)	-0,2903	0,0078	-0,7394	0,0075
$Q_{1,0}$ (m/°)	0,0512	0,0138	-0,0697	0,0122
$Q_{0,1}$ (m/°)	-0,1807	0,0051	-0,0445	0,0048
$Q_{1,1}$ (m/°^{2})	-0,0560	0,0186	0,0015	0,0168
$Q_{2,0}$ (m/°^{2})	-0,0500	0,0261	-0,0576	0,0253
$Q_{0,2}$ (m/°^{2})	-0,0660	0,0054	0,0325	0,0053

Shape of the polynomial surfaces is shown in Fig.4. and Fig.5.

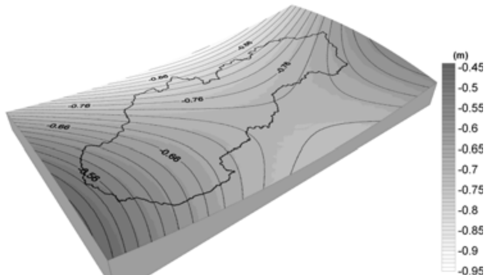

Fig.4 Fitting polynomial surface for GMSQ03B

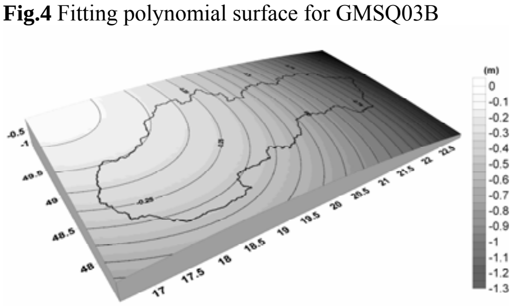

Fig.5 Fitting polynomial surface for GMSQ03C

Names of the quasigeoid models after fitting are GMSQ03BF or GMSQ03CF respectively. The standard deviation of residuals computed at the testing points after fitting is 0.041m for GMSQ03BF and 0.032m for GMSQ03CF. Reader is encouraged to compare these values with the corresponding standard deviations before fitting in Tab.1. It is also interesting to see the residuals obtained at the testing points after fitting process plotted as surface maps, see Fig.6. and Fig.7, or as histograms, see Fig.8. and Fig.9.

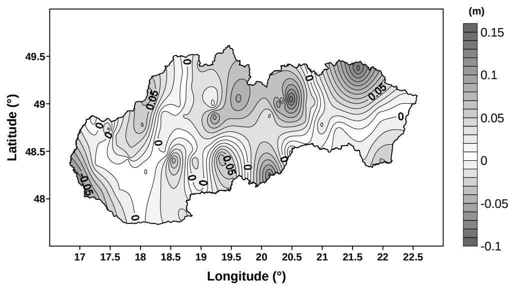

Fig.6 Residuals of GMSQ03BF

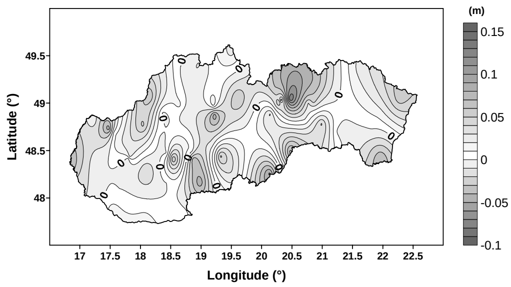

Fig.7 Residuals of GMSQ03CF

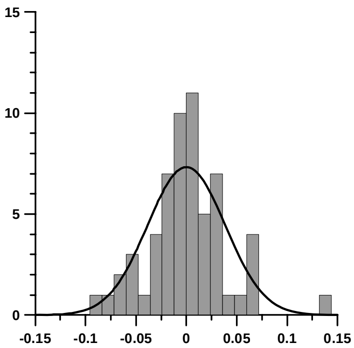

Fig.8 Histogram of GMSQ03BF residuals, x-axis in meters

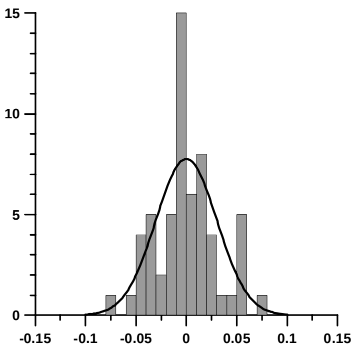

Fig.9 Histogram of GMSQ03CF residuals, x-axis in meters

5 Conclusion and perspective

To rich 1-centimeter accuracy of the quasigeoid model in an absolute sense in a mountainous country, as e.g. Slovakia, is very difficult task. One of the problems is that even the accuracy of reference values at the testing points is sometimes worse than one centimetre. Some improvements can still be done in theory and technology of computation. Presented quasigeoid models can guarantee, as you can see from the results, accuracy better than 5 centimetres in an absolute sense. Of course in many local areas it is much better, also below one centimetre.

Our future investigation, in order to improve the accuracy of the quasigeoid model, will be oriented to rigorous computation of the second term of Molodensky's series, refinement of digital terrain model, improvement of quality of the testing points, optimal numerical integration and careful unification of all reference systems.

Acknowledgement

The project of compilation of new quasigeoid model of Slovakia was partially supported by Research Institute of Geodesy and Cartography in Bratislava and partially supported by Grant Agency of the Slovak Republic (Project VEGA 1/1433/04).

For our computations we use several software products: commercial products SURFER and GRAPHER for interpolation of the input data and creating pictures, and scientific products SHGEO and GRAVSOFT software packages for working with global geopotential models and for numerical integration. We also use some, already mentioned, public data sets: GGM01, EGM96 and GTOPO30.

References

Anděl, J. (1998). Statistical Methods. Matfyz Press, Prague. (in Czech)

Hefty, J. and Ľ. Gerhátová (1997). Implementation of BERNESE software 4.0, processing of connection measurements of selected AGS points with the SLOVGERENET, comparison of processing using the version 3.5 and 4.0 and it's analysis. Technical report, Slovak University of Technology, Bratislava. (in Slovak)

Hefty, J. and M. Mojzeš (1999) Heights in Slovak Geodynamic Reference Network. Proceedings of the workshop "GPS and heights". TU Brno. (in Slovak)

Klobušiak, M. and J. Pecár (2004). Model and algorithm of effective processing of gravity measurements performed with a group of absolute and relative gravimeters. Geodetický a kartografický obzor 50 (92), No. 4-5, Prague, pp. 99-110. (in Slovak)

Kubeš, P., T. Grand, J. Šefara, R. Pašteka, M. Bielik and S. Daniel (2001). Atlas of geophysical maps and profiles. Technical report. National geological institute, Bratislava. (in Slovak)

Lemoine, F.G. et al. (1998). The development of the joint NASA GSFC and the NIMA geopotential model EGM96. NASA Technical Report NASA/TP-1998-206861, Goddard Space Flight Center, Greenbelt, Maryland.

Mojzeš, M. and J. Janák (1998). Gravimetric model of Slovak quasigeoid. Proceedings of the Second Continental Workshop on the Geoid in Europe. Reports of the Finnish Geodetic Institute 98:4, pp. 277-280.

Mojzeš, M. and J. Janák (1999). New gravimetric quasigeoid of Slovakia. Bolletino di Geofisica Teorica ed Applicata, Vol. 40, No. 3-4, pp. 211-217.

Mojzeš, M. (2002). Accuracy analysis of the digital terrain model DMR-2 in ETRS-89 reference system. Proceedings of the VIII. International Polish, Czech and Slovak Geodetic Days. Polanica. Zdrój, pp. 45-51. (in Slovak)

Molodensky, M.S., V.F. Eremeev and M.I. Yurkina (1962). Methods for Study of the External Gravitational Field and Figure of the Earth. Israel Program for Scientific Translations, Jerusalem.

Moritz, H. (1980). Advanced Physical Geodesy. Abacus Press, Karlsruhe.

Rummel, R., G. Balmino, J. Johannessen, P. Visser and P. Woodworth (2002). Dedicated Gravity Field Missions – Principles and Aims. Journal of Geodynamics, Vol. 33, 1-2, pp. 3-20.

Stangl, G. (1998). The GPS Campaigns of CERGOP. Reports on Geodesy, No. 9 (39), pp. 39-55.

Tscherning, C.C., R. Forsberg and P. Knudsen (1992). The GRAVSOFT Package for Geoid Determination. Proceedings of the First Continental Workshop on the Geoid in Europe. P. Holota and M. Vermeer (Eds.). Research Institute of Geodesy, Topography and Cartography, Prague, pp. 335-347.

COMPARISON AMONG SPHERICAL HARMONIC SYNTHESIS METHODS FOR FUNCTIONALS OF THE GRAVITY FIELD

Elena FANTINO[(1)], Stefano CASOTTO[(1,2)]

[(1)] Dipartimento di Astronomia, Università di Padova, vicolo dell'Osservatorio 2, 35122 Padova, Italy; e-mails: fantino@pd.astro.it, casotto@pd.astro.it

[(2)] CISAS "G.Colombo", Università di Padova, via Venezia 15, 35131 Padova, Italy

Abstract

Four well-known and qualified algorithms for the computation of the Earth's gravitational potential and its first and second gradients are examined and compared. Their characteristics are analysed with reference to the computational requirements of the global geopotential estimation process from satellite gradiometry. Numerical tests have been performed in order to assess and compare the efficiency, accuracy and precision of the algorithms. The algorithm of Clenshaw has shown to be by far the most efficient and therefore the most suitable for implementation and use when dealing with large amounts of observations.

Keywords: Spherical harmonic synthesis; Associated Legendre Functions; Helmholtz Polynomials; Clenshaw summation method

1 Introduction

The computation of the Earth's gravitational potential and its derivatives is a problem of interest to many applications in geophysics and geodesy. With reference to satellite gravity gradiometry, the phase of harmonic synthesis and least squares adjustment for geopotential and gravity gradient estimation is of major concern when dealing with large amounts of observations (of the order of 10^8) and high resolution (of the order of $9 \cdot 10^4$ Stokes coefficients) gravity models to be solved for: aspects such as numerical accuracy and computational performance are an issue of primary importance and must be carefully and critically addressed.

Following Bettadpur et al. (1992), we can identify three areas of concern in general spherical harmonic synthesis: the selection of a potential formulation (including the choice of the coordinate system describing the position of the observation points), the selection of the algorithms for the recursive computation of the Associated Legendre Functions (ALFs) and, finally, the issue of arrangement of the computations for the best performance on a given computer architecture.

In the past great attention has been given by several authors to the algorithms for the computation of the geopotential and its derivatives. In this work we have selected, examined and compared four among the most qualified and well-known analytical methods for the computation of the gravitational potential and its derivatives. They are: the traditional forward column recursion in spherical coordinates; the method proposed by Pines (1973) based on Helmholtz Polynomials (HPs) in rectangular Earth-fixed cartesian coordinates (and here presented as a forward column recursion method); the method developed by Cunningham (1970) and more recently reintroduced by Metris et al. (1999) consisting in a downward recursion on a complex operator of derivation in rectangular Earth-fixed cartesian coordinates; a backward recurrence method based on the Clenshaw summation formula (Press et al., 1992; Tscherning and Poder, 1982) in spherical coordinates. Note that the two methods in cartesian Earth-fixed coordinates (i.e., Pines and Cunningham-Metris) are singularity-free at the poles.

After a general introduction to the geopotential and its derivatives and the definition of the coordinate systems and transformations (Section 2), a description of the four algorithms is provided (Sections 3 to 6). Section 7 presents and describes a set of numerical tests applied to each algorithm, aiming at assessing numerical efficiency, relative numerical precision and numerical accuracy. The results of the comparison are discussed in Section 8.

2 The Earth's gravitational potential and its gradients

The gravitational potential V at a point P above the surface of the Earth can be written as a spherical harmonic expansion (Heiskanen and Moritz, 1967)

$$V(P) = \frac{\mu}{r} \sum_{n=0}^{\infty} \left(\frac{a}{r}\right)^n \sum_{m=0}^{n} \overline{P}_{nm}(\sin\varphi) \left(\overline{C}_{nm} \cos m\lambda + \overline{S}_{nm} \sin m\lambda\right) \tag{1}$$

where r, φ and λ are the spherical coordinates of P representing geocentric radius, latitude and longitude respectively, a is the mean Earth's radius, μ is the Earth's gravitational parameter ($\mu = GM_{\oplus}$), $\overline{C}_{nm}$ and $\overline{S}_{nm}$ are the fully normalized Stokes coefficients of the gravity field and $\overline{P}_{nm}(\sin\varphi)$ is the fully normalized Associated Legendre Function (fnALF) of the first kind of degree n and order m:

$$\overline{P}_{nm}(\sin\varphi) = \overline{P}_{nm}(\varphi) = N_{nm} \left[\frac{1}{n!2^n} \frac{d^{n+m}}{d(\sin\varphi)^{n+m}} (\sin^2\varphi - 1)^n\right] \tag{2}$$

with the full normalization factor

$$N_{nm} = \sqrt{\frac{(2-\delta_{o,m})(2n+1)(n-m)!}{(n+m)!}}. \tag{3}$$

In practice the expansion (1) is truncated at a maximum degree N, which determines the resolution of the gravity model. In this work we set $N = 360$. For issues such as the numerical stability of the recurrence relations employed for evaluating spherical harmonics of ultra-high degree and order (e.g., $N = 2700$) the reader is referred to Holmes and Featherstone (2002).

The gravitational potential V is a scalar field and as such can be regarded as a tensor of rank 0. The first gravity gradient ∇V is a tensor of rank 1 (a vector), the second gravity gradient $\nabla\nabla V$ is a tensor of rank 2. Now let us consider two generalized coordinate systems u^p and x^q. The transformations that affect a covariant and a contravariant tensor of rank 1, T_k and T^k respectively, under change of coordinates

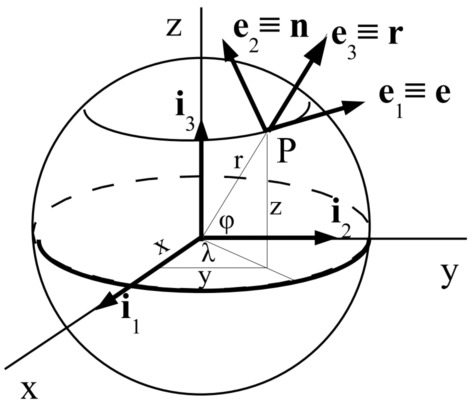

Figure 1: Relation between the spherical local coordinate system and the rectangular Earth-fixed coordinate system.

from u^p to x^q are

$$
\begin{aligned}
T_k &= \left(\frac{\partial u^m}{\partial x^k}\right) T'_m \\
T^k &= \left(\frac{\partial x^k}{\partial u^m}\right) T'^m.
\end{aligned}
\tag{4}
$$

Similarly, for a covariant and a contravariant rank 2 tensor, T_{kl} and T^{kl} respectively, we have:

$$
\begin{aligned}
T_{kl} &= \left(\frac{\partial u^m}{\partial x^k}\right)\left(\frac{\partial u^n}{\partial x^l}\right) T'_{mn} \\
T^{kl} &= \left(\frac{\partial x^k}{\partial u^m}\right)\left(\frac{\partial x^l}{\partial u^n}\right) T'^{mn}.
\end{aligned}
\tag{5}
$$

In this work we use two reference frames, the first a cartesian, Earth-centred, Earth-fixed frame with orthonormal vector basis ($\mathbf{i}_1$,$\mathbf{i}_2$,$\mathbf{i}_3$); the second a spherical local frame, centred at $P(\lambda,\varphi,r)$ with orthonormal vector basis ($\mathbf{e}_1$,$\mathbf{e}_2$,$\mathbf{e}_3$) which coincide with the East ($\mathbf{e}$), North ($\mathbf{n}$) and radial directions ($\mathbf{r}$) respectively (see Fig. 1).

In order to perform numerical comparisons among the algorithms we will apply the transformation of the first and second gravity gradient tensors from cartesian Earth-fixed coordinates to spherical coordinates. Introduce the transformation $x^p = x^p\left(u^q\right)$ between spherical local and rectangular Earth-fixed coordinates:

$$
\begin{aligned}
x &= r\cos\varphi\cos\lambda \\
y &= r\cos\varphi\sin\lambda \\
z &= r\sin\varphi.
\end{aligned}
\tag{6}
$$

The associated Jacobian matrix $\partial x^p/\partial u^q$ is

$$
\begin{pmatrix}
-\sin\lambda & \cos\lambda & 0 \\
-\sin\varphi\cos\lambda & -\sin\varphi\sin\lambda & \cos\varphi \\
\cos\varphi\cos\lambda & \cos\varphi\sin\lambda & \sin\varphi
\end{pmatrix}.
\tag{7}
$$

The transformations (4) and (5) from spherical to cartesian Earth-fixed coordinates as applied to the first and second gravity gradient tensors are provided in Tables 1

Table 1: The first gravity gradient: rotation of the physical components from cartesian Earth-fixed to spherical local coordinates.

$$
\begin{aligned}
V_\lambda &= -V_x \sin\lambda + V_y \cos\lambda \\
V_\varphi &= -V_x \cos\lambda \sin\varphi - V_y \sin\lambda \sin\varphi + V_z \cos\varphi \\
V_r &= V_x \cos\lambda \cos\varphi + V_y \cos\varphi \sin\lambda + V_z \sin\varphi
\end{aligned}
$$

Table 2: The second gravity gradient: rotation of the physical components from cartesian Earth-fixed to spherical local coordinates.

$$
\begin{aligned}
V_{\lambda\lambda} &= V_{xx} \sin^2\lambda - V_{xy} \sin 2\lambda + V_{yy} \cos^2\lambda \\
V_{\lambda\varphi} &= (V_{xx} - V_{yy}) \sin\lambda \cos\lambda \sin\varphi - V_{xy} \cos 2\lambda \sin\varphi + (V_{yz} \cos\lambda - V_{xz} \sin\lambda) \cos\varphi \\
V_{\varphi\varphi} &= \left(V_{xx} \cos^2\lambda + V_{xy} \sin 2\lambda + V_{yy} \sin^2\lambda\right) \sin^2\varphi - (V_{xz} \cos\lambda + V_{yz} \sin\lambda) \sin 2\varphi + V_{zz} \cos^2\varphi \\
V_{\lambda r} &= [-V_{xx} \sin\lambda \cos\varphi + V_{yz} \sin\varphi + V_{yy} \sin\lambda \cos\varphi] \cos\lambda + V_{xy} \cos\varphi \cos 2\lambda - V_{xz} \sin\lambda \sin\varphi \\
V_{\varphi r} &= \left(V_{zz} - V_{xx} \cos^2\lambda - V_{xy} \sin 2\lambda - V_{yy} \sin^2\lambda\right) \sin 2\varphi/2 + (V_{xz} \cos\lambda + V_{yz} \sin\lambda) \cos 2\varphi \\
V_{rr} &= \left(V_{xx} \cos^2\lambda + V_{yy} \sin^2\lambda + V_{xy} \sin 2\lambda\right) \cos^2\varphi + (V_{xz} \cos\lambda + V_{yz} \sin\lambda) \sin 2\varphi + V_{zz} \sin^2\varphi
\end{aligned}
$$

and 2: there the tensor components are physical components, i.e., components with respect to the orthonormal vector basis of the corresponding coordinate system.

3 Forward column recursion in spherical coordinates

The most direct and traditional approach for evaluating the gravitational potential uses recursions on Associated Legendre Functions. The physical components of the first and second gravity gradients have the form reported in Table 3. The partial derivatives that appear there are obtained by differentiating Eq. (1) with respect to λ, φ and r accordingly. Their full expressions can be found in Xu (2003) and Ditmar and Klees (2002).

The standard way of evaluating the fnALFs and their derivatives is by recursion. There are numerous recurrence relations, reproduced for example in Abramowitz and Stegun (1964): there are recurrences on n alone, on m alone, and on both n and

Table 3: Physical components of the first and second gravity gradients in local spherical coordinates.

$$
\begin{aligned}
V_\lambda &= \frac{1}{r\cos\varphi}\partial_\lambda V & V_\varphi &= \frac{1}{r}\partial_\varphi V \\
V_r &= \partial_r V & V_{\lambda\lambda} &= \frac{1}{r^2\cos^2\varphi}\left(\partial_{\lambda\lambda} V + r\cos^2\varphi\,\partial_r V - \frac{1}{2}\sin 2\varphi\,\partial_\varphi V\right) \\
V_{\lambda\varphi} &= \frac{1}{r^2\cos\varphi}\left(\partial_{\lambda\varphi} V + \tan\varphi\,\partial_\lambda V\right) & V_{\varphi\varphi} &= \frac{1}{r^2}\left(\partial_{\varphi\varphi} V + r\partial_r V\right) \\
V_{\lambda r} &= \frac{1}{r\cos\varphi}\left(\partial_{\lambda r} V - \frac{1}{r}\partial_\lambda V\right) & V_{\varphi r} &= \frac{1}{r}\left(\partial_{\varphi r} V - \frac{1}{r}\partial_\varphi V\right) \\
V_{rr} &= \partial_{rr} V
\end{aligned}
$$

m simultaneously. Most of the recurrences involving m are unstable and therefore dangerous for numerical work. The most commonly adopted procedure to produce a set of fnALFs complete to degree and order N follows the very well known forward column recursion (FCR) scheme on n (Hobson, 1965), which starts from the initialization $\overline{P}_{00}(\varphi) = 1$ and then computes the sectorial terms ($m = n$ with $n \geq 1$) by means of

$$\overline{P}_{nn}(\varphi) = f_n \cos\varphi \overline{P}_{n-1,n-1}(\varphi) \tag{8}$$

with

$$f_n = \sqrt{\frac{(2n+1)(1+\delta_{1,n})}{2n}}. \tag{9}$$

The remaining terms (zonals and tesserals with $0 \leq m \leq n-1$) are obtained from

$$\overline{P}_{nm}(\varphi) = g_{nm} \sin\varphi \overline{P}_{n-1,m}(\varphi) - h_{nm}\overline{P}_{n-2,m}(\varphi), \quad n > m \tag{10}$$

where

$$\begin{aligned} g_{nm} &= \sqrt{\frac{(2n+1)(2n-1)}{(n+m)(n-m)}} \\ h_{nm} &= \sqrt{\frac{(2n+1)(n-m-1)(n+m-1)}{(2n-3)(n+m)(n-m)}} = \frac{g_{nm}}{g_{n-1,m}}, \end{aligned} \tag{11}$$

while the fnALFs with $m > n$ are defined to be zero. The first derivatives of the fnALFs with respect to φ are given by (Ilk, 1983):

$$\frac{d\overline{P}_{nm}(\varphi)}{d\varphi} = m \tan\varphi \overline{P}_{nm}(\varphi) - k_{nm}\overline{P}_{n,m+1}(\varphi) \tag{12}$$

where

$$k_{nm} = \sqrt{\frac{(2-\delta_{o,m})(n-m)(n+m+1)}{2}}. \tag{13}$$

Differentiating Eq. (12) with respect to φ yields the second derivatives:

$$\begin{aligned} \frac{d^2\overline{P}_{nm}(\varphi)}{d\varphi^2} = &\, m\,(m\tan^2\varphi + \sec^2\varphi)\,\overline{P}_{nm}(\varphi) - (2m+1)k_{nm}\tan\varphi\,\overline{P}_{n,m+1}(\varphi) \\ &+ j_{nm}\overline{P}_{n,m+2}(\varphi) \end{aligned} \tag{14}$$

in which

$$j_{nm} = \sqrt{\frac{(2-\delta_{o,m})(n-m)(n-m-1)(n+m+2)(n+m+1)}{2}}. \tag{15}$$

The input required by the algorithm is the gravity field model ($\overline{C}_{nm}$, $\overline{S}_{nm}$ with $n, m = 0, ..., N$) and the position of K observation points (P_k: λ_k, φ_k, r_k with $k = 1, ..., K$ and $K \geq 1$). Optimum performance is reached by first evaluating and storing the normalization coefficients f_{nm}, g_{nm} ,h_{nm}, j_{nm} and k_{nm} [Eqs. (9), (11), (13) and (15)], then the latitude-dependent functions, i.e., the $\overline{P}_{nm}$ and their derivatives $d\overline{P}_{nm}/d\varphi$ and $d^2\overline{P}_{nm}/d\varphi^2$ [Eqs. (8), (10), (12) and (14)]; finally, for the given λ_k, the sums which yield the various partial derivatives of V are accumulated. This arrangement ensures

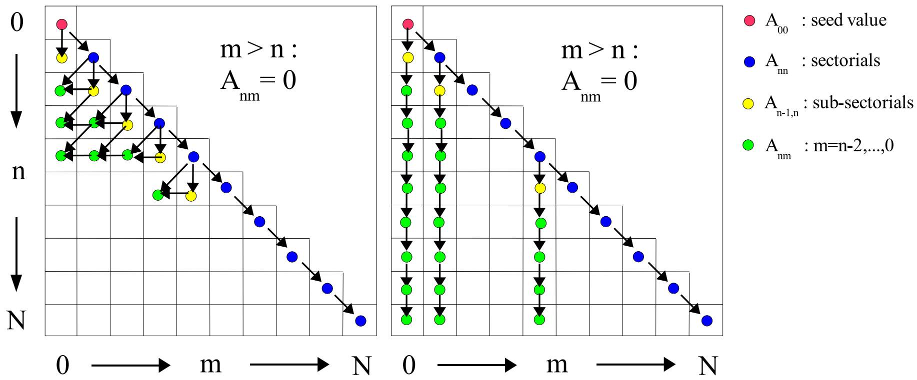

Figure 2: Left: mixed strides recursion algorithm. Right: forward column recursion scheme.

higher efficiency when dealing with data uniformly distributed on a spherical grid and accessed per parallel.

We implemented this algorithm in a Fortran90 computer code, named *LEGENDRE_a*, that, given the fully normalized Stokes coefficients of the gravity model and the position of the observation points, computes the gravitational potential and its first and second gradients in the $(\mathbf{e}_1,\mathbf{e}_2,\mathbf{e}_3)$ orthonormal basis. Another implementation of the same algorithm was kindly provided by F. Sansó (Politecnico di Milano, PoliMi) in the form of a dynamic link library (DLL) running under Matlab. We named it *LEGENDRE_b*.

4 The method of Helmholtz polynomials in Earth-fixed cartesian coordinates

In the work published by S. Pines in 1973 and later revised by Spencer (1976) the potential and its first and second gradients are computed in rectangular Earth-fixed coordinates. The algorithm developed by Pines uses Helmholtz Polynomials $A_{nm}(u)$ (Balmino et al., 1990) instead of ALFs

$$A_{nm}(u) = \frac{1}{n!2^n}\frac{d^{n+m}}{du^{n+m}}(u^2-1)^n \tag{16}$$

and the coordinates of the observation points are given by the components s, t and u of the geocentric unit position vector, supplemented by the geocentric distance r. The k^{th}derivative of the Helmholtz Polynomial of degree n and order m is the Helmholtz Polynomial of degree n and order $(m+k)$:

$$\frac{d^k A_{nm}(u)}{du^k} = A_{n,m+k}(u). \tag{17}$$

The author presented a recursion for the computation of the A_{nm} which, starting from the initialization $A_{00}(u) = 1$ (which follows from $P_0 = 1$), first fills in the diagonal (sectorial terms, $m = n$ with $n \geq 1$) and then yields the remaining zonal and tesseral terms $(0 \leq m \leq n-2)$ through a “mixed strides” recursion: away from the diagonal each polynomial is a linear combination of polynomials of different degree/order, therefore not on the same stride (row/column) (Fig. 2). This recipe is presented as a stable recursion. However, since we are basing our computations on fully normalized Stokes coefficients, appropriate normalization factors must be applied. The fully normalized Helmholtz Polynomial (fnHPs) $\bar{A}_{nm}(u)$ of degree n and order m is

$$\bar{A}_{nm}(u) = \sqrt{\frac{(2-\delta_{o,m})(2n+1)(n-m)!}{(n+m)!}} A_{nm}(u). \tag{18}$$

From our numerical experiments, we found that Pines' recursion scheme, as applied to the fnHPs, is strongly unstable. Fig. 3 illustrates a comparison with the results obtained by application of the traditional FCR scheme ($N = 360$), which on the contrary is very stable. As a consequence, we replaced the MSR scheme proposed by Pines with the FCR algorithm.

Written as a series expansion (truncated at a maximum degree N) in fnHPs, the Earth's gravitational potential V at a point P (x, y, z) in outer space is:

$$V(P) = V(x,y,z) \equiv V(s,t,u,r) = \sum_{n=0}^{N} \rho_n \sum_{m=0}^{n} \overline{A}_{nm}(u)\overline{D}_{nm}(s,t) \tag{19}$$

ρ_n being a recursively-defined function of r and $\overline{D}_{nm}(s,t)$ a so-called fully normalized mass coefficient function which depends on some trigonometric functions r_m and i_m of λ and the Stokes coefficients. By application of the chain rule of differentiation, the operators of derivation of the gravitational potential with respect to the cartesian Earth-fixed coordinates x, y, z of P can be written as a function of the operators of derivation with respect to s, t, u and r. Finally, the first and second gravity gradients, ∇V and $\nabla\nabla V$, in Earth-fixed cartesian coordinates are given by

$$\begin{aligned} V_x &= a_1 + sa_4 \\ V_y &= a_2 + ta_4 \\ V_z &= a_3 + ua_4 \end{aligned} \tag{20}$$

$$\begin{aligned} V_{xx} &= a_{11} + 2sa_{14} + a_4/r + s^2 a_{44} - s^2 a_4/r \\ V_{xy} &= a_{12} + sta_{44} + sa_{24} + ta_{14} - sta_4/r \\ V_{yy} &= a_{22} + 2ta_{24} + a_4/r + t^2 a_{44} - t^2 a_4/r \\ V_{xz} &= a_{13} + sua_{44} + sa_{34} + ua_{14} - sua_4/r \\ V_{yz} &= a_{23} + tua_{44} + ta_{34} + ua_{24} - tua_4/r \\ V_{zz} &= a_{33} + 2ua_{34} + a_4/r + u^2 a_{44} - u^2 a_4/r \end{aligned} \tag{21}$$

where a_j $(j = 1, 4)$ and a_{ij} $(i, j = 1, 4)$ are partial sums, functions of four additional mass coefficient functions and their derivatives. For the details of the method we refer the reader to the original work by Pines (1973).

We implemented this algorithm in a Fortran90 computer code, named *PINES*, that, given the fully normalized Stokes coefficients of the gravity model and the Earth-fixed rectangular coordinates x, y, z of K observation points P_k $(k = 1, ..., K$ and $K \geq 1)$, determines the gravitational potential and its first and second gradients. Best performance is reached by first evaluating and storing the various normalization coefficients, the functions ρ_n, r_m and i_m; then, the latitude dependent quantities, i.e.,

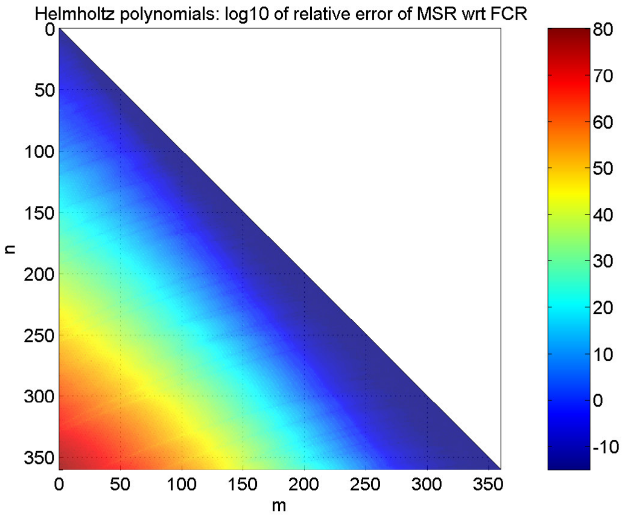

Figure 3: Log_{10} of the relative difference between the Helmholtz polynomials as computed with the FCR algorithm and with the MSR scheme: the difference grows larger with increasing degree (downwards) and decreasing order (backwards) proving that the MSR algorithm is highly unstable.

the Helmholtz polynomials $\overline{A}_{nm}$ and their derivatives $d\overline{A}_{nm}/du$ and $d^2\overline{A}_{nm}/du^2$ are computed; finally, for each s and t, the mass coefficient functions and their derivatives are formed, and the partial sums a_j and a_{ij} are accumulated. This arrangement offers higher efficiency when dealing with data distributed on a spherical grid and accessed per parallel.

5 The method of Cunningham-Metris

The algorithm developed by Cunningham (1970) is based on the representation of the gravitational potential in solid spherical harmonics V_{nm}

$$V_{nm} \equiv \frac{\overline{P}_{nm}(\sin\varphi)(\cos m\lambda + \mathrm{i}\sin m\lambda)}{r^{n+1}} \tag{22}$$

which enter the expression of V in the following way:

$$V = \mathrm{Re}\left[\mu \sum_{n=0}^{N}\sum_{m=0}^{n} a^n \left(\overline{C}_{nm} - \mathrm{i}\overline{S}_{nm}\right) V_{nm}\right] \tag{23}$$

i being the imaginary unit. The V_{nm} can be expressed through the operators of derivation $\partial/\partial z$ and $(\partial/\partial x + \mathrm{i}\partial/\partial y)$ and obey a downward recursion (Cunningham, 1970). Thanks to these two characteristics, any derivative of V_{nm} can be written as a simple linear combination of other V_{nm}.

The work recently published by Metris et al. (1999) makes one step forward by providing expressions for the derivatives of any order of V itself.

G.Metris and his collaborators implemented this algorithm into a Fortran77 computer programme which, given a set of fully normalized Stokes coefficients for the gravity model and the positions of the observation points, determines the gravitational potential and its gradients of arbitrary order with respect to the Earth-fixed coordinates x, y and z. The source code of this computer programme is available on the web http://wwwrc.obs-azur.fr/cerga/mecanique/potential. We upgraded it from single to double floating point precision and from Fortran77 to Fortran90. In the following it will be referred to as *METRIS*.

6 The method of Clenshaw summation

The algorithm developed by Clenshaw and known under the name of *Clenshaw summation* is a general method for computing sums of products between indexed coefficients and functions which obey a three-term recurrence relation. It belongs to the class of downward recurrence formulas. A general description of the algorithm can be found in Press et al. (1992); its application to geodetic problems was discussed by Tscherning and Poder (1982). Here we provide a derivation of the Clenshaw summation algorithm applied to the evaluation of the geopotential and its first and second gradients.

Our implementation of the Clenshaw summation is based on the recursion relations (10) and (8) that form the backbone of the FCR algorithm for fnALFs. By considering terms of equal order (therefore dropping the subscript m), the functions p_n are defined as

$$p_n = \overline{P}_{nm}(u)\left(\frac{a}{r}\right)^n \tag{24}$$

in which $u = \sin\varphi$. After some algebraic manipulation, the three-term recurrence relation (10) becomes

$$p_n = \alpha_n p_{n-1} - \beta_n p_{n-2} \tag{25}$$

with initialization $p_0 = 1$ and $p_1 = \alpha_1$, where $\alpha_n = u g_{nm} a/r$ and $\beta_n = (a/r)^2 h_{nm}$, with g_{nm} and h_{nm} given by Eq. (11). For every value of m there exists a set of coefficients $y_n^{(i)}$ such that

$$\begin{aligned}
y_{N+1}^{(i)} &= 0\\
y_N^{(i)} &= c_N^{(i)}\\
&\dots\\
y_n^{(i)} &= c_n^{(i)} + \alpha_{n+1} y_{n+1}^{(i)} - \beta_{n+2} y_{n+2}^{(i)}\\
\dots&\\
y_m^{(i)} &= c_m^{(i)} + \alpha_{m+1} y_{m+1}^{(i)} - \beta_{m+2} y_{m+2}^{(i)}
\end{aligned} \tag{26}$$

where

$$c_n^{(i)} = \begin{cases} \overline{C}_{nm} \text{ if } i = 1\\ \overline{S}_{nm} \text{ if } i = 2 \end{cases} \tag{27}$$

On defining the functions $v_m^{(i)}$ as

$$v_m^{(i)} = \sum_{n=m}^{N} c_n^{(i)} p_n, \tag{28}$$

it can be shown that

$$v_m^{(i)} = y_m^{(i)} p_m \tag{29}$$

and

$$V(r,\varphi,\lambda) = \frac{GM}{r} \sum_{m=0}^{N} \left(v_m^{(1)} \cos m\lambda + v_m^{(2)} \sin m\lambda \right) . \tag{30}$$

Note that only the sectorial fnALFs need to be computed and stored, and each term in the sum over the orders [Eq. (30)] is the product of only two factors, i.e., the fnALF of degree m and order m and the output $y_m^{(i)}$ of the recursion (26). This makes the evaluation of the gravitational potential very efficient.

The first and second order partial derivatives of the gravitational potential V with respect to the local spherical coordinates λ, φ and r of the observation point P can be written in a form similar to Eq. (30) by introducing recursions on appropriate "y" coefficients (Table 4) and defining the corresponding "v" terms (Table 5). Note that some partial derivatives with respect to λ make use of y coefficients and v terms specifically developed for other derivatives. The final expressions for the first and second order partial derivatives of V with respect to spherical coordinates are given in Table 6.

Table 4: Seed values (first and second column) and general three-term recursion (third column) for each set of y coefficients. The subscript $_{..,uu}$ means for example that the corresponding coefficient is employed in the computation of the second derivative of V with respect to u. The quantity q replaces the ratio a/r.

$y_{N+1}^{(i)} = 0$	$y_N^{(i)} = c_N^{(i)}$	$y_n^{(i)} = c_n^{(i)} + uqg_{n+1,n} y_{n+1}^{(i)} - q^2 h_{n+2,m} y_{n+2}^{(i)}$
$y_{N+1,r}^{(i)} = 0$	$y_{N,r}^{(i)} = c_N^{(i)}(N+1)$	$y_{n,r}^{(i)} = c_n^{(i)}(n+1) + uqg_{n+1,m} y_{n+1,r}^{(i)} - q^2 h_{n+2,m} y_{n+2,r}^{(i)}$
$y_{N+1,u}^{(i)} = 0$	$y_{N,u}^{(i)} = 0$	$y_{n,u}^{(i)} = qg_{n+1,m} y_{n+1,u}^{(i)} + uqg_{n+1,m} y_{n+1}^{(i)} - q^2 h_{n+2,m} y_{n+2,u}^{(i)}$
$y_{N+1,uu}^{(i)} = 0$	$y_{N,uu}^{(i)} = 0$	$y_{n,uu}^{i} = 2qg_{n+1,m} y_{n+1,u}^{(i)} + uqg_{n+1,m} y_{n+1,uu}^{(i)} - q^2 h_{n+2,m} y_{n+2,uu}^{(i)}$
$y_{N+1,ur}^{(i)} = 0$	$y_{N,ur}^{(i)} = 0$	$y_{n,ur}^{(i)} = qg_{n+1,m} y_{n+1,r}^{(i)} + uqg_{n+1,m} y_{n+1,ur}^{(i)} - q^2 h_{n+2,m} y_{n+2,ur}^{(i)}$
$y_{N+1,rr}^{(i)} = 0$	$y_{N,rr}^{(i)} = c_N^{(i)}(N+1)(N+2)$	$y_{n,r}^{(i)} = c_n^{(i)}(n+1)(n+2) + uqg_{n+1,m} y_{n+1,rr}^{(i)} - q^2 h_{n+2,m} y_{n+2,rr}^{(i)}$

Table 5: Definition of the v terms involved in the sums over the orders to obtain V and its derivatives. The subscript $_{..,uu}$ means for example that the corresponding term is employed in the computation of the second derivative of V with respect to u.

$v_m^{(i)} = y_m^{(i)} p_m$	$v_{m,u}^{(i)} = y_m^{(i)} \frac{dp_m}{du} + y_{m,u}^{(i)} p_m$
$v_{m,r}^{(i)} = y_{m,r}^{(i)} p_m$	$v_{m,\lambda u}^{(i)} = m \left(y_{m,u}^{(i)} p_m + y_m^{(i)} \frac{dp_m}{du} \right)$
$v_{m,uu}^{(i)} = y_{m,uu}^{(i)} p_m + \frac{d^2 p_m}{du^2} y_m^{(i)} + 2 y_{m,u}^{(i)} \frac{dp_m}{du}$	$v_{m,\lambda r}^{(i)} = m y_{m,r}^{(1)} p_m$
$v_{m,ur}^{(i)} = y_{m,r}^{(1)} \frac{dp_m}{du} + y_{m,ur}^{(1)} p_m$	$v_{m,rr}^{(i)} = y_{m,rr}^{(i)} p_m$

We implemented this algorithm into a Fortran90 computer programme named *CLENSHAW* that, given the fully normalized Stokes coefficients of the gravity model and

Table 6: The geopotential V and its first and second order partial derivatives with respect to spherical coordinates according to the Clenshaw summation scheme.

$V = \frac{\mu}{r}\sum_{m=0}^{N}\left(v_m^{(1)}\cos m\lambda + v_m^{(2)}\sin m\lambda\right)$	$\partial_\lambda V = -\frac{\mu}{r}\sum_{m=0}^{N} m(v_m^{(1)}\sin m\lambda - v_m^{(2)}\cos m\lambda)$
$\partial_\varphi V = \frac{\mu\cos\varphi}{r}\sum_{m=0}^{N}\left(v_{m,u}^{(1)}\cos m\lambda + v_{m,u}^{(2)}\sin m\lambda\right)$	$\partial_r V = -\frac{\mu}{r^2}\sum_{m=0}^{N}\left(v_{m,r}^{(1)}\cos m\lambda + v_{m,r}^{(2)}\sin m\lambda\right)$
$\partial_{\lambda\lambda} V = -\frac{\mu}{r}\sum_{m=0}^{N} m^2(v_m^{(1)}\cos m\lambda + v_m^{(2)}\sin m\lambda)$	$\partial_{\lambda\varphi} V = -\frac{\mu\cos\varphi}{r}\sum_{m=0}^{N}\left(v_{m,\lambda u}^{(1)}\sin m\lambda - v_{m,\lambda u}^{(2)}\cos m\lambda\right)$
$\partial_{\varphi\varphi} V = \frac{\mu\cos^2\varphi}{r}\sum_{m=0}^{N}\left(v_{m,uu}^{(1)}\cos m\lambda + v_{m,uu}^{(2)}\sin m\lambda\right) - \frac{\mu\sin\varphi}{r}\sum_{m=0}^{N}\left(v_{m,u}^{(1)}\cos m\lambda + v_{m,u}^{(2)}\sin m\lambda\right)$	$\partial_{\lambda r} V = \frac{\mu}{r^2}\sum_{m=0}^{N}\left(v_{m,\lambda r}^{(1)}\sin m\lambda - v_{m,\lambda r}^{(2)}\cos m\lambda\right)$
$\partial_{\varphi r} V = -\frac{\mu\cos\varphi}{r^2}\sum_{m=0}^{N}\left(v_{m,ur}^{(1)}\cos m\lambda + v_{m,ur}^{(2)}\sin m\lambda\right)$	$\partial_{rr} V = \frac{\mu}{r^3}\sum_{m=0}^{N}\left(v_{m,rr}^{(1)}\cos m\lambda + v_{m,rr}^{(2)}\sin m\lambda\right)$

the local spherical coordinates λ_k, φ_k, r_k of K observation points P_k ($k = 1, ..., K$ and $K \geq 1$), determines the gravitational potential and its first and second gradients. Best performance is reached by first evaluating and storing the normalization coefficients f_n, g_{nm} and h_{nm}, and then computing the latitude-dependent quantities, i.e., the sectorials $\overline{P}_{mm}$, their derivatives $d\overline{P}_{mm}/du$ and $d^2\overline{P}_{mm}/du^2$ and the various recursions on the y coefficients (Table 4); then, for each λ_k the sums listed in Table 6 are accumulated. This arrangement offers higher efficiency when dealing with data distributed on a spherical grid and accessed per parallel.

7 Numerical tests

We performed a set of numerical tests on the following computer programmes:

1a. *LEGENDRE_a* (Fantino and Casotto, FC) implementing the FCR algorithm based on fnALFs in Fortran90 (Section 3);

1b. *LEGENDRE_b* (PoliMi) implementing the FCR algorithm based on fnALFs as a DLL running under Matlab (Section 3);

2. *PINES* (FC) implementing the FCR algorithm based on fnHPs in Fortran90 (Section 4);

3. *METRIS* (Metris et al.) implementing a downward recursion on solid spherical harmonics in Fortran77 (Section 5);

4. *CLENSHAW* (FC) implementing the Clenshaw summation on fnALFs in Fortran90 (Section 6).

All programmes have been provided with an interface which allows to select the simulation parameters: the intervals (N_1, N_2) and (M_1, M_2) of spherical harmonic degrees and orders to be considered, the gravity model (as a set of fully normalized Stokes coefficients) and the type of input for the observation points, to be chosen between:

- spherical grid at constant heigth h, extending over the longitude and latitude intervals (λ_s, λ_f) and (φ_s, φ_f) with resolution $\Delta\lambda$ and $\Delta\varphi$ respectively;
- previously computed positions over a satellite orbit and provided in the form of binary input data.

Three simulation configurations have been adopted:

a) GRID: spherical grid of 64440 uniformly distributed observation points; simulation parameters: $h = 250\ km$, $\lambda_s = -179^o$, $\lambda_f = 180^o$, $\Delta\lambda = 1^o$, $\varphi_s = -89^o$, $\varphi_f = 89^o$, $\Delta\varphi = 1^o$; gravity model: EGM96; $N_1 = 0$, $N_2 = 360$, $M_1 = 0$, $M_2 = 360$; simulated quantities: V, the three physical components of ∇V and the six physical components of $\nabla\nabla V$;

b) ORBIT1: positions over a simulated orbit (Fig. 4) with semimajor axis of 6628 km, eccentricity of 0.002, inclination of 96.5^o - corresponding to the orbital parameters of the GOCE mission (ESA, 2000; Albertella et al., 2002) - and angular elements precessing due to J_2; the considered mission extends over $2 \cdot 10^6$ s and is sampled at an interval of 31 s; gravity model: EGM96; $N_1 = 0$, $N_2 = 360$, $M_1 = 0$, $M_2 = 360$; number of field points: 64440; simulated quantities: V, the three physical components of ∇V and the six physical components of $\nabla\nabla V$;

c) ORBIT2: same as ORBIT1 but with a sampling rate of 1 observation per second, as in the GOCE mission, resulting in $2 \cdot 10^6$ simulation points.

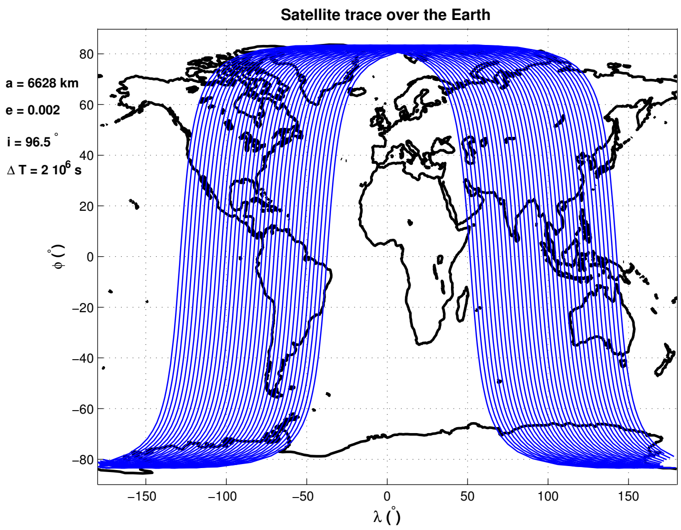

Figure 4: Ground track of a simulated satellite orbit over the surface of the Earth.

All numerical tests have been run on a Pentium IV personal computer with 500 MB of RAM and 1.3 GHz of processor speed.

Following the example of Holmes and Featherstone (2002), we have assessed the relative merits of the five programmes by testing their efficiency, precision and accuracy:

Table 7: Execution times of the five codes for the three chosen simulation scenarios. Note that *LEGENDRE_b* is interpreted, while the remaining software codes are all compiled; this may explain its low performance. The execution times of ORBIT2 have been extrapolated by scaling the performance of ORBIT1 according to the different number of observation points.

CPU execution times						
	GRID		ORBIT1		ORBIT2	
Programme	seconds	hours	seconds	hours	seconds	hours
LEGENDRE_a (FC)	2390	0.7	2079	0.6	64449	17.9
LEGENDRE_b (PoliMi)	9793	2.7	9975	2.8	309225	85.9
PINES (FC)	5275	1.5	6306	1.8	195486	54.3
METRIS (Metris et al.)	3271	0.9	3418	0.9	105958	29.4
CLENSHAW (FC)	8	-	992	0.3	30752	8.5

the tests of efficiency compare the execution (CPU) times; the tests of numerical precision compare the numerical values of the gravitational potential V, the three components of ∇V and the six components of $\nabla\nabla V$ as computed in quadruple (REAL*16) and double (REAL*8) floating point precision; the tests of accuracy employ exact analytic identities to perform self-validation of each individual code.

7.1 Numerical efficiency

The execution times of the first two simulation scenarios (i.e., GRID and ORBIT1), supplemented by extrapolated estimates for the CPU times of the third case (ORBIT2), are shown in Table 7, which gives the performance of each algorithm in seconds and hours. These execution times include I/O operations, which, however, are arranged in an efficient way: the gravity tensor quantities are stored in binary files made up of 179 records of 360 double precision numbers each and the output is updated per record. The use of binary output is efficient also from the viewpoint of storage space. The performance of the algorithm of Clenshaw on the GRID is three orders of magnitude better than all the others: this is due to the very favourable arrangement of the computations, which requires partial sums over the orders only.

7.2 Numerical precision

The numerical agreement among the results produced by each code has been verified by first expressing all tensor components in the same coordinate system: since three codes provide results in spherical coordinates and two work in cartesian coordinates, we have chosen to transform from cartesian to spherical cooordinates (Tables 1 and 2).

The assessment of numerical precision has been obtained by compiling the method of Clenshaw in quadruple floating point precision (*CLENSHAW**16) and then computing the relative differences with each algorithm in double floating point precision (i.e., *LEGENDRE_a**8, *LEGENDRE_b**8, *PINES**8, *METRIS**8 and *CLENSHAW**8). The adopted simulation configuration is GRID. The number of coinciding decimal digits in each pair is shown in Figs. 5 to 9: the level of agreement within each pair

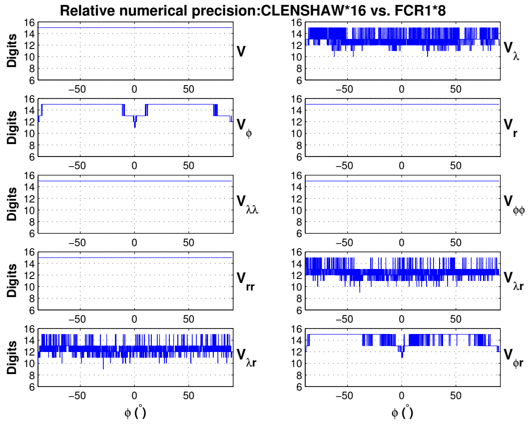

Figure 5: Relative numerical precision between *CLENSHAW*∗16 and *LEGENDRE_a*∗8 (denoted FCR1∗8 in the plot).

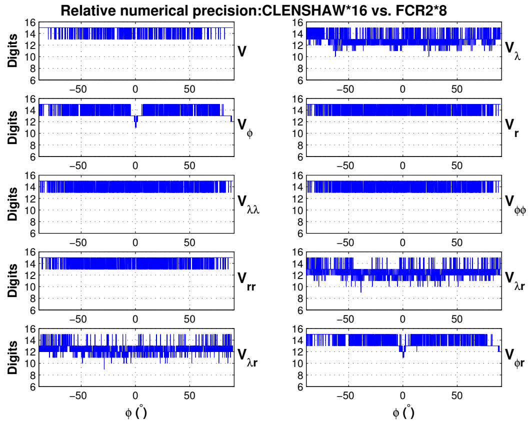

Figure 6: Relative numerical precision between *CLENSHAW*∗16 and *LEGENDRE_b*∗8 (denoted FCR2∗8 in the plot).

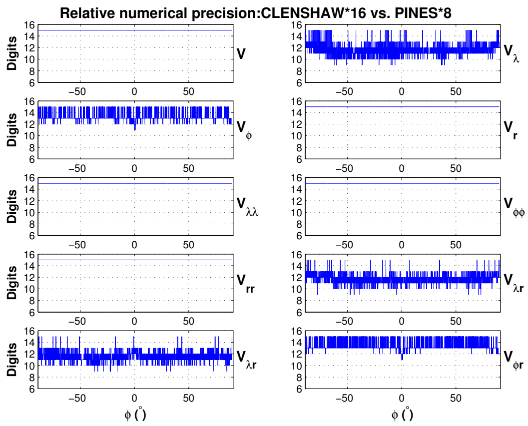

Figure 7: Relative numerical precision between *CLENSHAW*∗16 and *PINES*∗8.

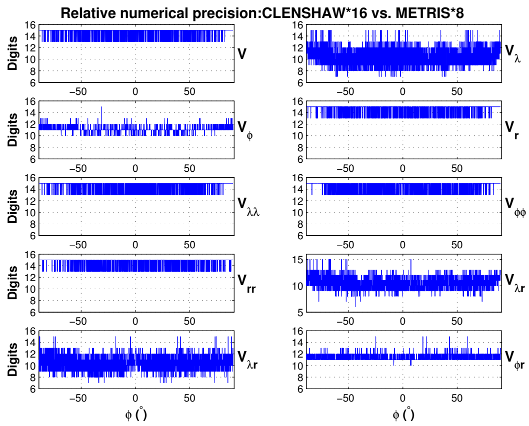

Figure 8: Relative numerical precision between *CLENSHAW*∗16 and *METRIS*∗8.

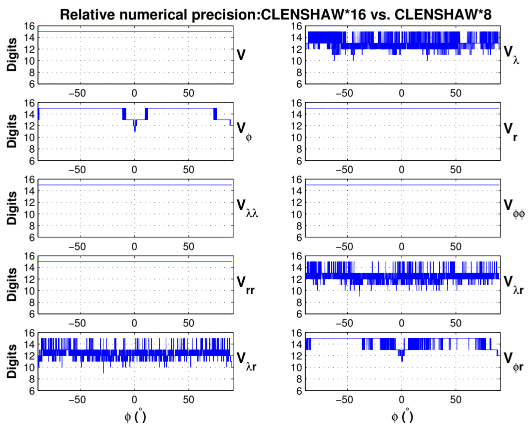

Figure 9: Relative numerical precision between *CLENSHAW*∗16 and *CLENSHAW*∗8.

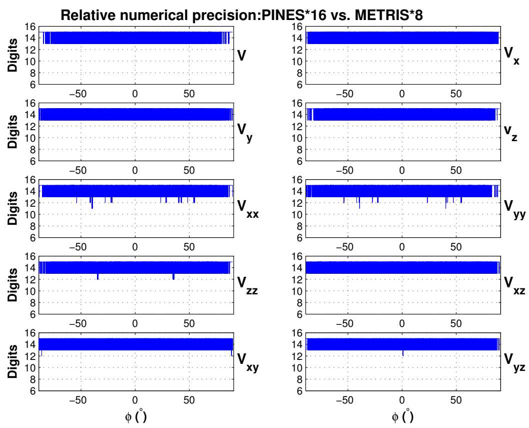

Figure 10: Relative numerical precision between *PINES*∗16 and *METRIS*∗8.

shows variations with the specific tensor component considered and ranges from 10 to 15 decimal digits in the case of the algorithms developed in spherical coordinates (*LEGENDRE_a*∗8, *LEGENDRE_b*∗8 and *CLENSHAW*∗8), while it can get as low as 7 decimal digits in the case of *METRIS*∗8. We believe that the poor agreement between *CLENSHAW*∗16 and *METRIS*∗8 is not due to error propagation resulting from the coordinate transformations. However, a direct comparison between *METRIS*∗8 and *PINES*∗8 shows that the two algorithms are in very good agreement (Fig. 10). We believe that the issue of numerical precision should be further investigated.

7.3 Numerical accuracy

The accuracy of the computations performed by each programme can be verified by computing the values of exact identities incorporating specific tensor components. The most important and well known of these is the Laplace identity:

$$\sum_{\alpha=1}^{3} V_{\alpha\alpha} = 0 \tag{31}$$

which relates the diagonal elements of the second gravity gradient tensor. Other exact relations involve finite sums of the ALFs and their derivatives; for example:

$$\sum_{n=0}^{N}\sum_{m=0}^{n}\left[\overline{P}_{nm}(\varphi)\right]^2 = (N+1)^2 \tag{32}$$

and

$$\sum_{n=0}^{N}\sum_{m=0}^{n}\left[\frac{\partial \overline{P}_{nm}(\varphi)}{\partial\varphi}\right]^2 = \frac{N(N+2)(N+1)^2}{4}. \tag{33}$$

We evaluated Eq. (31) with all five computer codes and Eqs. (32) and (33) with *LEGENDRE_a* only. We found that all algorithms verify Eq. (31) with results of the order of 10^{-18} or 10^{-19}; *LEGENDRE_a* reproduces the identities (32) and (33) with accuracies at the level of 10^{-14} and 10^{-13} respectively.

8 Conclusions

We have described, tested and compared four numerical algorithms for spherical harmonic synthesis applied to the evaluation of the gravitational potential and its first and second gradients.

The method of Pines is computationally heavy also when running on a spherical grid: this is due to the large number of longitude-dependent auxiliary functions to be evaluated. The apparently low performance of *LEGENDRE_b* both on the grid and on the orbit might simply be an effect of the mode (interpreted rather than compiled) in which it runs. The performance of the algorithm of Clenshaw on the GRID is three orders of magnitude better than all the others: this is due to the very favourable arrangement of the computations, which requires partial sums over the orders only. The precision and accuracy of the methods considered is good in most cases, although some aspects of the tests on numerical precision deserve to be investigated further.

We conclude that the algorithm of Clenshaw is by far the most efficient and therefore the most suitable for implementation and use when dealing with large amounts of observations.

Acknowledgements

We thank F. Sansò and M. Reguzzoni for providing their software and for helpful suggestions.

References

Abramowitz M, Stegun IA (1964) Handbook of Mathematical Functions with Formulas, Graphs, and Mathematical Tables. Dover Publications, New York

Albertella A, Migliaccio F, Sansò F (2002) GOCE: the Earth gravity field by space gradiometry. Cel Mech & Dynam Astron 83: 1-15

Balmino G, Barriot JP, Valès N (1990) Non-singular formulation of the gravity vector and gravity gradient tensor in spherical harmonics. Manuscr Geod 15: 11-16

Bettadpur SV, Schutz BE, Lundberg JB (1992) Spherical harmonic synthesis and least squares computations in satellite gravity gradiometry. Bull Géod 66: 261-271

Cunningham LE (1970) On the computation of the spherical harmonic terms needed during the numerical integration of the orbital motion of an artificial satellite. Cel Mech & Dynam Astron 2: 207-216

Ditmar P, Klees R (2002) A Method to Compute the Earth's Gravity Field from SGG/SST data to be Acquired by the GOCE Satellite. Technical report

ESA (2000) From Eötvös to Milligal. Final Report

Heiskanen WA, Moritz H. (1967) Physical Geodesy. Freeman, San Francisco

Hobson EW (1965) The theory of spherical and ellipsoidal harmonics. Chelsea Publishing Company, New York

Holmes SA, Featherstone WE (2002) A unified approach to the Clenshaw summation and the recursive computation of very high degree and order normalized associated Legendre functions. J Geod 76: 279-299

Ilk KH (1983) Ein Beitrag zur Dynamik ausgedehnter Körper - Gravitationswechselwirkung. PhD thesis, Bayerischen Akademie der Wissenschaften, Munchen

Metris G, Xu J, Wytrzyszczak I (1999) Derivatives of the gravity potential with respect to rectangular coordinates. Cel Mech & Dynam Astron 71: 137-151

Pines S (1973) Uniform representation of the Gravitational Potential and its Derivatives. AIAA Journal 11/11: 1508-1511

Press WH, Teukolsky SA, Vetterling WT, Flannery BP (1992) Numerical Recipes in Fortran 77. Cambridge University Press

Spencer JL (1976) Pines' nonsingular gravitational potential derivation, description and implementation. Technical report, NASA Contract No. 9-13970

Tscherning CC, Poder K (1982) Some Geodetic applications of Clenshaw summation. Boll Geod Sci Aff, XLI/4: 349-375

Xu G (2003) GPS - Theory, Algorithms and Applications. Springer-Verlag, Berlin

On the Potential of Wavelets for Filtering and Thresholding Airborne Gravity Data

M. El-Habiby, M. G. Sideris
Department of Geomatics Engineering,
The University of Calgary, 2500 University Drive N.W., Calgary, Alberta, Canada, T2N 1N4

Abstract. Wavelets can be used in the decomposition and analysis of airborne gravity data. In this paper, multiresolution analysis is applied to de-noise gravity disturbance and different de-noising techniques are studied. The first objective is testing the usefulness of wavelets for analyzing and filtering airborne gravity data. The second one is a comparison between the usage of the wavelet transform and other well known low-pass filters. The gravity disturbances are filtered using wavelet thresholding to remove the noise introduced by the dynamics of the aircraft. Two procedures have been tested. The first one is de-noising using minimax and universal techniques. The second one is a combination of wavelet thresholding and filtering at certain levels. Comparison to independent reference data is performed in the area of interest to determine the external accuracy of this approach. Results from both cases and from the low-pass filter approach are compared. The results of testing different de-noising techniques show that the combination of thresholding and filtering can reach RMS values equal to 25 mGal in comparison to the results from the 90s low-pass filter.

Keywords. Wavelet multiresolution analysis; airborne gravimetry; filtering; universal, hard and soft thresholding.

1 Introduction

Wavelet analysis is a comparatively young branch in signal processing. It is developed to overcome some of the problems of Fourier analysis. Wavelet expansions allow better local description and decomposition of signal characteristics. Filtering airborne gravimetry data has been introduced in a number of publications. Glennie and Schwarz (1997), Schwarz and Glennie (1998), Glennie and Schwarz (1999), Wei and Schwarz (1998), and Glennie (1999) low-pass filtered gravity disturbances using an FIR filter to specified cut-off filter lengths, which range from 30s to 120s.

Bruton et al. (1999) used wavelets for the analysis and de-noising of kinematic geodetic measurements. Wavelets have been used as a de-noising tool for removing stochastic noise from different geodetic signals. They used SURE (Stein Unbiased Estimate of Risk) soft thresholding and tested the Daubechies family in the decomposition of the signal. Abdel-Hamid et al. (2004) improved the performance of MEMS-based sensors using multiresolution analysis. They concentrated on enhancing the performance of Kalman-filtering INS/GPS integration techniques.

Our objective in this paper is to check the effectiveness of using wavelets in de-noising gravity disturbance. Different thresholding techniques will be tested. Minimax thresholding, fixed thresholding (universal), and thresholding combined with filtering at certain levels will be used. Hard and soft thresholding have been used in parallel with the different thresholding techniques.

In the next section, wavelets are introduced as a filtering tool. Then the system, flight and data characteristics are described. This is followed by the analysis of the data using wavelets and FFT. Following that the results of de-noising the gravity disturbance data using different wavelet thresholding techniques are compared with reference data and a comparison is made between the different thresholding and filtering techniques. The paper ends with conclusions, recommendations and future work with respect to the suitability, accuracy and efficiency of the methods used.

2 Wavelets as a Filtering Tool

A wavelet base is a set of building blocks to construct or represent a signal or function; Burrus et al. (1998). The discrete wavelet transform (DWT) coefficients $\omega_{j,k}$ of a signal or a function $f(t)$ are calculated by the inner product

$$\omega_{j,k} = \langle f(t), \psi_{j,k}(t) \rangle \tag{1}$$

where $\psi_{j,k}$ is the wavelet expansion function, and both j is the scale and k is the translation and both are integer indices. The inverse wavelet transform is used for the reconstruction of the signal from the wavelet coefficients $\omega_{j,k}$ by

$$f(t) = \sum_j \sum_k \omega_{j,k} \psi_{j,k}(t) \tag{2}$$

Equations (1) and (2) are named analysis and synthesis, respectively. Wavelets used in this paper have energy concentrated in time, continuous null moments, and decrease quickly towards zero when the input tends to infinity. Meyer and Daubechies wavelets have been used in this research (Figure 1). Both the wavelet and scaling function for Meyer are defined in the frequency domain and have a closed form. Meyer is not compactly supported, nevertheless, it introduces a good approximation leading to FIR filters, and then allowing DWT, (Misiti et al., 2002). Daubechies (db) wavelets have no explicit expression except of db1 (Haar wavelet).

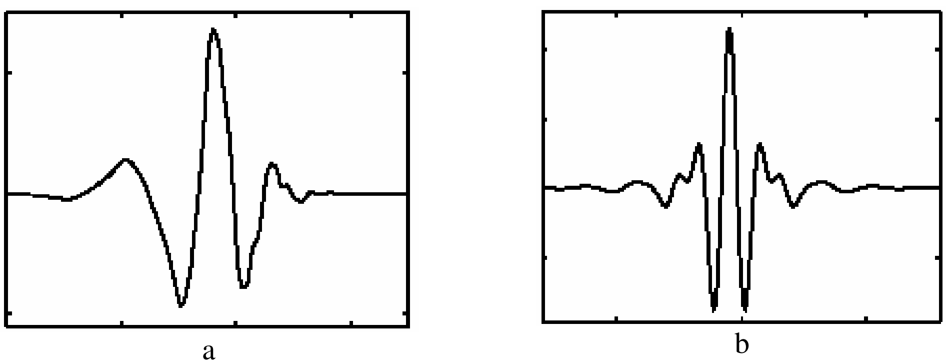

Fig. 1 Daubechies 4 wavelet (a) and Meyer wavelet (b) (Misiti et al., 2002)

2.1 Wavelet Thresholding

Wavelet thresholding is a technique used to remove random noise and outliers from the signal before reconstruction. Wavelet absolute coefficients larger than a certain specified threshold δ are the ones that should be included in reconstruction. The reconstructed function can be show as, (Ogden, 1997):

$$\hat{f}(t) = \sum_j \sum_k I_{\{|\omega_{j,k}|>\delta\}} \omega_{j,k} \psi_{j,k}(t) \tag{3}$$

where $I_{\{|\omega_{j,k}|>\delta\}}$ is the indicator function of this set. This represents a keep or kill wavelet reconstruction. This thresholding is a kind of nonlinear operator on the wavelet coefficients vector. This leads to a resultant vector of estimated coefficients $\hat{\omega}_{j,k}$ to be used in the reconstruction process. The problem is always about finding the proper thresholding value. In order to make this decision, two main parameters have to be taken into account. These parameters are the sample size $\boldsymbol{n}$ and the noise level σ^2. The estimated coefficients can be determined from either hard thresholding or soft thresholding. In case of hard thresholding the estimated coefficients will be:

$$\hat{\omega}_{j,k} = \begin{cases} \omega_{j,k} & if \ \left|\omega_{j,k}\right| \geq \delta \\ 0 & otherwise \end{cases} \tag{4}$$

In case of soft thresholding, the estimated coefficients will be:

$$\hat{\omega}_{j,k} = \begin{cases} \omega_{j,k} - \delta & if \ \left|\omega_{j,k}\right| \geq \delta \\ 0 & if \ \left|\omega_{j,k}\right| \leq \delta \\ \omega_{j,k} + \delta & if \ \omega_{j,k} < -\delta \end{cases} \tag{5}$$

This can also be illustrated in the following figure.

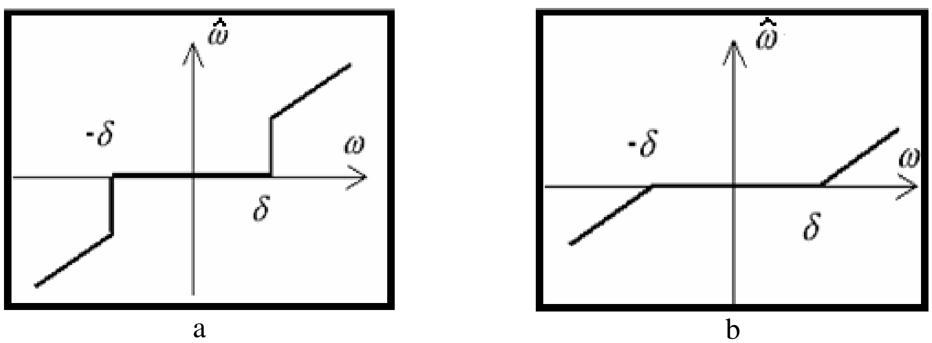

Fig. 2 (a) Hard and (b) soft thresholding

Choosing the value of the threshold is a very fundamental problem in order to avoid oversmoothing or undersmoothing.

Minimax thresholding has been applied in this research. This technique depends on the sample size $\boldsymbol{n}$ and it minimizes a bound for the risk involved in estimating a function. Minimax threshold has no closed form, but it can be approximated numerically. Another thresholding technique has been used in this research; it is called universal thresholding (fixed thresholding). This is an alternative to the minimax technique. The thresholding value is chosen equal to $\sqrt{2\, log\, n}$. This thresholding value is larger than the corresponding value in the minimax estimate, for the same sample size; for more details, see Donoho and Johnstone (1994).

2.2 Wavelet Level-dependent Thresholding and Filtering

Filtering is adjusting all the coefficients of certain level or levels to zero:

$$\hat{\omega}_{j,k} = \begin{cases} \omega_{j,k} & if \ \ j \leq j_{max} \\ 0 & if \ \ j \geq j_{max} \end{cases} \tag{6}$$

In this research, filtering has been combined with thresholding for de-noising gravity disturbances. First, either minimax or universal thresholding is applied to the signal. This is followed by applying filtering to a number of the high wavelet decomposition levels. The choice of the wavelet decomposition level to be filtered depends on the minimum wavelength of signal that can be reconstructed from each level. Sometimes both filtering and level-dependent thresholding are used, which means that a possibly different threshold value is chosen for each wavelet level *j*, (Barthelmes et al., 1994).

3 System, Flight and Data Description

The data used originated from a project collected by the University of Calgary on 9, 10, and 11 of September, 1996. Only the data of the second day has been used in this research. The hardware used consists of three main components: a strapdown INS, GPS master and remote stations, and data acquisition. The INS system is a Honeywell LASEREFIII (LRFIII) navigation grade inertial system. Various types of GPS receivers have been used. The major requirements were low noise and high reliability. The data was collected over the Rocky Mountains; the area covered was 100 km * 100 km. This area was covered by 14 lines in day 2, as shown in Figure 3.

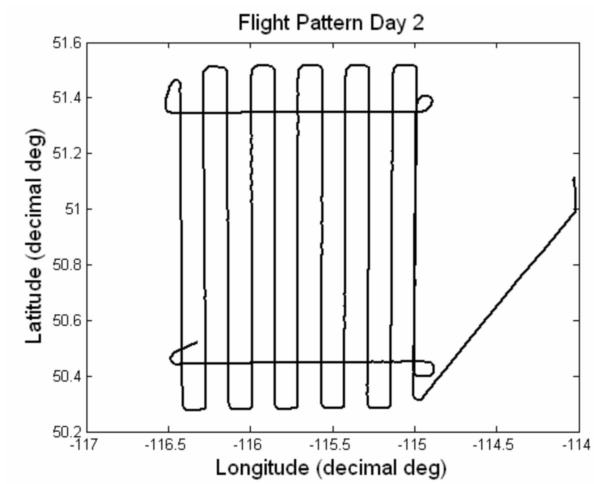

Fig. 3 Flight pattern for day 2 (September 10th) of the Kananaskis Campaign

This area was chosen because of the high variability of the gravity field and the availability of dense ground gravity values to be used as reference. The reference data were upward continued gravity disturbances with RMS equal to 1.5 mGal. The heights of the terrain in the area vary from 800 m to 3600 m. Average ellipsoidal flight height was 4357 m. The flight speed was 360 km/hr. The data used in the de-noising procedure has been resampled to 1 Hz (01 h bandlimit).

4 Analysis and De-noising of Results

4.1 Wavelet versus FFT analysis

The data to be analyzed is a gravity disturbance with 1h bandlimit, introduced as sub output from the KINematic Geodetic Software for Position and Attitude Determination (KINGSPAD) software, figure 4.

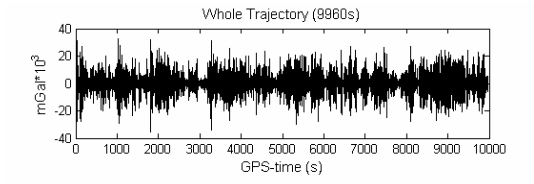

Fig. 4 Gravity disturbance with 1 Hz sampling rate

The gravity disturbance analysis (Figure 5a) starts with the demonstration of (1h bandlimit) signal using Fourier analysis. The FFT was used to visualize the different frequency contents of the signal. This spectrum shows that there are different signals at different frequencies, but the problem is that it is difficult to localize the errors, and separate them from the signal (figure 5a). The deficiency of time localization by FFT analysis leads to the use of wavelet transform analysis.

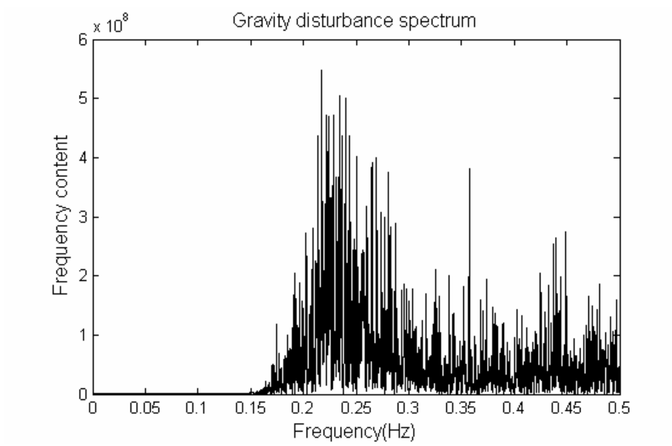

(a)

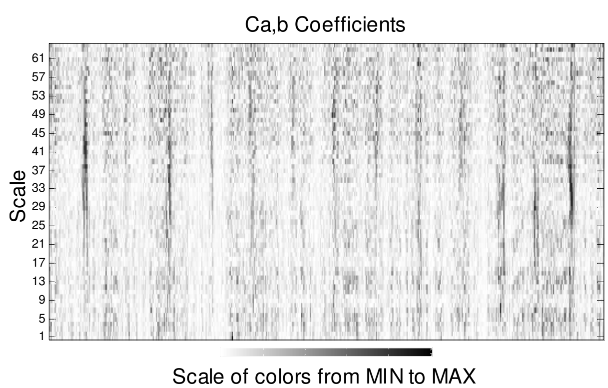

(b)

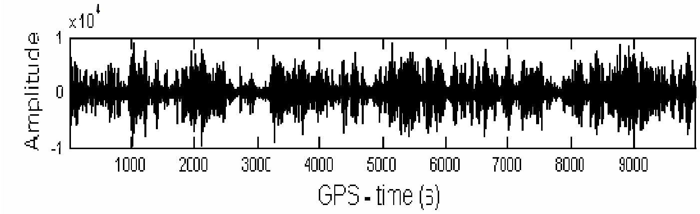

(c)

Fig. 5 (a) FFT spectrum shows a number of undesired frequencies. **(b)** Time-frequency analysis and localization using continuous wavelet transform. **(c)** Coefficients Line - $\omega_{j,k}$ for scale j = 32 (frequency = 0.031).

The usage of the continuous wavelet transform allows time-frequency localization; this can be seen in Figure 5b. Continuous here means that it is not decimated to dyadic format (decreasing the number of coefficients into half at each approximation or detailed level) as in the traditional discrete cases. However, all the wavelet decomposition coefficients are taken into account. Darker shades show high frequencies, different from the expected gravity disturbances frequencies (depending on a priori information). These high frequencies are interpreted as errors at certain time and scale. In wavelet analysis, different types of errors can be tracked through the whole trajectory and interpreted corresponding to different aircraft dynamics. Also, by the decomposition of the signal into several levels, stochastic errors and outliers can be easily detected and removed using different thresholding techniques. For example, the takeoff and different maneuver periods between lines can be easily identified. Figure 5c is a sample of the coefficients at scale 32 showing clearly the maneuvers between lines.

4.2 Wavelet versus low-pass filter

Wavelet transforms have been also used in de-noising and smoothing of gravity disturbances. The wavelet techniques are compared to the output of a low-pass filter with four cut-off lengths, which are 30s, 60s, 90s, and 120s. The difference between output computed raw data and the reference data shows the presence of noise and outliers, as shown in figure 6. The four low-pass filters are an output from the KINGSPAD and AGFILT software, developed by the University of Calgary.

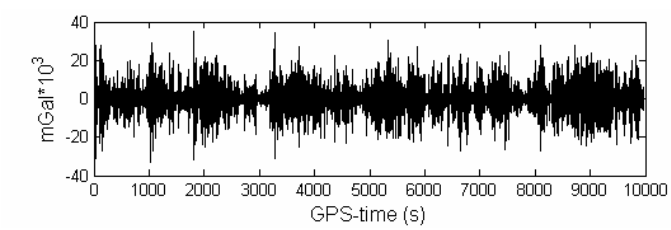

Fig. 6 Deference between reference and bandlimited 1h data

The difference between the output from the four low-pass filters and the reference data is shown in Figure 7. The RMS of the difference between the low-pass filtered data and the reference has been computed.

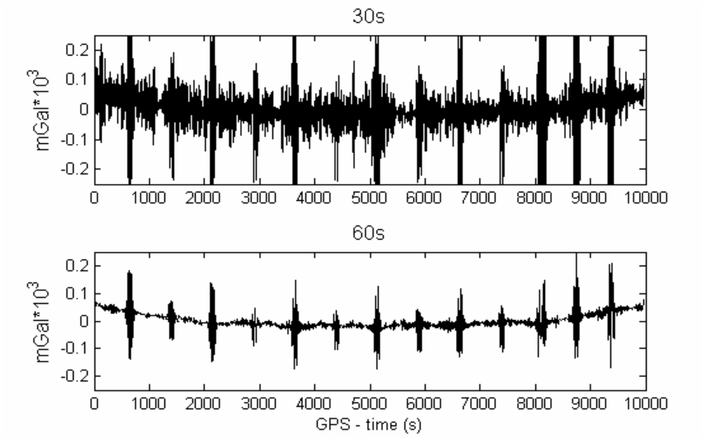

(a)

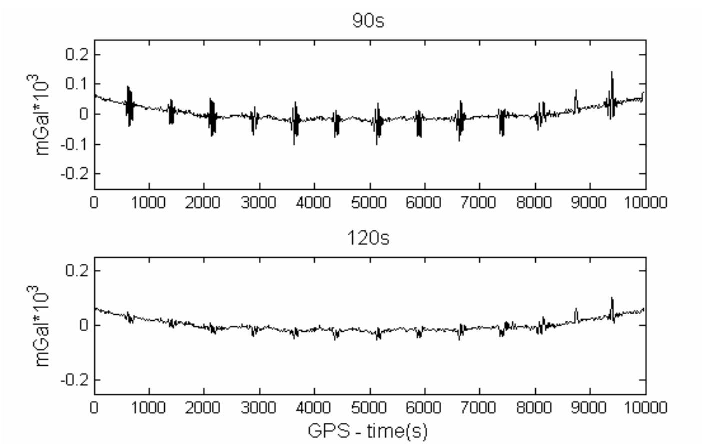

(b)

Fig. 7 (a) Difference between reference data and 30s, and 60s low pass filter output. **(b)** Difference between reference data and 90s, and 120s low pass filter output.

The same data was de-noised using different thresholding and filtering techniques, using the two wavelet families shown in Figure 1. Finally, they are compared with the results obtained from the four low-pass filters.

The universal and minimax thresholding has been applied to the gravity disturbance data. Both of them have been applied with soft and hard thresholding. The results are compared to the reference data. The RMS of the residuals ranges between 712 and 1700 mGal, which is not acceptable (Figure 8).

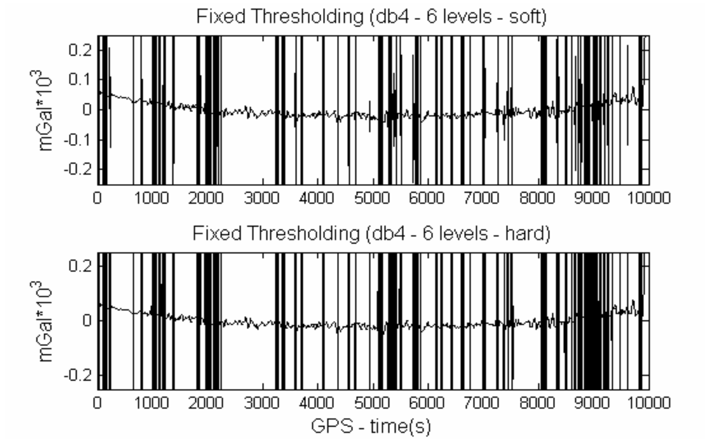

(a)

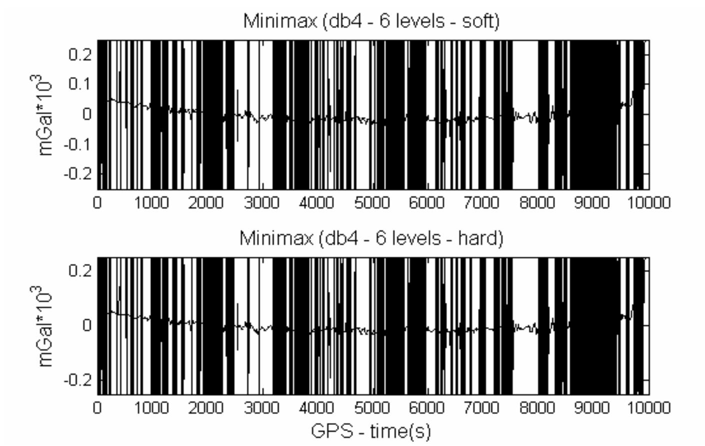

(b)

Fig. 8 (a) Difference between the gravity disturbances de-noised by universal (fixed) thresholding and the reference data **(b)** Difference between the gravity disturbances de-noised by minimax thresholding and the reference data

Two modifications have been made to reduce this difference. Another wavelet family has been tested and filtering has been applied to the data in sequence with the two thresholding techniques mentioned before. After different trials and tests, it has been found that the usage of minimax soft thresholding, by Meyer wavelets followed by filtering at certain high levels of the wavelet decomposition, is the optimum in our case study.

In the following figures it can be seen that universal thresholding has been tested with Meyer wavelets. The RMS was 729 mGal, which is still not acceptable. This is followed by three trials of applying the minimax soft thresholding, and applying filtering by removing a whole decomposition level at a certain scale. The value of the RMS decreased from 1846 mGal, because of inappropriate choice of the filtering level, at the first trial to 25 mGal at the third trial. This value is close to the best result introduced by low-pass filtering (120s). This can be illustrated in figure 9.

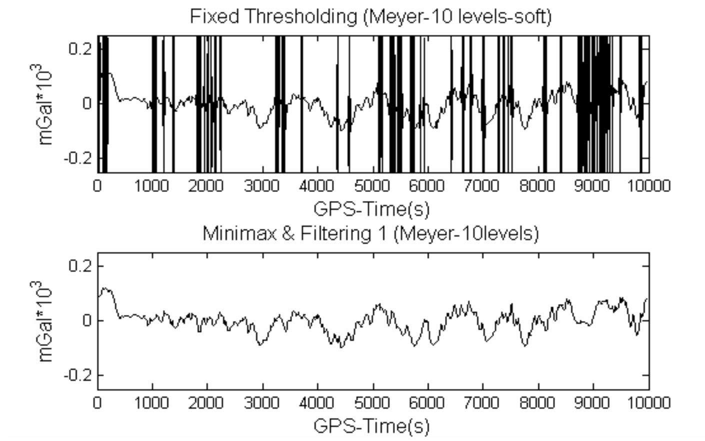

(a)

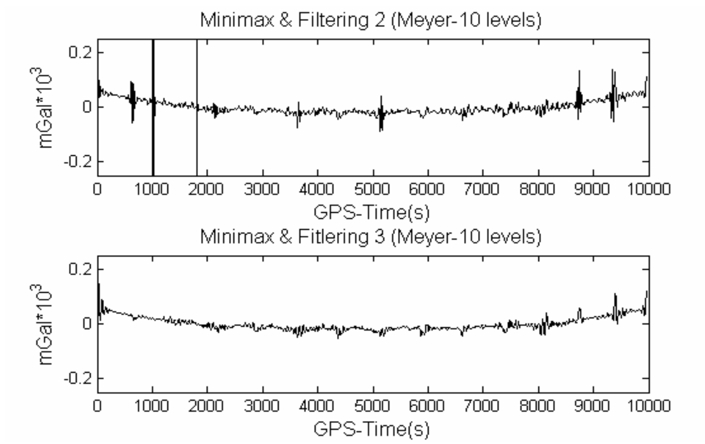

(b)

Fig. 9 (a) Meyer wavelets with fixed soft thresholding (up), and minimax and filtering (1st trial) down. **(b)** Meyer wavelets with minimax and filtering 2^{nd} (up), and 3^{rd} (down) trial

Table 1 RMS of the difference between de-noised gravity disturbances and reference data

Method	RMS (mGal)
Low pass filter (30s)	99.52
Low pass filter (60s)	37.45
Low pass filter (90s)	26.68
Low pass filter (120s)	23.71
Minimax & filtering 1	1846.80
Minimax & filtering 2	82.86
Minimax & filtering 3	25.52

The choice of the thresholding value is depending on the sampling rate and the signal that can be reconstructed at each level. It is automated through one of the two techniques mentioned above, either universal or minimax thresholding. Applying filtering to certain levels is very dangerous, needs a prior information and is depending on trial and error. The same procedure was applied to one of the 14 lines, which is line 6 between 4725 s and 5280 s. The first and last 10 points, which contain a lot of outliers because of the dynamics introduced from the turning maneuvers of the aircraft, have been removed. Similar results were obtained The only difference is that, in case of line 6, less usage of filtering was required because of the stability of the aircraft during this period. It is worth mentioning here that a trend has been removed from the difference of the de-noised and the referenced data, in both cases (low-pass filter, and different wavelet procedures). The RMS errors from different trials and approaches for the difference between the de-noised gravity disturbance and reference data are summarized in table 1.

5 Conclusions

Wavelets can be used in the decomposition and analysis of airborne gravimetry data. Minimax and fixed thresholding techniques as an automated procedure are not enough for de-noising airborne gravity data, because of the need of filtering high frequency levels. The combination of these automated thresholding techniques with filtering is more effective in de-noising and bandlimiting the gravity disturbance. Soft thresholding proved to be more effective in this study than hard thresholding. Different wavelets have different effect on the analysis and de-noising of the signal. This can be easily noticed from the improvement in the accuracy when using Meyer wavelets instead of Daubechies. Decomposition of the signal to higher levels and applying thresholding and filtering is effective especially in the case of outliers. Wavelet de-noising reached the same accuracy as the approximation introduced by the low-pass filters with 120s cut-off, and better than the 30s, 60s, and 90s low pass filters. Trial and error is required for determining the levels to be removed (filtering) in case of combining both filtering and thresholding. Further research is under investigation to automate the filtering and thresholding procedures by combining them with priory information about the range of the frequency required.

References

Abdel-Hamid, W., A. Osman, A. Noureldin, and N. El-Sheimy (2004). Improving the performance of MEMS-based inertial sensors by removing short-term errors utilizing wavelet multi-resolution analysis. Published in the *ION National Technical Meeting*, Ca, USA, 26-28 Jan.

Barthelmes, F., L. Ballani, and R. Klees (1994). On the Application of wavelets in Geodesy. In: *"Geodetic Theory Today"*, convened and ed. by Sansò, F., Springer-Verlag Berlin, Heidelberg 1995 (International Association of Geodesy Symposia 114, L'Aquila, Italy, May 30 - June 3, pp. 394-403.

Bruton, A. M., K. P. Schwarz, and J. Skaloud (1999). The use of wavelets for the analysis and de-noising of Kinematic geodetic measurements. *Geodesy Beyond 2000-IAG General Assembly*, Birmingham, UK, July 19-24.

Burrus, C. S., R. A. Gopinath, and H. Guo (1998). Introduction to Wavelets and Wavelet Transforms: A Primer. Prentice Hall, Upper Saddle River, New Jersey, USA.

Donoho, D. L., and I. M. Johnstone (1994). Ideal Spatial Adaptation via Wavelet Shrinkage. *Biometrika* 81: pp. 425-455.

Glennie, C. (1999). An analysis of an Airborne Gravity by Strapdown INS/GPS. Ph.D. Thesis, *UCGE Report #20125*, Department of Geomatics Engineering, University of Calgary, Calgary, Canada.

Glennie, C., and K. P. Schwarz (1999). A Comparison and Analysis of Airborne Gravimetry Results from Two Strapdown Inertial .DGPS Systems. *Journal of Geodesy*, 73, Issue 6, pp. 311-321.

Glennie, C., and K.P. Schwarz (1997). Airborne Gravity by Strapdown INS/DGPS in a 100 km by 100 km Area of the Rocky Mountains. In: Proceedings of International Symposium on K*inematic Systems in Geodesy, Geomatics and Navigation (KIS97)*, Banff Canada, June 3-6, pp. 619-624.

Misiti, M. Y., G. Oppenheim and J. Poggi (2002).Wavelet Toolbox for use with Matlab. *User's Guide*, the Math Works Inc.

Ogden, R. T. (1997). Essential Wavelets for Statistical Applications and Data Analysis. *Birkhäuser*, Boston, USA.

Schwarz, K. P., and C. Glennie (1998). Improving Accuracy and Reliability of Airborne Gravimetry by Multiple Sensor Configurations. In: *proceeding of International Association of Geodesy Symposia 'Geodesy on the Move'*. Forsberg R. Feissel M. Dietrich R. (eds) Vol. 119, Springer Berlin Heidelberg New York, pp 11-17.

Wei, M., and K.P. Schwarz (1998). Flight Test Results from a Strapdown Airborne Gravity System. *Journal of Geodesy*, 72, pp. 323-332.

A comparative study of the geoid-quasigeoid separation term C at two different locations with different topographic distributions

Muhammad Sadiq [A1], **Zulfiqar Ahmad** [A2]
Department of Earth Sciences, Quaid-i-Azam University, Islamabad Post Code 45320, Pakistan
A1: sdq_geo@yahoo.com, **A2:** hash@isb.paknet.com.pk

Abstract:
The present study has been carried out to compare the geoid-quasigeoid separation in two areas of Pakistan with different topographic distributions. The height datum of Pakistan is based on the orthometric height system. Since Pakistan has a diversity of terrain distribution as regards the elevation from mean sea level due to vast expanse comprising both land and hilly areas, the emphasis of this study has been placed on the quantification of the geoid-quasigeoid separation term with respect to elevation distribution for future geoid determination. Bouguer gravity anomalies and digital terrain elevation were used to estimate the minimum/maximum separation between these two reference surfaces. This was also compared with a separation term C computed from EGM96 gravity anomalies. The statistics of the results in the two areas exhibit a one to one correspondence of EGM96 gravity anomalies with observed gravity data and digital elevation data. The area with high mountains (Kalat) has more offset between the two surfaces. The standard deviation of separation term is ~77 mm from observed and 62.5 mm from model data. In contrast with the low elevation area (Dadu), the standard deviation of the separation becomes as small as ~2 mm from observed data and ~7mm from gravity anomalies computed from the EGM96 model. The terrain correction has measurable effect on the standard deviation in Kalat and is very insignificant in Dadu area. The difference of the separation term from observed data and the model can be related to assumption of the topographic density, local mass irregularities and inherent omission error of the EGM96 model. These results also show that the separation term C is significant in Pakistan and may be required to be incorporated in the final geoidal solution.

Keywords: Geoid, Quasigeoid, Bouguer Gravity anomaly, Height Anomaly, C Term

1-Introduction:

The investigation made in this paper is a comparative study of the effect of terrain on the geoid to quasigeoid separation in two selected areas of Pakistan. This study also focuses on the issue of significance of this term with reference to Pakistan and surrounding areas for onward more feasible geodetic boundary values solution.

The geoid is an equipotential surface of the Earth that corresponds to mean sea level, whereas the quasi geoid is a geometrical surface referred to a normal height system. The geoid undulation (N) is the separation between the ellipsoid and the geoid measured along the ellipsoidal normal. The height anomaly (ζ) is the separation between the reference ellipsoid and quasigeoid along the ellipsoid normal. There is similar concept of orthometric heights (H^o) measured along plumb line whereas, normal heights (H^N) are measured along the ellipsoidal normal. These reference surfaces of the geodesy are shown in Figure 1

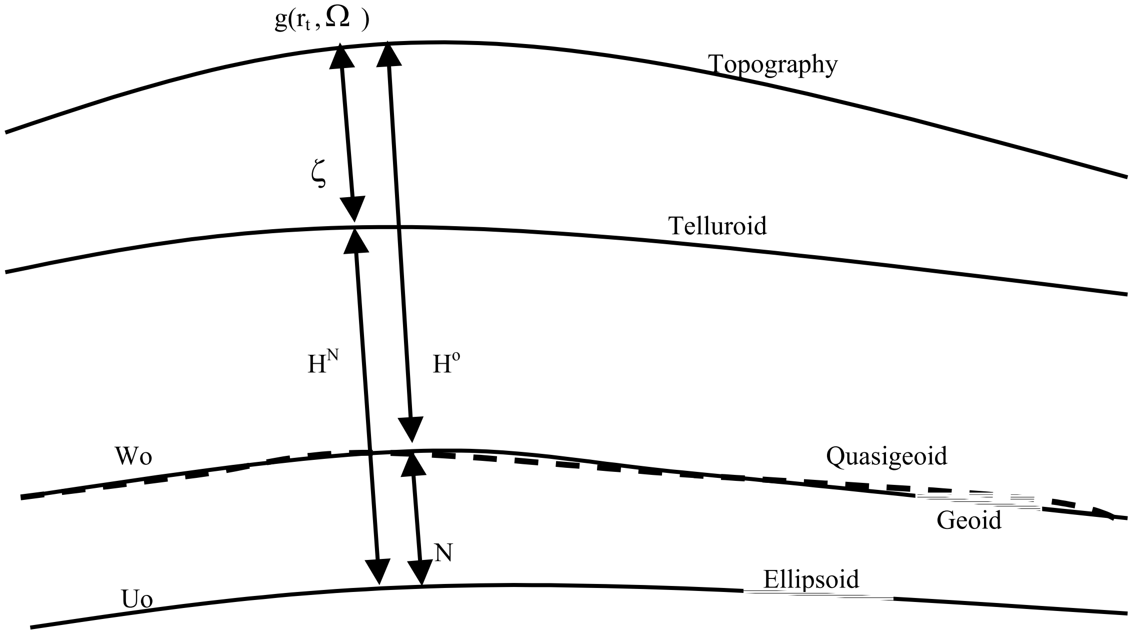

Figure-1: The geoid undulation(N), Orthometric heights (H), Height Anomaly (ζ) and Normal heights (H^N)

In this study, a comparison is made of the geoid to quasigeoid correction term for two study areas with different topographic distribution. This comparison is made with observed gravity/elevation data, gravity anomalies computed from the EGM96 global model and digital elevation model data extracted from Shuttle Radar Topographic Mission (SRTM) for these areas. The EGM96 global model is a recent estimate of the global gravity and height anomalies [Rapp (1997)]. The global correction term was determined using EGM96 potential coefficients. The Bouguer gravity anomalies and elevation data of the 3495 points in the low land area (Dadu) and 927 points in the high elevation (Kalat) area were determined from observed land gravity data while orthometric heights were determined using spirit leveling. The terrain correction was also calculated in these areas and added to the Bouguer anomaly to quantify the effect of terrain on geoid to quasigeoid separation.

2-Theoretical Background

Molodensky et al. (1962) formulated the geodetic boundary value problem on the earth surface and introduced two new surfaces called the telluroid and the quasigeoid. The quasigeoid is not an equipotential surface of the earth's gravity field and thus has no physical meaning (Heiskanen and Moritz, 1967). However, the quasigeoid can be determined somewhat more directly from surface gravity data without prior knowledge of the topographic bulk density. The separation between the reference ellipsoid and the quasigeoid is called the height anomaly and is defined as;

$$\zeta = h - H^N \tag{1}$$

The telluroid is the surface defined by plotting the points at a distance equal to ζ below the earth surface. The distance between the ellipsoid and the telluroid is called the normal height H^N and can be computed from optical leveling measurements using the integral mean of normal gravity between the reference ellipsoid and the telluroid as,

$$\bar{\gamma} = \frac{1}{H^N}\int_0^{H^N} \gamma \, dH \tag{2}$$

This equation makes it possible to determine the normal heights without prior knowledge of the topographic density distribution along the ellipsoidal normal.

The orthometric height H^o of any point on the surface of the earth is the height of point above the geoid along the geoidal normal. It can be determined by optical leveling measurement along the plumb line between the point on surface and the geoid. It requires the integral mean of the gravity along the geoidal normal and can be determined using the relationship [Heiskanen and Moritz (1967)].

$$\bar{g} = \frac{1}{H^o}\int_0^{H^o} g \, dH \tag{3}$$

However, this requires the knowledge of the subsurface density along the plumbline and this information is not available in normal routine work. For this purpose, the Poincare-Prey gravity gradient is often used. Assuming that the ellipsoidal normal and plumb line are coincident between the earth surface and the geoid, the geoid separation can be approximated by

$$\mathbf{N \cong h - H^o} \tag{4}$$

Eliminating h from Eq. 1 & 4 gives

$$\mathbf{H^N - H^o = N - \zeta \cong C2} \tag{5}$$

Where, C2 is the geoid-quasigeoid separation term. It depends on the Bouguer anomaly, average theoretical gravity and orthometric height of the point. This term can be derived as follows.

The basic formula for the definition of orthometric height is given by (Heiskanen and Moritz, 1967)

$$H^o = \frac{C[r_t(\Omega)]}{\bar{g}} \qquad \forall\Omega(\varphi,\lambda) \in \Omega_0(-\pi/2 \le \varphi \le \pi/2; 0 \le \lambda \le 2\pi) \tag{6}$$

Where $C[r_t(\Omega)]$ is the geopotential number, and $\bar{g}(\Omega)$ is the mean value of the gravity along the plumb line between geoid and earth surface determined using Poincare-Prey's gravity gradient.

The Molodensky's normal height $H^N(\Omega)$ reads (Molodensky, 1945)

$$H^N = \frac{C[r_t(\Omega)]}{\bar{\gamma}} \qquad \forall\Omega \in \Omega_o \tag{7}$$

Where $\bar{\gamma}(\Omega)$ is the mean value of normal gravity along the ellipsoidal normal between the surface of the geocentric reference ellipsoid and the telluroid.

The difference between the normal height and orthometric height can be determined by the following relation.

$$H^N - H^o = H^o(\Omega)\,\frac{\bar{g}(\Omega) - \bar{\gamma}(\Omega)}{\bar{\gamma}(\Omega)} \qquad \forall \Omega \in \Omega_o \qquad (8)$$

The difference between the mean gravity $\bar{g}(\Omega)$ and mean normal gravity $\bar{\gamma}(\Omega)$ can be determined using their mathematical definitions with some assumptions as. [Heiskanen and Moritz, 1967]

$$\bar{g}(\Omega - \bar{\gamma}(\Omega) = g[r_t(\Omega)] - \gamma\,[r_o(\Omega)+H^N] - 2\pi G\rho_o H^o(\Omega) \qquad (9)$$

Where G is Newton's gravitational constant and ρ_o is the mean topographical density $\rho_o = 2.67$ g.cm^{-3}. The expression on the right side of Eq. 9 is the Simple Bouguer Anomaly. Therefore Eq. 8 can be written for geoid – quasigeoid separation term as,

$$H^N - H^o = \frac{\Delta g_B}{\bar{\gamma}(\Omega)} H(\Omega) \qquad (10a)$$

or

$$N_p - \zeta_p = \frac{\Delta g_B}{\bar{\gamma}(\Omega)} H(\Omega) \qquad (10b)$$

Eq. 10 is also called the C2 term as mentioned by Sjoberg, 1995, Rapp, 1997 and Featherstone and J.F. Kirby, 1998.

$$N(\varphi,\lambda) = \zeta_o(\varphi,\lambda,r_E) + C1(\varphi,\lambda) + C2(\varphi,\lambda) \qquad (11)$$

or

$$N(\varphi,\lambda) - \zeta_o(\varphi,\lambda,r_E) = C1(\varphi,\lambda) + C2(\varphi,\lambda) \qquad (12)$$

where

$$C1(\varphi,\lambda) = \frac{\partial\zeta}{\partial r}H + \frac{\partial\zeta}{\partial\gamma}\frac{\partial\gamma}{\partial h}H \qquad (13)$$

and

$$\mathbf{C2} = \frac{\Delta g_B}{\bar{\gamma}(\Omega)} H^o(\Omega) \qquad (14)$$

However, the Sjoberg (1995) paper includes a term dependent on H^2 as well as H in the N - ζ difference. For this analysis, only the 1st order term in terrain elevation (H^o) is considered.

Here Δg_B is the Bouguer gravity anomaly, $\bar{\gamma}(\Omega)$ is the average normal gravity between the reference and the telluroid. It is calculated between geoid and earth surface in routine work taking orthometric height as height term in its calculations.

3-Data Analysis and numerical comparison of the Results:

The data in both study areas comprise the absolute gravity along with orthometric heights. In addition to this Digital terrain model data (3 arc sec.≈ 90 m) from SRTM (USGS, EROS data center) was used to compare its results with orthometric heights to asses its applicability in the terrain correction determination for future geoid computation in Pakistan. The area boundaries and elevation statistics are shown in table 1. The Δg_B was computed using generalized formula [W.E. Featherstone and M.C. Dentith (1997), Eq-23] using point absolute gravity and elevation/DTM data. Theoretical normal gravity γ was computed using Somigliana's formula. For the computation of Δg_B, standard topographical density was assumed, i.e. 2.67 g.cm^{-3}. The Bouguer gravity anomalies and average theoretical gravity in conjunction with elevation data at the corresponding points were used in Eq. 14 to compute the C2 correction term. The results from absolute gravity and terrain/DTM data were compared with the geoid to quasigeoid correction term determined for the EGM96 global geopotential model [Lemoine et al. (1997), National Imagery and Mapping Agency]. The contour plots of C2 term from observed data is shown in figure 6 & 7. The statistics of the C2 term results are shown in table 2.

The Free Air gravity anomalies are correlated (90%) with elevation with inverse correlation (62%) of Bouguer anomalies in Kalat area (Fig-2). The correlation of Bouguer anomalies indicates the considerable Bouguer plate effect demanding the application of terrain correction in this area. This correlation is not significant (Fig-3) in Dadu, as both anomalies are negative and behave approximately similarly with elevation. This small difference of free air and Bouguer anomalies can be related to a small Bouguer plate effect (1.5 to 15.5 mgal only).

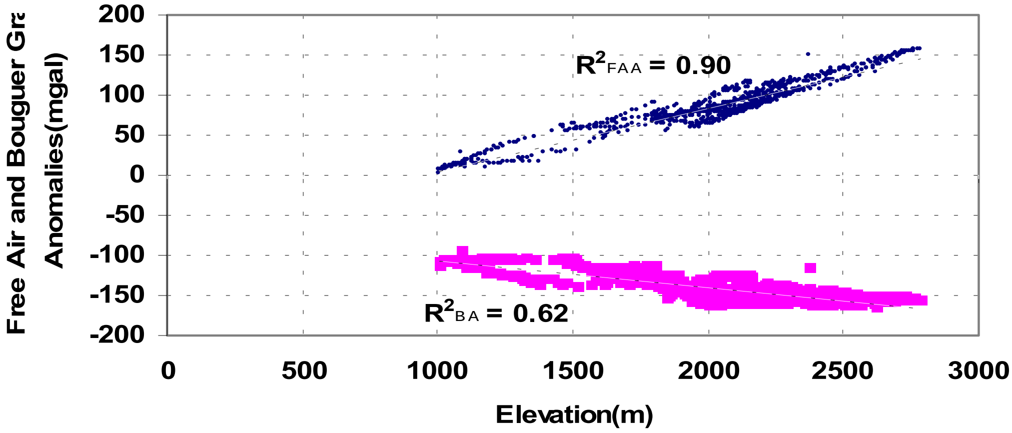

Fig-2. Relationship of Elevation with Free Air and Bouguer gravity Anomalies in Kalat Area

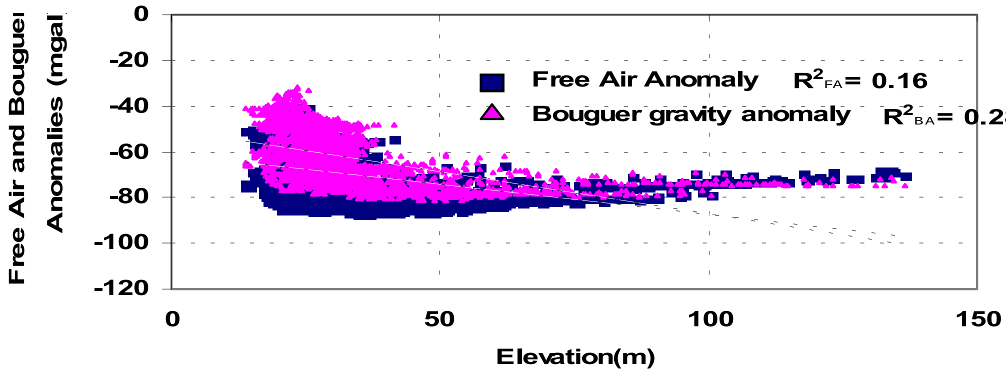

Fig-3. Relationship of Elevation with Free Air and Bouguer gravity Anomalies in Dadu Area

The comparison of geoid to quasigeoid separation terms from observed gravity data and gravity anomalies derived from the EGM96 global geopotential model in Kalat area shows close correlation with each other. The use of the digital terrain model in Kalat has created insignificant difference to the computed C2 term. Although DTM data differs much (of the order of 10-40 m), the effect on the resulting separation term is insignificant due to the reason that the coefficient of H in Eq-14 is of the order of 10^{-3}. The maximum magnitude of the C2 term determined from observed gravity data is 440 mm while that of the EGM96 gravity anomalies is 484mm. However, the standard deviation differs only by 14.3 mm. This term from gravity measurements in Dadu area comes out to be 12 mm while 19.6 mm from EGM96 gravity anomalies whereas, standard deviation differs by only 5mm. The results of DTM data confirm the observed data. This indicates similarity of the elevation data from DTM with leveling data. The difference of values from observed gravity data and EGM96 model may be related to the omission error within EGM96 model. This shows that the overall effect of omission error in Dadu is not significant, whereas it is considerable in Kalat.

The terrain correction was calculated using the software developed by Yecai Li, and Michael G. Sideris (1993) on the grids of orthometric heights to study its effect on this term. The terrain correction is not very large however considerable in Kalat and it has practically insignificant effect on this term in Dadu area. The standard deviation of geoid-quasigeoid separation differs by only 5.4 mm in the Kalat area and really no effect in Dadu area.

Measured Parameter(Kalat area)	Max	Min	Mean	Measured Parameter (Dadu Area)	Max	Min	Mean
Longitude(degrees)	67.093	66.496	66.776	**Longitude(degrees)**	67.78	67.35	67.566
Latitude(degrees)	29.426	28.57	29.005	**Latitude(degrees)**	27.29	26.53	26.909
Altitude above MSL(m)	2782.8	1006.2	2024.7	**Altitude above MSL(m)**	136.5	13.7	34.008
Altitude (from DTM)	2782	1021	2029	**Altitude (from DTM)**	148	32	51
Terr. Correction (mgal)	7.663	0.034	0.819	**Terr. Correction(mgal)**	0.155	0.0	0.005

Table-1:Statistics of altitude (in meters) of 927 land gravity points in Kalat(high land) area and 3495 points in Dadu (low land) area along with Terrain correction and latitudinal/longitudinal boundaries.

Description of Model(Kalat Area)	Max	Min	Mean	Std. Dev.	Description of Model(Dadu Area)	Max	Min	Mean	Std. Dev.
C (Obs. Gravity) Before Terrain Correction applied	-103	-440	-297	76.8	**C2(Abs. Gravity) Before Terrain Correction applied**	-0.7	-12	-2.67	1.6
C (Obs. Gravity) After Terrain Correction applied	-106.9	-427.4	-260	71.4	**C2(Obs. Gravity) After Terrain Correction applied**	-0.66	-10.1	-2.3	1.46
C2 (DTM)	-103	-437.4	-295.7	76.6	**C2 (DTM)**	-1.1	- 10	- 3.2	1.5
C2(EGM96)	-210	-484	-411.5	62.5	**C2(EGM96)**	18	-19.6	0.7	7

Table-2: Statistics of the geoid to quasigeoid correction term C2 (in mm) at 927 land gravity points in Kalat (high land) area and 3494 points in Dadu(low land) area from the Bouguer gravity anomaly and elevation with and without terrain correction applied. Also included are the C2 results from DTM and EGM96 global geopotential model gravity anomalies.

The separation term C2 is positive in low land area, though very small (quasigeoid is relatively higher than geoidal surface) and these surfaces reverse position with negative increase of C2 term as elevation increases. It is negative in low land (Dadu area) in general, and become more negative in high land (Kalat area). The correlation with elevation is more with observed data (94%) in Kalat area than EGM96 model (49.8 %) values (Fig-4). However, this correlation is reversed in low land (Dadu area) as C2 from observed data is less correlated (35.5 %) than EGM96 model (97%) separation term. This also indicates an important aspect of inherent data deficiency in EGM96 model in these areas. In low land area (Dadu) the EGM96 model with dominant low frequency components has close correlation with low elevation and gravity gradient. In high land area (Kalat), the EGM96 model values are ~50% less correlated than observed data indicating the deficient information regarding the high frequency component of gravity and elevation.

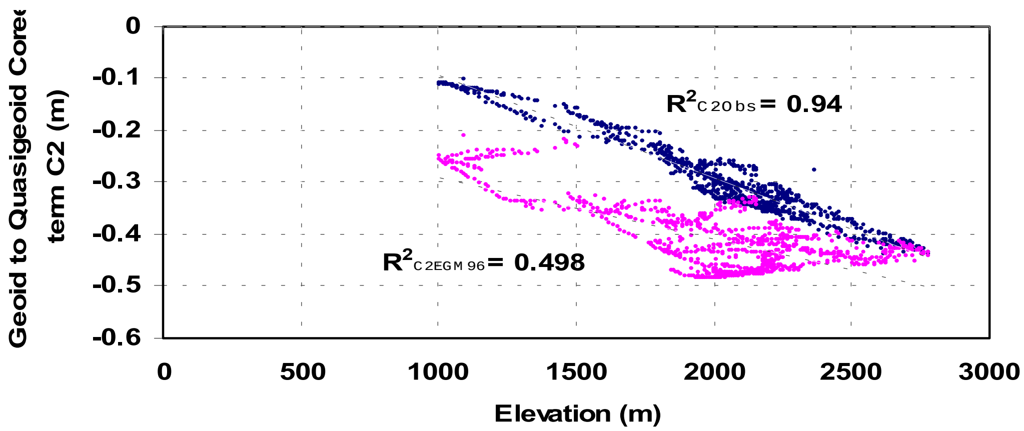

Fig-4. Relationship of Elevation with geoid-quasigeoid correction C2 term from observed gravity data and EGM96 model gravity in the Kalat area

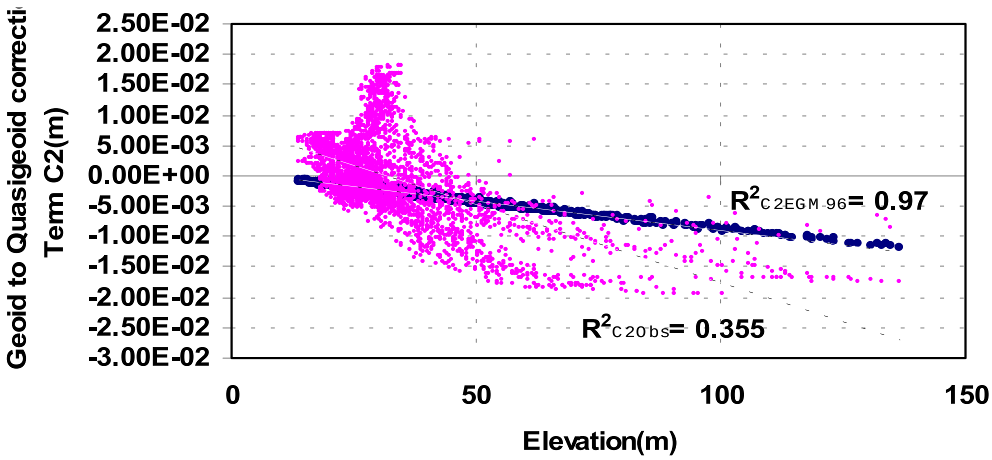

Fig-5. Relationship of Elevation with geoid-quasigeoid correction C2 term from observed gravity data and EGM96 model gravity in the Dadu area

The contour maps of the geoid to quasigeoid separation term from observed gravity data (Fig. 6 & 7 below) show an increase in absolute value in the north-west direction. The trend of the elevation is also increasing towards north-west direction. Most of the western half and complete eastern half of Dadu area is low elevation with 20-40 m above sea level, with the C2 term in the range of 2 -3 mm. The Kalat area has highest elevation in central west part with corresponding maximum separation term of 440 mm. This shows high correlation of C2 term with elevation. This also validates the data quality of observed gravity and elevation in both study areas.

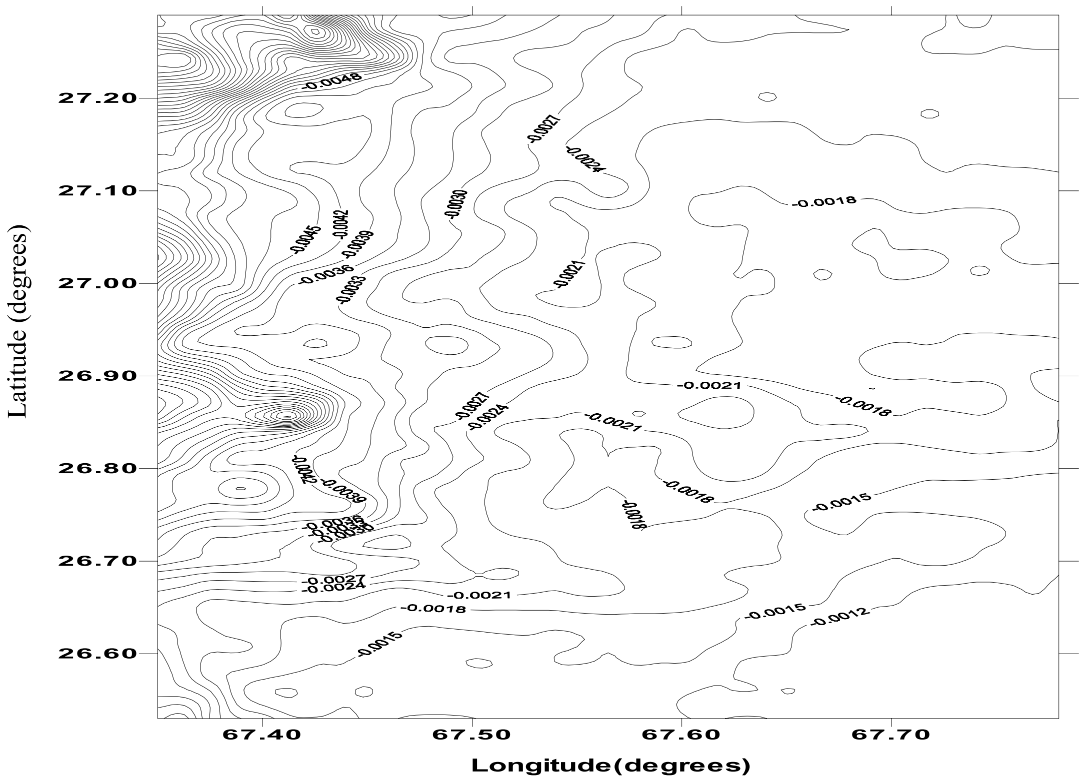

Fig-6. Geoid to Quasigeoid separation term C2 from observed gravity data in Dadu Area. Contour Interval=0.3mm

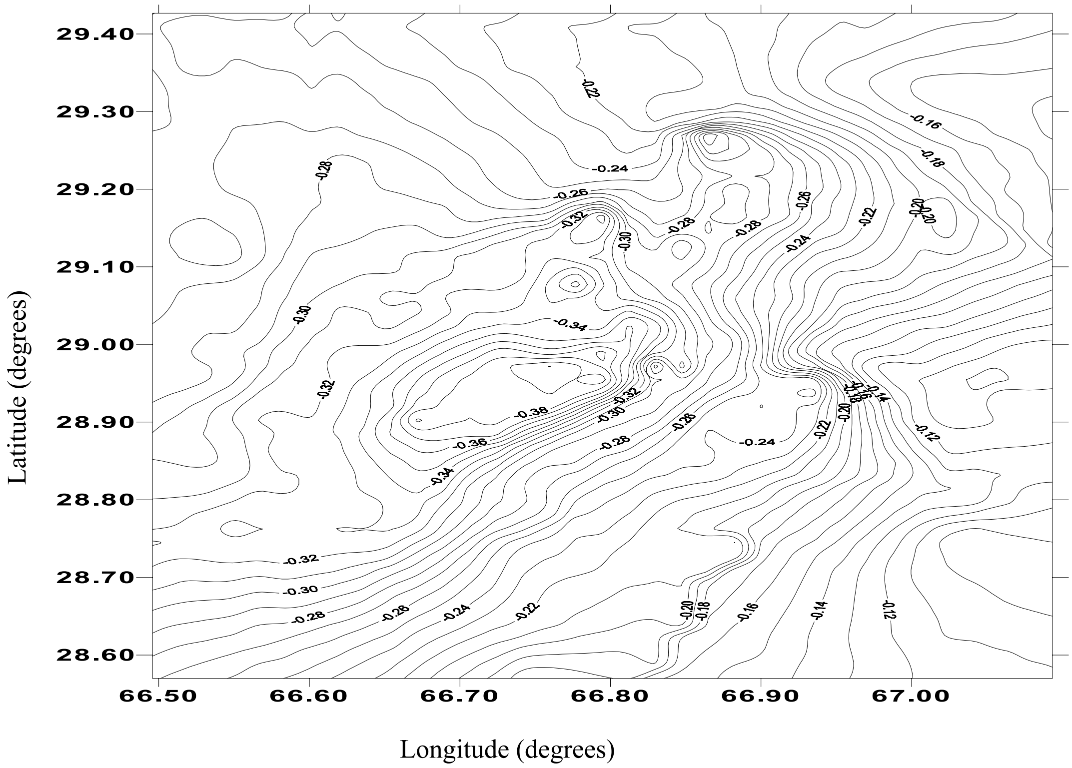

Fig-7. Geoid to Quasigeoid separation term C2 from observed gravity data in Kalat Area. Contour Interval=10 mm

4-Conclusions and Recommendations:

The geoid to quasigeoid separation term C2 was estimated in both study areas and a comparative study with elevation was established. There is a high correlation of the C2 term with elevation, though the correlation of Bouguer anomalies and free air anomalies in the low land area is comparable due to the very small Bouguer plate effect. The terrain correction effect in Kalat is considerable and it is practically insignificant in Dadu area. Keeping in view of the general terrain of Pakistan and the height datum of Pakistan, it is emphasized that the terrain correction be applied in the calculation of geoid to quasigeoid separation term. Also, the magnitude of the geoid to quasigeoid separation term C2 suggests its incorporation in the final geoidal solution, whichever course is followed in solving the geodetic boundary value problem of the gravity field. This also necessitates the estimation of C2 term over the whole area of Pakistan and its validation with other data sources e.g. GPS/Leveling data.

Acknowledgements:

Higher Education Commission of Pakistan is highly acknowledged for sponsoring this study under the indigenous Ph.D. program at the Department of Earth Sciences Quaid-i-Azam University (QAU) Islamabad, Pakistan. The Directorate General of Petroleum Concessions (DGPC), Ministry of Petroleum and Natural

Resources, Islamabad, Pakistan is also acknowledged for providing the gravity data of two study areas to the Department of Earth Sciences, QAU, Islamabad.

The authors are also very grateful to Professor Carl Christian Tscherning, University of Copenhagen, Denmark for the constructive remarks on the initial manuscript of this paper.

Reference:

Heiskanen, W. A. and Moritz, H. (1967) Physical Geodesy. Freeman, San Francisco.

Featherstone, W. E. and Dentith, M. C. (1994) Matters of gravity: the search for gold. GPS World 5(7), 34-39.

Featherstone, W. E. and Dentith, M. C. (1997), A geodetic approach to gravity data reduction for Geophysics. Computers & Geosciences Vol.23, No. 10, pp. 1063-1070.

Featherstone, W. E. and J.F. Kirby (1998), Estimates of the separation between the geoid and quasigeoid over Australia. Geomatics Research Australia, No. 68, pp.79-90.

H. Nahavandchi (2002), Two different methods of geoidal height determinations using a spherical harmonics representation of the geopotential, topographic corrections and height anomaly-geoidal height difference. Journal of Geodesy, No. 76, pp. 345-352

Lemoine, F. G., Smith, D. E., Smith, R., Kunz, L., Pavlis, N. K., Klosko, S. M., Chinn, D. S., Torrence, M. H., Williamson, R. G., Cox, C. M., Rachlin, K. E., Wang, Y. M., Pavlis, E. C., Kenyon, S. C., Salman, R., Trimmer, R., Rapp, R. H. and Nerem, R. S. (1997). The development of the NASA, GSFC and NIMA joint geopotential model, in Segawa, Fugimoto and Okubo (eds), IAG Synzposza 117: Gravzly, Geozd, and Marzne Geodesy, Springer-Verlag, Berlin, pp. 461-470.

Molodensky, M. S., Eremeev, V. F. and Yurkina M. I. (1962). Methods for the study of the external gravitational field and figure of the Earth. Israeli Program for Scientific Translations, Jerusalem.

National Imagery and Mapping Agency (1997). WGS 84 EGM96 (360,360) Public Web Page, http://164.214.2.59/geospatial/products/GandG/wgs-84/egm96.html

Rapp. R. H. (1997). Use of potential coefficient models for geoid undulation determinations using a spherical harmonic representation of the height anomaly/geoid undulation difference, Journal of Geodesy 71: 282-289.

Sjoberg, L. E. (1995). On the quasigeoid to geoid separation, manuscripta geodaetica 20: 182.-192.

USGS, EROS, DATA Center, SIOUX Fall, SD 57198-0001, http://srtm.usgs.gov/data/obtainingdata.htmal

Yecai Li and Michael G. Sideris (1993),Terrain Correction via 2 Dimensional Fast Fourier Transform with either mass-Prism or mass-Line topographic model. Deptt. of Geomatics Engineering. The University of Calgary, Canada.

Outlier detection in CHAMP kinematic orbit data to be used in gravity field determination

C. Gruber

Institute of Navigation and Satellite Geodesy, Graz University of Technology, gruber@geomatics.tu-graz.ac.at

March 1, 2005

Abstract

CHAMP orbit data have become available from dynamic, reduced dynamic and kinematic (purely geometric) approaches. All of them have been used in gravity field determination. However, the kinematic orbits enjoy higher acceptance since they do not employ any a-priori gravity field model. Unfortunately, kinematic orbits suffer from higher noise levels and outliers. Hence, improving kinematic orbits will directly influence the quality of the gravity field model. In this paper, a pre-processing strategy for kinematic orbit data will be presented. Based on orbit smoothing, outliers will be detected and excluded from further processing.

1 Introduction

The energy balance method is an established approach to determine the lower spherical harmonic coefficients (in the case of CHAMP up to degree/order ≈ 70) of the Earth gravity field (cf. *Badura et al.* 2004). Due to this approach the quality of the solution depends to a high degree on an accurate knowledge of the velocity of the spacecraft. If kinematic orbits shall be used, a strategy has to be developed to derive those velocities with sufficient accuracy. In the case of CHAMP, where a geoid solution at *dm* precision is envisaged, the velocity RMS must not be larger than $10^{-1} mm/s$ in order to meet this requirement. For the case of simulated orbits this can usually be achieved by standard numerical differentiation. Unfortunately, kinematic orbits suffer, compared to simulated or reduced dynamic orbits from a much higher noise level due to low confidence in the GPS configuration, i.e. poor satellite geometry or a low number of observations for a certain epoch (cf. *Švehla et al.* 2003). Althought the overall orbital data is of unpreceedented quality, still outliers have to be recognized in order to ensure the introduction of normally distributed kinetic energy as input for the balance equations.

The idea of how to detect outliers and to exclude them from further gravity field processing is the correlation of the data by a simple model. Filtering the orbital data with the spectral properties of the model could then be used to define a criterion for outliers.

2 The error model

We assume to estimate kinetic energy from orbit positions and their numerically derived velocities as,

$$T = \frac{1}{2}\left(\frac{G^2}{R^2} + \dot{r}^2\right) \tag{1}$$

with G being the angular momentum, R the radius from the satellite to the Earth center and $\dot{r}$ the radial velocity. The expression in brakets in eq. (1) can be assigned to $\dot{q}^2$, where $\dot{q}$ represents generalized momentum.

Understanding the force model as

$$U = -\int_{r_0}^{r} \boldsymbol{\mathcal{K}}(\boldsymbol{q})d\boldsymbol{q} \tag{2}$$

with q describing the shortest path from $\boldsymbol{r}_0$ to $\boldsymbol{r}$ in the Hamiltonian sense.

The total force $\mathcal{K}$ can be approximated as

$$\boldsymbol{\mathcal{K}} = \nabla V_{\oplus} + \nabla V_{\odot☾} + \boldsymbol{F}_s \tag{3}$$

with the conservative gradients of the Earth potential field, as well as of third bodies and the surface force $\boldsymbol{F}_s$, representing energy dissipation in the upper atmosphere. The surface force can be further analyzed by

$$\boldsymbol{F}_s = \boldsymbol{ac} + \boldsymbol{b} \tag{4}$$

leading to a linear correction of the (in the case of CHAMP) mismeasured dissipative accelerations $\boldsymbol{ac}$. The unknown bias $\boldsymbol{b}$ can be approximated if the derivatives of the along track, cross track and radial velocities are set equal to eq. (3) cf. *Gruber et al.* (2005), or after integration along the orbit by applying low degree polynomials (*Badura et al.* 2004).

After determination of the dissipative forces a representive energy constant over a certain time span can be found by

$$E = \frac{1}{n}\sum_{i=1}^{n}(T_i + U_i) \tag{5}$$

or by following $\|\mathcal{L}\|_1$ and using instead of the mean value the median.

From interchanging eq. (5), a general reference momementum $\dot{q}_r$ can be calculated

$$\dot{q}_r = \sqrt{2(E - U(q))} \tag{6}$$

Differences in position from the reference momentum and the change in position per epoch Δr of the satellite are obtained,

$$\delta r = \dot{q}_r \Delta t - \|\Delta \boldsymbol{r}\| \tag{7}$$

and can be treated by treshold values to define outliers.

3 Data preparation

The kinematic position data in the terrestial reference frame (ITRF) has been transformed into a non rotating frame and numerically differentiated. From analysis of the inclination of the orbital plane, gross outliers can be easily detected with standard methods, e.g. regression based technics (cf. M-estimation, *Huber* 1973) and the covariance information for these positions has been adjusted.

The gradient forces can be obtained from any a priori gravity field of the Earth as well as the solid Earth tides. The accelerometer data has been rotated into the orbital plane by the available attitude information as well as the orientation of the local orbital tripod in each point.

Fig. 1 shows the kinematic residuals from eq. (7) during a 12 hour time span (30 *sec* sampling), revealing a very good accordance between the kinematic orbit and the used model.

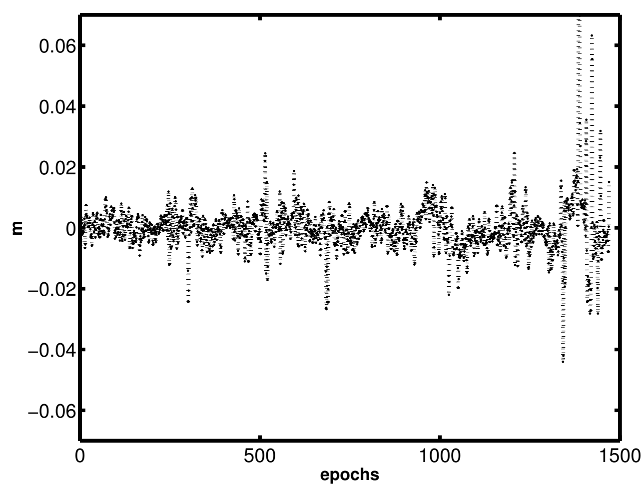

Figure 1: Kinematic position residuals between the used geopotential model and the measured data.

3

4 The Outlier detection

The kinematic residuals from eq. (7) will be split in the following by a suitable filter into a smooth dynamic innovation, $f(\delta r)$, with respect to the used geopotential coefficients of the reference field in eq. (2) and higher frequency components $g(\delta r)$, consisting of omitted geopotential spectrum, noise and outliers. Instead of filtering in spectral domain by impulse response filters, where hardly use of the available covariance information can be made, $f(\delta r)$ shall be approximated by a functional model with smooth characteristics in order to approximate the continuous properties of the osculating ellipses. The term continuous in this context underlines the fact that small changes within the geopotential field of the Earth will introduce only small changes to the orbital geometry of the spacecraft. Since the lower frequency part of the used reference field, e.g. EGM96 (*Lemoine et al.* 1998) is in good accordance to this by its parameterization with spherical harmonics (SH), the occurence of spikes in the data should be fully ascribed to outliers from the determination of the kinematic velocities.

A similiar approach can be found in SLR data processing, known as normal point generator (*Sinclair* 1997). The range observations are reduced by predicted satellite state vectors from force models and the differences are then approximated by smooth trend functions. The RMS of the residuals to the trendfunction will then be used as a rejection level for the observations.

4.1 Definition of a trend model

In our model the trend function is establised by harmonical base functions up to a finite spectral resolution and the corresponding amplitudes shall be determined by an optimized fit to the data. In order to make the functional model insensitive to outlier peaks, the available covariance information will be used as an a priori observation dispersion as well as a robust estimation approach (cf. *Koch/ Levenhagen* 2002) that shall fit the trend function. Thus a spectrally limited harmonic analysis of the kinematic residuals shall best approximate low frequencies as the innovative signal, and gain outliers as their signal counterparts beyond a to be defined treshold.

4.2 Estimation of the model parameters

The functional model can then be described by a Fourier series, but the coefficients shall be determined by an estimation procedure in order to incorporate covariance information.

$$\begin{aligned} f(\delta r) \Leftrightarrow \mathcal{F}(\omega) &= a \cdot \cos(2\pi n\tau) + ib \cdot \sin(2\pi n\tau) \\ (a + i \cdot b) &= (A'Q^{-1}A)^{-1}A'Q^{-1}f(\delta r) \end{aligned} \tag{8}$$

The linear parameter estimation, minimizing the norm of the residuals shows deficiencies when outliers are in the data. We therefore applied an iterative approach where assumed outliers are iteratively downweighted during the estimation process.

4.3 Definition of the spectral resolution of the trend model

In oder to supplement the low geopotential frequencies used in eq. (2) as well as to account for unmodelled effects such as ocean tides, it has to be defined what spectral resolution of the trend function should be envisaged.

From analysis of Fig. 1 it can be seen that in order to remove a suitable trend function a development up to a few principal frequencies would be sufficient. The corresponding frequency of the flattening term of the Earth (J_2) transforms within a 12 *hours* time span, i.e. rougly 8 revolutions, to 16 harmonic cycles or an upper frequency of roughly $(46 \cdot 60)^{-1}$ Hz if the revolution duration is $\approx 92min$. If the trend function is limited to that degree, only a possible mismodeling of this particular geopotential frequency is being taken care of by the trend function.

If we regard the used gravity field model as a rough approximation only, then the trend function should be able to absorb deficiencies in all employed geopotential frequencies in order to maintain independence from the model. On the other hand it is clear that during a given timespan only a limited number of geopotential frequencies (e.g. mainly zonal terms) should truly affect the satellites position. We therefore assume the isotropic commission error from error degree variances (RMS) of the SH - spectrum as representative measure to analyse the effect on the orbit positions. According to Kaula's rule of thumb (*Kaula* 1966),

$$\sigma_l = \sqrt{\sum_{m=0}^{l} \bar{C}_{lm}^2 + \bar{S}_{lm}^2} = \sqrt{2l+1} \;\; \frac{10^{-5}}{l^2} \tag{9}$$

approximates the spectral density (PSD) of the fully normalized geopotential coefficients (C, S) and together with the transfer function

$$\lambda_l = \frac{GM}{R} \left(\frac{a_\oplus}{R} \right)^l \tag{10}$$

we obtain error degree variances for the gravity potential at satellite height,

$$\sigma_{U_l} = \sqrt{\lambda_l^2 \sigma_l^2}, \tag{11}$$

with GM the gravity constant of the Earth, $a_\oplus$ mean Earth radius, l geopotential degree, R geocentric radius of the satellite.

The equivalent error model according to *Rapp* (1978) reads,

$$\sigma_l(\Delta g) = \sqrt{\alpha_1 \frac{l-1}{l+1} s_1^{l+2} + \alpha_2 \frac{l-1}{(l-2)(l+2)} s_2^{l+2}} \tag{12}$$

5

where $\alpha_1 = 3.404, \alpha_2 = 140.03, s_1 = 0.998006, s_2 = 0.914232$

and the corresponding transfer function

$$\lambda_l = \left(\frac{ae}{R}\right)^l \frac{R}{l-1}. \tag{13}$$

Error propagation of σ_{U_l} into eq. (7) yields the reference position error per degree

$$\sigma_{l,\delta r} = \frac{\Delta t}{\sqrt{2(E-U(q))}} \cdot \sigma_{U_l} \tag{14}$$

due to the used geopotential model. Fig. 2 shows the position error per degree, comparing the two different error degree variance models, namely Kaula and Rapp,

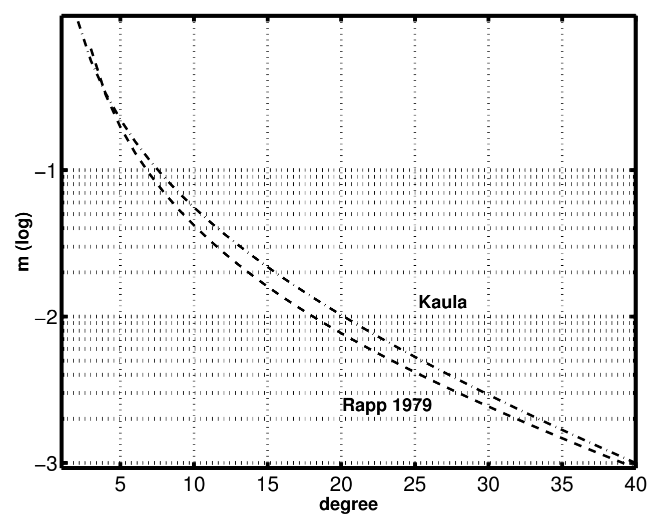

Figure 2: position error per degree according to error degree variances of the SH expansion from different empirical models.

It is understood, that in order to approach a *cm*- level for the filtering of the kinematic position residuals the spectral range of the trend function should be in the case of Kaula's rule equivalent to geopotential frequencies up to DEG/ORD 20. On the other hand, the higher the resolution of the trend function becomes, the more difficult it gets to robustly estimate the corresponding parameters. A proposed rigorous treatment would be the statistical assessment of the applied model, i.e. testing for significance of the model parameters for each estimation. The outliers could then be statistically detected by data snooping. For details cf. (*Kern*, 2005). In our approach we must admit a lot better quality to the reference field than the error PSD of the coefficients indicate and therefore limit the resolution of the trend function to an equivalent geopotential degree of $l_{\max} = 6$. This can be understood in the following manner: the innovative difference between the used reference model and the solution belonging to the kinematic orbit data shall be found far below the degree variance models of Kaula and Rapp. This is certainly a critical aspect and we might therefore loose independend gravity field information within the spectral bandwith (BW) of the used reference geopotential model beyond ($l > 6$) that would possibly be detected as outliers. Nevertheless, it turns out after geopotential recovery of the filtered kinematic orbit (cf. section 5), the named spectral BW comes out different from the used reference model, inspite of being the weakest part in terms of infiltration of a- priori information. The system proofes to be still capable in recovering an independend solution. Fig. 3 shows the trend function, approximating the kinematic position residuals.

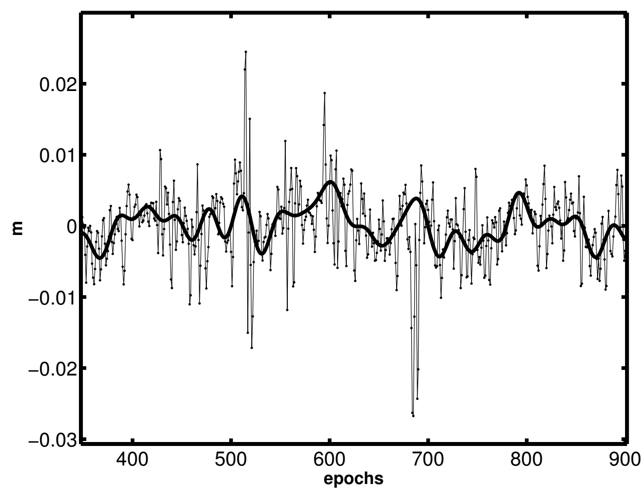

Figure 3: Fit of the trend function with a spatial resolution up to 15 epochs (DEG/ORD 6).

4.4 Definition of a treshold for outliers

Once the trend model has been fitted, the innovative part can be subtracted from δr, yielding the noise and outlier function $g(\delta r)$. To distinguish outliers from remaining gravity field signal a treshold value has to be defined, taking into account the remaining signal power that can be expected from the omission error of the geopotential development of the reference field,

$$\Delta\delta r = \frac{\Delta t}{\sqrt{2(E - U(q))}} \cdot \Delta U \tag{15}$$

7

where ΔU has been calculated by

$$\Delta U = \int_{r_0}^{r} \nabla V_{l,\infty} d\boldsymbol{q} \tag{16}$$

from EGM96 but could be simultaneously obtained again from e.g. Kaula's rule of thumb. Fig. 4 shows the omission error according to eq. (15) from a signal beyond DEG/ORD $l > 40$ in terms of orbit deviations.

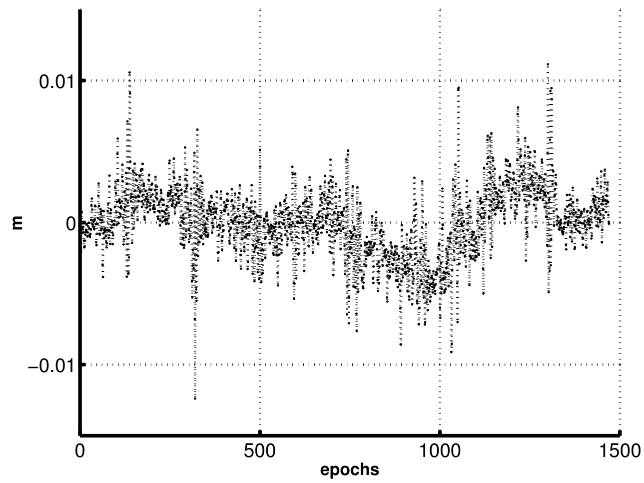

Figure 4: Range of the omission error in terms of orbit deviations

It is evident that the omission of geopotential signal beyond DEG/ORD 40 represents a clear limitation for an outlier treshold. Reduction of the omission error by a newly trend reveals remaining deviations of less than 1 *cm*. The treshold value has therefore been set to 1.25 *cm*.

Fig. 5 shows the total situation after removal of the trend function. No assumeable geopotential information should be found beyond the treshold values.

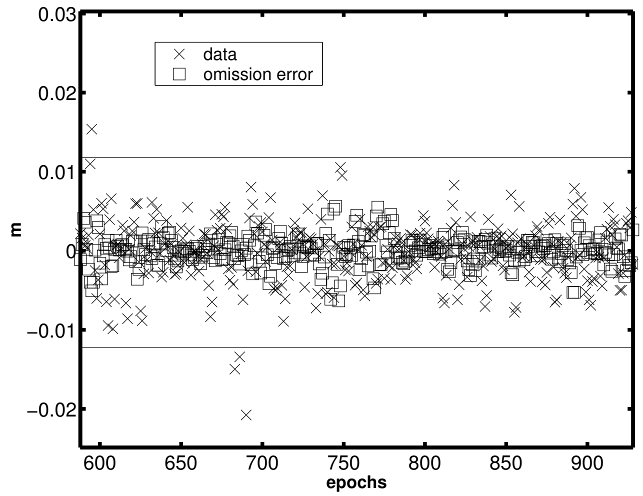

Figure 5: Kinematic residuals after trend removal and omission error within a treshold.

5 Model test

After the filtering with EGM96, modified error variances for the kinetic energy have been introduced into a LS estimation of the full geopotential coefficients from DEG/ORD 2 to 50, applying the energy balance equation (cf. *Jekeli* 1999). Fig. 6 shows the difference PSD's with respect to other gravity field models.

9

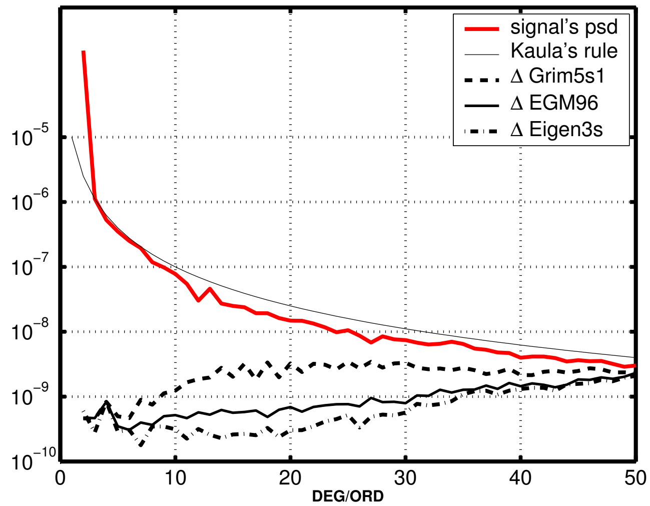

Figure 6: Comparison of a filtered solution by EGM96 to existing geopotential models: GRIM5S1, EGM96, EIGEN3.

It can be seen that the solution fits best to EIGEN3S, although not being used for the outlier detection. A similiar result is obtained if EIGEN3S shall be used for the filtering. If GRIM5S1 has been used, a slight deterioration of the result can be observed (not plotted) which is in accordance to the general deficiency of the approach in the BW above $l > 6$, as being stated earlier. In order to obtain acceptable results a good reference solution is thus necessary.

6 Conclusions and Outlook

The method presented in this paper is an alternative approach, compared to the use of dynamic orbits, in order to detect outliers, by their kinematic correlation to external gravity field information.

In an ideal case, the a-priori covariance information would represent the configuration of the observation space. Projection onto the parameter space would then give an immediate result for the geopotential model. Unfortunately this is not the case and the available covariances give therefore a too optimistic picture concerning the outliers.

Once a global gravity field solution has been processed, the a-posteriori covariances for the velocities (and thus the positions) can be computed and their differentiation being repeated. A question under investigation is, whether an iterative approach without use of any a-priori information will converge. An evaluation strategy could moreover be defined, assessing the quality of the approach and the error probability of successfully detection (or failure) of outliers.

10

7 Acknowledgement

The Author would like to thank the Geoforschungszentrum Potsdam (GFZ) for providing the accelerometry data as well as Drs. Dražen Švehla and Markus Rothacher who made available the kinematic orbit data. Valuable discussions and input from Dr. Michael Kern has been gratefully appreciated.

The Authors Adress:
Christian Gruber
Graz University of Technology
Institute for Navigation and Satellite Geodesy
Steyrergasse 30/III, A-8010 Graz, Austria
phone +43(0)316 873-6357
fax +43(0)316 873-6845
email chrs.gruber@gmx.net

References

Badura T., Gruber C., Klostius R., Sakulin C. CHAMP *gravity field processing applying the Energy Integral Approach* Joint CHAMP/GRACE Science Meeting,GFZ, July 6-8, 2004, IN: Arne K. Richter (ed.) Advances in Geosciences 2004.

Gerlach C. et al., *A* CHAMP-*only gravity field model from kinematic orbits using the energy integral,* Geophysical Research Letters, VOL. 30, NO. 20, 2037, doi:10.1029/2003GL018025, 2003.

Gruber C., Tsoulis D., Sneeuw N., CHAMP *Accelerometer calibration by means of the equation of motion and an a-priori gravity field.* Zeitschrift für Vermessungswesen, ZfV, in print, 2005.

Huber P.J. *Robust regression: Asymptotics, conjectures and Monte Carlo*, Ann. Stat., **1**, 799-821, 1973.

Jekeli C., *The determination of gravitational potential differences from satellite-to-satellite tracking,* Cel. Mech. Dyn. Astron., 75, 85-101, 1999.

Kaula W.M. *Thoery of Satellite Geodesy, Applications of Satellites to Geodesy.* Dover Publications, Inc. Mineola, New York (edition 2000).

Kern M., *External Calibration and Validation Methods for the Satellite Mission* GOCE*,* Final technical report in the frame of External ESA Fellowship at Graz University of Technology 2005.

Rapp RH.: *Potential Coefficient and Anomaly Degree Variance Modelling Revisited.* Tech. Rep. No. 293, The Ohio State University, Department of Geodetic Science, Columbus, Ohio 1979.

Reigber Ch., Lühr H., Schwintzer P.: *First Champ Mission Results,* Springer Verlag, Berlin Heidelberg 2003

Sinclair A.T.: *Data Screening and Normal Point Formation.* Royal Greenwich Observatory, Cambridge, UK 1997.

Švehla D, Rothacher M, *Kinematic and Reduced-Dynamic Precise Orbit Determination of* CHAMP *satellite over one year using zero-differences.* EGS-AGU-EUG Joint Assembly 06-11 April 2003, Nice, France. Geophysical Research Abstracts, European Geophysical Society Vol. 5. ISSN:1029-7006

Latest Geoid Determinations for the Republic of Croatia

T. Bašić*, Ž. Hećimović**

* Faculty of Geodesy, University of Zagreb, HR-10000 Zagreb, Kačićeva 26, Croatia
** Av. M. Držića 76, 10000 Zagreb, Croatia

Abstract. *Due to several improvements that have been done in comparison to the previous solution, like the usage of better terrestrial gravity data at the Adriatic Sea, much more GPS/leveling points available, wider topography integration area and better residual terrain modeling procedure, one-block collocation for entire area, and finally, four times denser computation grid, have resulted in the official geoid solution for Croatia HRG2000. This solution is based on the long wavelength gravity field structures from EGM96 global geopotential model.*

Recent CHAMP and GRACE satellite missions are defining new standards in modeling of the Earth's gravity field, improving global gravity field models especially in long- and medium-wave range. This was confirmed for the Croatian territory thanks to the undertaken comparison of several such models with GPS/leveling and HRG2000 geoid data.

Based on these facts and the availability of a new and much denser point gravity data set over the land area, newest geoid computation for the Republic of Croatia become possible. This paper offers a detailed description of the applied computation procedure, the geoid quality estimation using GPS/leveling points, and the presentation of specially developed computer program made for the purpose of geoid interpolation in any area of the state.

Keywords. *Geoid, gravity, GPS/leveling, terrain modeling, satellite missions, HRG2000 geoid solution*

1 Introduction

First serious attempts in determination of geoid surface in this region are connected with the establishment of independence of the Republic of Croatia. Nevertheless, a significant improvement was realized in 1998, when the first HRG98 solution was presented at the EGS 23rd General Assembly in Nice (Bašić et al. (1999)), and immediately after that HRG98A modified solution at the 2nd Joint Gravity and Geoid Meeting in Trieste (Bašić and Brkić (1999)).

During the year 2000 next step forward was made in the Department for Geomatics at the Faculty of Geodesy University of Zagreb, resulting with the most recent geoid solution HRG2000, see Bašić (2001). Since HRG2000 was proclaimed by the State Geodetic Administration as the official geoid surface of the Republic of Croatia, in the continuation the short presentation of this solution and the special computer program for interpolation purpose is given, followed by an overview of the latest efforts in the preparation for the calculation of the new solution HRG2005.

2 Computation of HRG2000 geoid

2.1 Previous investigations

In the frame of preparatory work (Hećimović (2001)), the numerical investigation with 14 global Earth Geopotential Models (EGM) was undertaken with the goal to find the model that best fits the Earth gravity field on the territory of Croatia. As reference values, GPS/leveling geoid undulations on 121 points were used. It was found out that global geopotential models EGM96 and GFZ97 fit best the Earth gravity field on our territory (see Table 1). In order to determine the existence of constant vertical shift between the Croatian vertical datum and EGM96 and GFZ97, two transformation models were defined. The transformation model which includes zero-undulation N_o fits better the real data and improves the existence of constant vertical displacement between GPS/leveling undulations and EGM96 and GFZ97 geoid of –1.37 m and -1.28 m respectively, for more details see Hećimović and Bašić (2003).

Another interesting investigation was the examination of the influence of the resolution change in reference Digital Terrain Model (DTM) on the calculation of short-wavelength effects (Residual Terrain Modeling - RTM) in gravity anomalies (Hećimović (2001), which showed that the use of 20′x30′ reference DTM yielded residual gravity anomalies with the best statistical properties to apply in the collocation (small and smooth residual gravity field).

Table 1. The statistics of differences between GPS/leveling and different EGM geoid undulations (in m).

Model	Min	Max	Mean	St.
EGM96	-2.43	0.21	-1.33	0.44
GFZ97	-2.44	0.22	-1.21	0.47
OSU91A	-4.43	2.07	-0.62	1.16
IFE88E2	-3.42	1.41	-0.55	0.93
GFZ93A	-2.97	1.74	-0.62	0.85
GFZ93B	-3.08	1.67	-0.69	0.85
GPM2	-4.45	2.08	-0.80	1.47
GRIM4	-3.37	2.28	-0.53	1.14
GEM-T3	-4.21	0.76	-1.65	1.11
JGM-1S	-3.85	1.07	-1.99	1.00

2.2 Calculation method

The strategy for high-resolution local gravity field determination is using three parts of the gravity field information: the long-wavelength part is taken from the global geopotential model, the medium-wavelength part originates in terrestrial point gravity field observations like free-air gravity anomalies and GPS/leveling data, and the short-wavelength part is taken from the high-resolution digital terrain model. In the simple remove-restore technique, the reduced observations are thus written as linear functional of the anomalous gravity potential T (Bašić (1989)):

$$x_i = \mathrm{L_i}(T) - \mathrm{L_i}(T_{EGM}) - \mathrm{L_i}(T_{RTM}) + n_i \,. \tag{1}$$

The least squares collocation determines the approximation:

$$\tilde{T}'(P) = \mathbf{C}_P^T \ (\mathbf{C} + \mathbf{D})^{-1}\, \mathbf{x} \,. \tag{2}$$

Here P is a point in space, matrix **C** contains the signal co-variances between the observations, $\mathbf{C}_P$ contains the signal co-variances between the observations and predicted $\tilde{T}'$ value in the point P, and **D** is the variance-covariance noise matrix.

The least square collocation technique results in predictions $\mathrm{L_j}(\tilde{T})$. To obtain the desired results, the effect of the anomalous masses and the effect of the geopotential model need to be added back through the restore procedure:

$$L_j(\tilde{T}) = \mathrm{L_j}(\tilde{T}') + \mathrm{L_j}(T_{EGM}) + \mathrm{L_j}(T_{RTM}) \,. \tag{3}$$

We decided to use collocation technique because the territory of Croatia is a relatively small area, so the huge and extensive numerical operations were possible to be done in one-step due also to their flexibility in handling heterogeneous irregular spaced data. In addition, we preferred to have the error estimates of predicted quantities (Bašić (1989)).

2.3 Data sets used

Since the global geopotential models EGM96 fit best the Earth gravity field on our territory (Table 1), it is used for definition of long-wavelength structures. This model consists of spherical harmonic coefficients complete to degree and order 360 (Lemoine et al. (1996)).

In performing the residual terrain modeling, three grids were put to use: the detailed model of topography 4"x5" (approx. 120x110 m), covering an area from 41° to 48° in latitude, and 12° to 21° in longitude, the coarse 5′x5′ grid of relief heights covering an bigger area from 32° to 57° and from 0° to 33° in latitude and longitude respectively, and 20′x30′ RTM reference grid of the same area as the coarse one. For the topographic masses the constant density of 2670 kgm^{-3} is assumed. These digital terrain models were applied in well-known Forsberg's TC software (Forsberg (1984)) for computation of terrain effects on gravimetric quantities.

For the calculation of free-air gravity anomalies point gravity data has been applied over the continental part of Croatia, Slovenia and Bosnia and Herzegovina, as well as Hungary and Italy (but rare). The gravity anomalies over the Adriatic Sea have been derived in 5′x5′ grid from map 1:750 000 (Morelli et al. (1969)), while the data covering Serbia and Montenegro have been recalculated in 5′x5′ grid from Bouguer anomaly maps 1:200 000. In this way a gravity data bank with more than 7500 free-air anomalies was created (Bašić (2001)).

In Table 2 the main statistics of gravity anomalies is presented, where the effects of the applied remove procedure decreasing the standard deviation from 34.53 mgal for observed anomalies to 12.40 mgal for residuals (Δg_{OBS}-Δg_{EGM96}-Δg_{RTM}) is evident. A significant reduction of the mean value from 8.70 mgal to 0.47 mgal (good centered data) can be recognized too (1 mgal = 10^{-5} ms^{-2}).

Table 2. Statistics of gravity anomalies and their residuals (in $10^{-5}ms^{-2}$)

	Δg_{OBS}	Δg_{EGM}	Δg_{RTM}	Δg_{RES}
Mean	8.70	14.27	-6.04	0.47
St.Dev.	34.53	29.15	20.21	12.40
Min	-103.07	-95.59	-119.35	-47.04
Max	180.14	109.33	106.80	64.31

A priori information about the variation of the local gravity field is introduced through the empirical covariance function calculated using residual gravity anomalies. In our case the variance of the empirical covariance function has the value of 154.09 $mgal^2$ and the first zero-value occurs already at the distance of 50 km (Bašić (2001)).

For the purpose of correct absolute orientation of the calculated geoid surface, a limited number (138) of GPS/leveling points distributed across the Croatia has been used. The statistics are presented in Table 3, where an apparent remove effect is present again, but it should be noted that the value of the mean N_{RES} = -2.16 m, most likely originates from the discrepancy between the used EGM96 model and the definition of national vertical datum, which is related to the tide gauge in Trieste.

Table 3. The statistical characteristics of geoid reduction effect in 138 GPS/leveling points (in m)

	$N_{GPS/l}$	N_{EGM9}	N_{RTM}	N_{RES}
Mean	44.41	45.78	0.81	-2.16
St.Dev.	1.22	1.07	0.23	0.33
Min	39.65	40.35	0.61	-3.18
Max	46.88	47.63	1.67	-1.50

2.4 Geoid prediction

The actual computation area has been chosen to cover the entire territory of Croatia: from 42.0° to 46.6° in latitude, and 13.0° to 19.5° in longitude, with calculation grid of 1′x1.5′ (approx. 1.8x2.0 km) or total 72 297 prediction points. As a final product selected HRG2000 with 36 184 points was defined covering strictly the Croatian territory (Fig. 1). Table 4 gives the main statistics for the selected HRG2000 geoid, their error estimates and belonging height information. For the predominant part of selected area the geoid undulations have the standard deviations of 1-2 cm and only in the Central Adriatic Sea they are up to 10 cm (Bašić (2001)).

The comparison of HRG2000 with former HRG98 solution (Bašić et al. (1999) shows significant differences resulting from the application of more reliable gravity anomalies over the Adriatic Sea, considerably more GPS/leveling points (138), better residual terrain modeling (20′x30′ reference DTM and farther integration up to 2000 km), as well as successful realization of one step collocation.

Furthermore, calculation grid in HRG2000 solution is four times denser. Although we met dramatically huger demands in numerical processing of topography data as well as in collocation, everything was successfully done on an average personal computer.

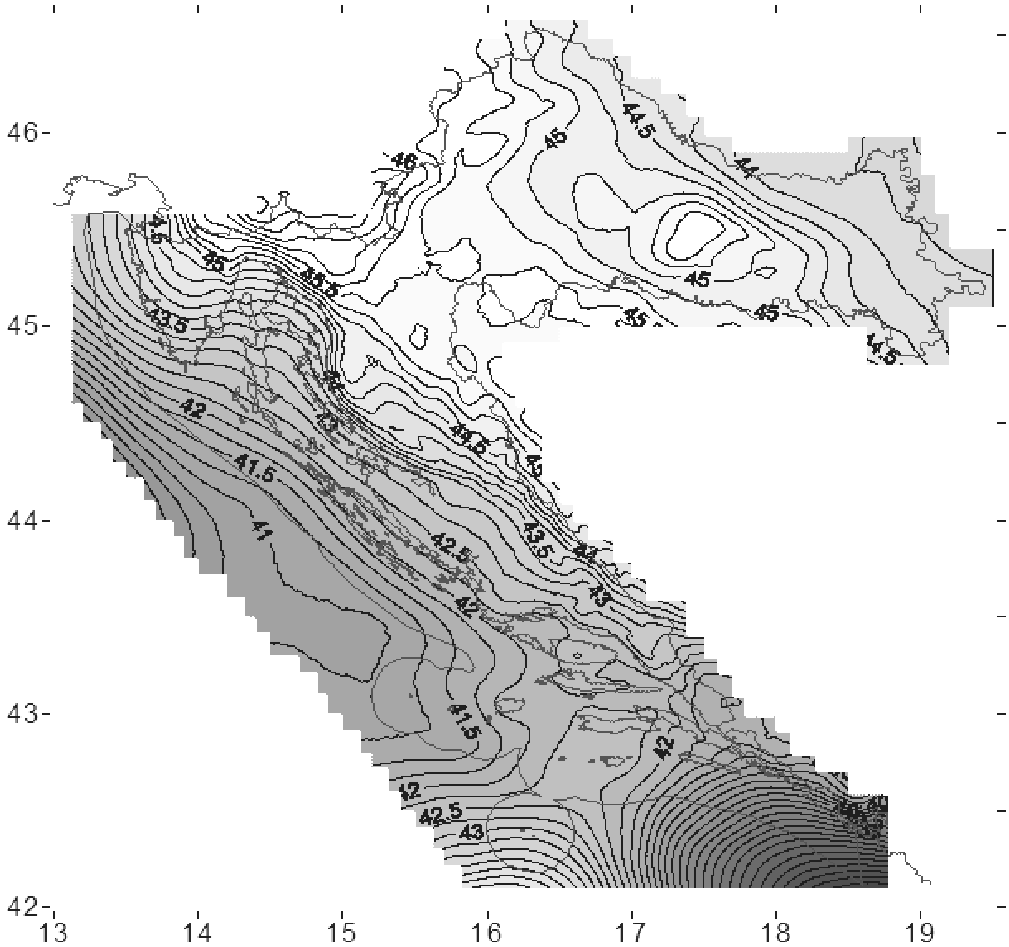

Fig. 1 Selected HRG2000 geoid surface (m).

Table 4. Statistics for selected HRG2000 geoid undulations, their standard deviations and corresponding heights (36184 data, in m)

	N	St. Dev.	$H_{HRG2000}$
Mean	43.2	0.02	118.9
St.Dev.	1.9	0.02	347.9
Min	36.3	0.01	-1169.0
Max	47.0	0.11	1781.0

3 Computer program for interpolation

Resulting from an increasing number of GPS-technology users in Croatia, a special scientific and professional project has been made by the State Geodetic Administration and the Department for Geomatics at the Faculty of Geodesy that resulted with the computer program: IHRG2000. The program is written in Microsoft Visual Basic 6.0 and supports all the latest Windows platforms. The basic purpose of the program is the interpolation of HRG2000 geoid (Fig. 1) and the presentation of the results on screen, their storage on a disc and a print out. In the IHRG2000 program there are two possibilities of interpolation: bilinear and spline (Bašić and Šljivarić (2003)).

After initiating the program IHRG2000, the *initial form* in Croatian language is shown on the screen (Fig. 2). The program is ready for data input and for the changes in computation parameters. The most important input values are latitude and longitude in DEG (degrees and decimal degree parts) or DMS (degree, minutes and seconds) units. They are entered in three ways: by keyboard, disc, and from a map.

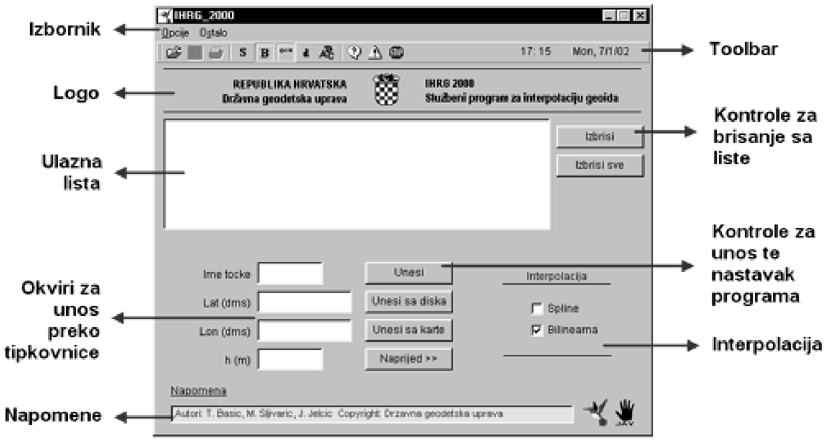

Fig. 2 Initial form of IHRG2000 program

The utility programs IHRG2000, created in the Department for Geomatics, to be used by the State Geodetic Administration of the Republic of Croatia should find their application in the practice, especially because the application of modern geodetic technologies requires that. Without knowing the accurate geoid surface it is impossible to make the connection between ellipsoid heights that are today very accurately provided by GPS technology, and orthometric heights that are used in practice. The licensing system of the program by the State Geodetic Administration provides the uniqueness and official character for this computer program, as well as for the data processed and realized using this program.

4 Preparations for the calculation of the new geoid

In 2004 the work was continued on finding even better solution for the geoid surface in Croatia. Within the frame of these efforts, the analysis of CHAMP and GRACE geoid solutions on our territory was made (Hećimović and Bašić (2004a)), the new digital terrain model Shuttle Radar Topography Mission (SRTM) was used for computing topographic effects of the Earth gravity field and compared with the so far used DTM (details in Hećimović and Bašić (2004b)), and the most important of all, the situation in gathering and quality control of the new gravity data has been significantly improved in this area.

4.1 CHAMP and GRACE geoid models

Recent CHAMP and GRACE satellite missions define new standards in modeling gravity field of the Earth. Gravity signals that were out of sensitivity band of previous measurement techniques are becoming clearly recognized. CHAMP and GRACE are improving global gravity field models especially in long-wave and middle-wave range.

To estimate how well CHAMP and GRACE geopotential models fit gravity field in Croatia, the comparison of seven CHAMP and three GRACE models with GPS/leveling undulations (121 points) and HRG2000 geoid in 1'x1' raster has been made. GRACE models show better fitting of gravity field than CHAMP models (see Tables 5 and 6). The differences from gravity field with CHAMP models are strongly correlated with topography. The differences of GRACE gravity models are containing higher amount of short-wave topography gravity signal than CHAMP models, but the discrepancies from a more precise topography structure can be recognized. GRACE model GGM01C is the best fitting gravity field (Fig. 3 and Table 6), details in Hećimović and Bašić (2004a).

Table 5. The main statistical characteristics of differences between GPS/leveling and recent global geoid models (121 points; in m)

Model	Min	Max	Mean	St. Dev.
EIGEN-2	-4.70	2.30	-1.34	1.35
EIGEN-3p	-3.40	1.89	-1.07	1.04
TUM-1S	-3.74	1.57	-1.26	1.15
TUM-2Sp	-4.16	1.98	-0.62	1.29
ITG-CHAMP01E	-3.50	1.88	-0.91	1.07
ITG-CHAMP01S	-4.11	1.72	-0.89	1.13
ITG-CHAMP01K	-4.13	1.69	-0.88	1.16
GRACE01S	-2.51	1.13	-1.08	0.80
GGM01S	-2.59	1.33	-1.06	0.82
GGM01C	-2.02	0.17	-1.00	0.45

Obtained wavelengths of differences are in short wave ranges depending on the terrain behavior. In the higher mountain area the differences are bigger than in the flat area. As the new CHAMP and GRACE global geopotential models represent much better the long and medium wave gravity field structures at the Croatian territory than the older models, they could certainly be used for the computation of the new geoid solutions in the future.

Table 6. The main statistical characteristics of differences between global geoid models and HRG2000 (53135 grid points; in m)

	Min	Max	Mean	St. Dev.
EIGEN2 - HRG2000	-0.51	5.74	2.54	1.61
GRACE01S - HRG2000	-0.99	3.38	1.23	0.78
GGM01S - HRG2000	-1.20	3.72	1.18	0.83
GGM01C - HRG2000	-0.29	2.50	1.20	0.46

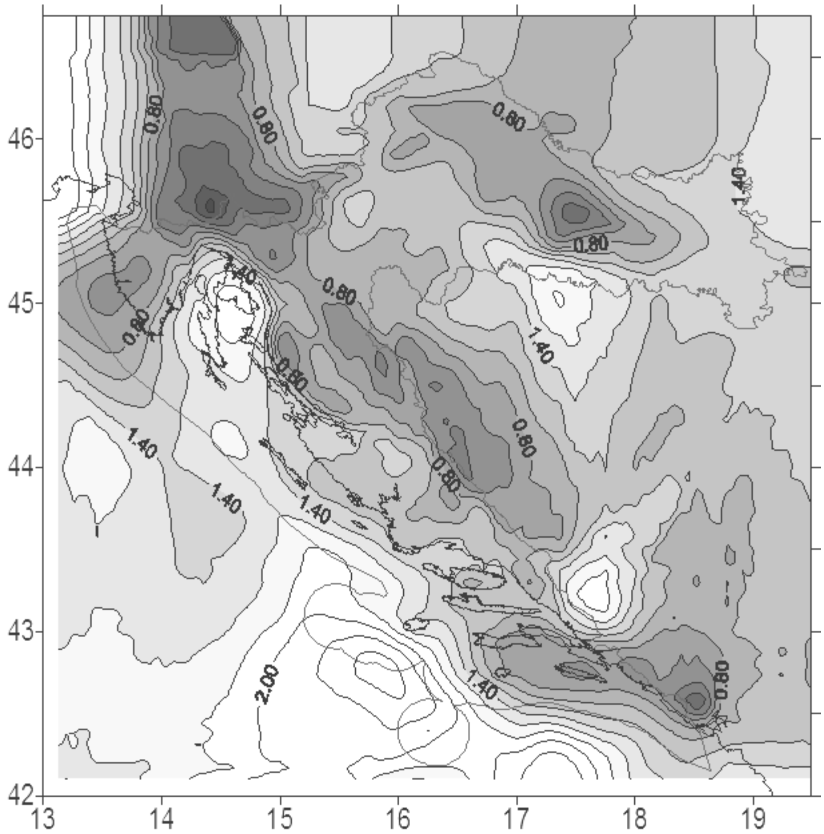

Fig. 3 Differences between GGM01C and HRG2000 geoid solutions (m)

4.2 New Gravity Data Base

In the meantime, a new gravity data base with over 46700 items has been successfully established, out of which over 41000 point gravity values cover the land part of former Yugoslavia (see Fig. 4).

We deal here with essentially larger number of available gravity data than it has been the case so far (more than 10 times). Using the method of prediction by least squares, the quality of these data was first checked comparing all measured gravity values with those predicted on the basis of adjacent points. In Fig. 5 one can see the points where the differences were obtained between the measured and predicted anomalies being larger than the three times of standard deviations (206 differences up), i.e. larger than the two times of standard deviations (1372 differences down), both obtained from the prediction. It is obvious that a very small number of measurements are problematic in Croatia, and the majority of such measurements are outside of our area where an additional analysis of these data will be necessary in order to find the causes.

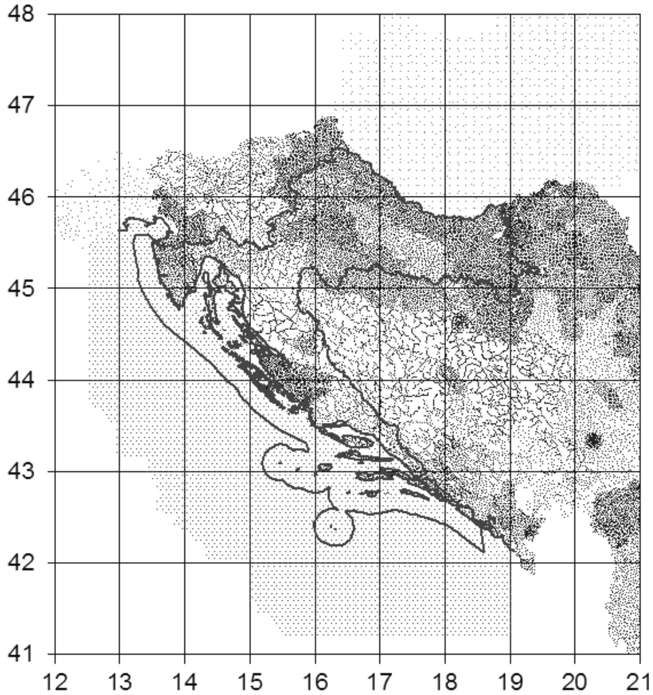

Fig. 4 New available gravity data base

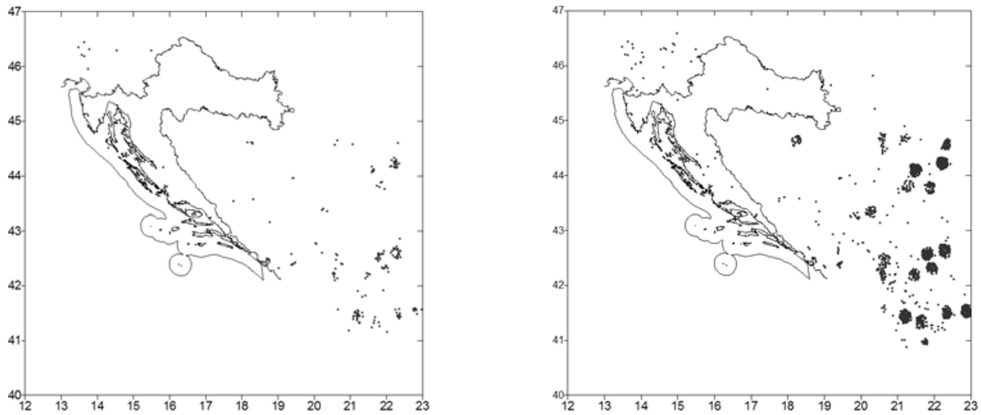

Fig. 5 Differences between measured and predicted gravity anomalies (left 206 diff. > 3·std, and right 1373 diff. > 2·std, obtained from the preduction)

5 Conclusion

Since we are now in the situation that most preparatory work has been done, determination of the new geoid solution for the territory of Croatia is expected in the nearest future, using also other methods of calculation, like FFT and integral formulas. We are also happy to be involved in the international **E**uropean **G**ravity and **G**eoid **P**roject (within IAG Commission 2) serving as a regional data and computing center. Therefore, we would like to develop a good cooperation with all surrounding countries.

References

Bašić, T. (1989). Untersuchungen zur regionalen Geoidbestimmung mit "dm" Genauigkeit, disertation (in German), Wiss. Arbeit. der Fachrichtung Vermess. der Univ. Hannover, Nr. 157.

Bašić, T. (2001). Detailed Geoid Model of the Republic of Croatia (in Croatian), *Reports of the State Geodetic Administration on Scientific and Professional Projects in the Year 2000*, Ed. Landek I., 11-22, Zagreb.

Bašić, T., M. Brkić, and H. Sünkel (1999). A New, More Accurate Geoid for Croatia. EGS XXIII General Assembly, Nice, 20-24 April 1998, In: *Physics and Chemistry of the Earth*, Part A: Solid Earth and Geodesy, Special Issue: Recent Advances in Precise Geoid Determination Methodology, I. N. Tziavos and M. Vermeer (eds.), pp. 67-72, Elsevier Science Ltd.

Bašić, T., and M. Brkić (1999). The Latest Efforts in the Geoid Determination in Croatia, 2nd Joint Meeting of the International Gravity Commission and the International Geoid Commission, 7-12 September, 1998, Trieste, *Bollettino di Geofisica Teorica ed Applicata*, Vol. 40, N. 3-4, pp. 379-386, Osservatorio Geofisico Sperimentale.

Bašić, T., and M. Šljivarić (2003). Utility Programs for Using the Data of the Official Croatian Geoid and Coordinate Transformation between HDKS and ETRS (in Croatian), *Reports of the State Geodetic Administration on Scientific and Professional Projects from the Year 2001*, Ed. I. Landek), 21-32, Zagreb.

Forsberg, R. (1984). A Study of Terrain Reductions, Density Anomalies and Geophysical Inversion Methods in Gravity Field Modeling, Dep. of Geod. Sci. and Surv., Rep. No. 355, Ohio State University, Columbus.

Hećimović, Ž. (2001). Modeling of Reference Surface of Height Systems, Ph.D. thesis (in Croatian), 1-135, Faculty of Geodesy, University of Zagreb.

Hećimović, Ž., and T. Bašić (2003). Global Geopotential Models on the Territory of Croatia (in Croatian). *Geodetski list*, 57 (80), No. 2, 73-89, Zagreb.

Hećimović, Ž., and T. Bašić (2004a). Comparison of CHAMP and GRACE Geoid Models with Croatian HRG2000 Geoid, 1st General Assembly of the European Geosciences Union, Session G9: Results of Recently Launched Missions: Champ, Envisat, Icesat, Jason-1, and Grace, Nice, France, 25-30 April 2004, poster EGU04-A-02715; G9-1WE3P-0316, Abstract in: *Geophysical Research Abstracts* (CD), Volume 6, 2004, ISSN 1029-7006.

Hećimović, Ž., and T. Bašić (2004b). Modeling of Terrain Effect on Gravity Field Parameters in Croatia, IAG International Symposium Gravity, Geoid and Space Missions (GGSM2004), 30. Aug. – 3. Sep. 2004, Porto, Portugal.

Lemoine F. G., et al. (1996). The Development of the NASA, GSFC and NIMA Joint Geopotential Model, Proceed. paper for the IAG Symposium on Gravity, Geoid, and Marine Geodesy, Tokyo.

Morelli, C., M.T. Carrozzo, P. Ceccherini, I. Finetti, C. Gantar, M. Pisani, P. Schmidt di Friedberg (1969). Regional Geophysical Study of the Adriatic Sea, *Bollettino di Geofisica Teorica ed Applicata*, Vol. XI, N. 41-42, Trieste.

Terrain Effect on Gravity Field Parameters using Different Terrain Models

Ž. Hećimović*, T. Bašić**

* Av. M. Držića 76, 10000 Zagreb, Croatia
** Department for Geomatics, Faculty of Geodesy, University of Zagreb, HR-10000 Zagreb, Kačićeva 26, Croatia

Abstract. *This paper presents the results of several analyses considering influence of terrain models on gravity field data. In the analysis are used digital elevation model (DEM) made by digitalization of topographic maps, Shuttle Radar Topography Mission Digital Terrain Elevation Data (SRTM DTED), gravity anomalies, GPS\leveling undulations and deflections of the vertical in Croatian geoid test area. To check the influence of different terrain resolutions on residual terrain model (RTM) effects on gravity anomalies and GPS\leveling undulations, the resolutions of referent terrain models 6'x7.6', 10'x15', 20'x30' and 30'x30' are used. Influence of different referent DEM resolutions on remove-restore residual fields is showing the smoothest and smallest field for resolution 20'x30'. The comparison of DEM and SRTM DTED terrain models is made to check their quality. To judge influence on gravity field considering differences of DEM and SRTM DTED terrain models, RTM effects on gravity anomalies, GPS\leveling undulations and vertical deflections are modeled.*

Keywords. *DEM, SRTM DTED, terrain model resolution, RTM effect.*

1. Introduction

CHAMP and GRACE and further GOCE gravity models are defining new standards in gravity field modeling in global (long wave) and regional (middle wave) scale. Topographic, short wave, influence on gravity is becoming more and more important. However, the latest GRACE models are containing topographic (short wave) structure of gravity field, see Hećimović and Bašić (2004). Different characteristics of Croatian topography, on the coast very slope, high mountains and in the eastern part flat area, can be clearly recognized in the GRACE models, see Hećimović et al. (2004). Modeling of short wave gravity field, which is caused by topography and masses densities variability, is becoming the primary problem in modeling regional and local gravity field.

To investigate influence of different terrain models on gravity anomalies, deflections of the verticals and GPS\leveling undulations the test area in the northern part of Croatia has been chosen. To get a insight into the terrain resolution influences, it is interesting to analyze the influences of different terrain model resolutions on RTM gravity anomalies and RTM GPS\leveling undulations. Terrain models with the resolutions 6'x7.6', 10'x15', 20'x30' and 30'x30' are used in investigations. For every resolution, the statistical characteristics are analyzed as well the main characteristics of empirical covariance functions.

Besides the used DEM that is based on national topographic information, global topographic information, e.g. SRTM DTED is also publicly available now. Comparing of DEM and SRTM DTED we obtain the independent quality control of available topographic information. Calculating RTM influences on gravity functionals using DEM and SRTM DTED gives us the possibility to check direct influence on gravity field values as well on geoid using independent sources of topographic information. It gives us the possibility to judge systematic errors in topographic models on gravity field values.

2. Croatian Geoid Test Area

Croatian political borders have got an unpleasant shape for modeling earth gravity field. The rectangular test area (45.0° < φ < 46.5°, 15.5° < λ < 17.5°) is chosen for numerical analysis (see Figure 1).

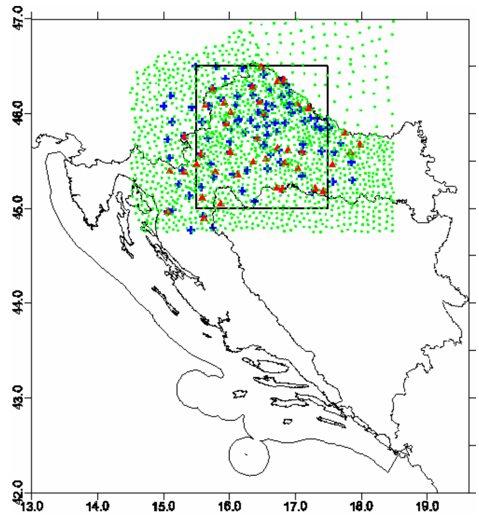

Fig. 1 Croatian geoid test area with point free air anomalies (green points), deflections of the verticals (blue crosses) and GPS\leveling data (red triangles).

There are point free air anomalies, deflections of the verticals, GPS\leveling data and different terrain models used in the analysis. Because of inconvenient Croatian shape for modeling earth gravity field, the data about the territory of other countries are also used.
To separate different gravity fields' wavelengths, and analyze smaller gravity signal, the remove-restore procedure on gravity field functionals L_i is used (Denker (1988)). Wavelengths are separated considering different sources of data after

$$L_i(T) = L_i(T_{GPM}) + L_i(T_M) + L_i(T_{RTM}) \,. \tag{1}$$

The theoretical background to mode RTM effect can be found in Forsberg (1984a) or Forsberg and Tscherning (1981).
The main statistical characteristics of 1491 point free air anomalies are given in Table 1.

Table 1. The main statistical characteristic of gravity anomalies

	$\Delta g_{FREE\ AIR}$ [mGal[1]]	Δg_{EGM96} [mGal]	Δg_{RTM} [mGal]	$\Delta g_{REZID.}$ [mGal]
Mean	31.85	23.76	-0.86	12.70
St. dev.	23.46	9.11	10.31	12.76
Min.	-40.76	-3.06	-43.88	-22.24
Max.	135.22	47.51	74.61	64.26

From available GPS\leveling dataset, only 41 reliable GPS\leveling undulations in the test area are used. The main statistical characteristics of GPS\leveling data are shown in Table 2.

[1] 1 mGal = $1 \cdot 10^{-5}$ m·s^{-2}

Table 2. The main statistical characteristic of GPS\leveling undulations

	$N_{GPS\backslash LEV.}$ [m]	N_{EGM96} [m]	N_{RTM} [m]	$N_{REZID.}$ [m]
Mean	45.16	46.46	-0.01	-1.29
St. dev.	0.48	0.38	0.05	0.26
Min.	44.03	45.71	-0.07	-1.83
Max.	46.44	47.07	0.14	-0.68

RTM undulations are indicating small influence on the geoid height changes, and the mean of undulations is indicating datum differences in the first approximation.
Deflections of the vertical components are used in 91 points. They are behaving irregularly in amplitude and directions. The main statistical characteristics of deflections of the vertical components are given in Tables 3a and 3b.

Table 3a. The main statistical characteristic of meridian component of deflections of the vertical

	$\xi_{MEAS.}$ ["]	ξ_{EGM96} ["]	ξ_{RTM} ["]	$\xi_{REZID.}$ ["]
Mean	0.64	0.29	0.02	0.33
St. dev.	3.61	1.64	1.28	2.35
Min.	-10.46	-4.96	-2.92	-7.16
Max.	11.02	2.95	4.70	6.18

Table 3b. The main statistical characteristic of longitude component of deflections of the vertical

	$\eta_{MEAS.}$ ["]	η_{EGM96} ["]	η_{RTM} ["]	$\eta_{REZID.}$ ["]
Mean	1.55	1.32	-0.29	0.52
St. dev.	3.07	1.61	1.57	2.11
Min.	-10.18	-4.85	-5.36	-4.62
Max.	7.56	4.75	5.76	4.96

The mean values for gravity anomalies and undulations are indicting datum differences that should be considered before geoid modeling.

3. Terrain Models

The terrain models are used for modeling of terrain influence on gravity field DEM of different resolutions and new SRTM DTED. Fine DEM is made by digitizing the maps in the scale 1:25000. Rough and referent terrain models are made by resampling of the fine DEM model. SRTM DTED for area 12 (USGS EROS Data Center (2004)) in the resolution 3”x 3” is used as a separate fine terrain model. Coverage of terrain models is shown on Figure 2.

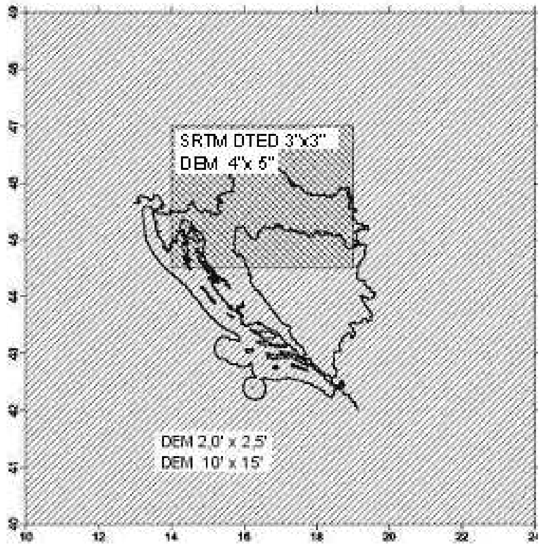

Fig. 2 Terrain models.

- fine SRTM DTED, 3”x 3” in area 44.5° < φ < 47.0°, 14.0° < λ < 19.0°,
- fine DEM, 4”x 5” in area 44.5° < φ < 47.0°, 14.0° < λ < 19.0°,
- rough DEM, 2.0’x 2.5’ in area 40.0° < φ < 49.0°, 10.0° < λ < 24.0°,
- referent DEM, 10’x 15’ in area 40.0° < φ < 49.0°, 10.0° < λ < 24.0°.

4. Analysis of Influence of Terrain Model Resolution Changes on Gravity Field Functionals

To judge the influence of terrain model resolution changes on modeling RTM effect, a resampling of referent DEM is made. In the analysis there are resolutions 6’x 7.5’, 10’x 15’, 20’x 30’ and 30’x 30’ used. RTM effect on gravity anomalies and GPS\leveling undulations is modeled using TC program (Forsberg (1984b)). Constant terrain density of 2670 kg·m^{-3} is used. The main statistical characteristics for RTM gravity anomalies and RTM GPS\leveling undulations are given in Tables 4 and 5.

Table 4. The main statistical characteristics of RTM gravity anomalies using different referent DEM resolutions

	6’ x 7.5’ Δg_{RTM} [mGal]	10’x15’ Δg_{RTM} [mGal]	20’x30’ Δg_{RTM} [mGal]	30’x30’ Δg_{RTM} [mGal]
Mean	-3.72	-4.17	-4.62	-8.59
St. dev.	11.42	13.47	15.67	19.12
Min.	-77.06	-74.58	-65.98	-74.40
Max.	61.31	77.69	89.98	92.57

Table 5. The main statistical characteristics of RTM GPS\leveling undulations using different referent DEM resolutions

	6' x 7.5' N_{RTM} [m]	10'x 15' N_{RTM} [m]	20'x 30' N_{RTM} [m]	30'x 30' N_{RTM} [m]
Mean	0.01	-0.01	-0.03	-0.50
St. dev.	0.03	0.07	0.15	0.67
Min.	-0.08	-0.23	-0.40	-1.91
Max.	0.31	0.57	0.89	0.95

Increasing resolution of the referent DEM is causing the increase of standard deviations of RTM gravity anomalies and RTM GPS\leveling undulations. With increasing referent DEM resolution the mean values of RTM gravity anomalies are increasing regularly, and the data are deflecting from centering conditions. The mean values of RTM GPS\leveling undulation are increasing regularly up to the resolution 30'x30', where big jump can be observed.

5. Analysis of Influence of Terrain Model Resolution Changes on Empirical Covariance Function

Covariance function is essential for gravity field modeling in collocation techniques. To judge the influence that the changing of referent DEM resolution makes on empirical covariance function of free air anomalies, residuals of free air anomalies are calculated with different RTM values considering changing of resolutions of DEM. In Table 6 the main statistical characteristics of gravity anomalies residual fields are presented.

Table 6. The main statistical characteristics of free air anomalies residual fields in the middle wavelength calculated using different resolutions of referent DEM

	6' x 7.5' Δg_M [mGal]	10'x15' Δg_M [mGal]	20'x30' Δg_M [mGal]	30'x30' Δg_M [mGal]
Mean	11.85	12.22	12.67	16.64
St. dev.	18.37	15.68	12.76	15.66
Min.	-48.15	-27.38	-22.27	-21.15
Max.	90.77	72.92	64.19	81.08

The residual anomalies calculated by RTM effect with 20'x30' referent DEM resolution are giving the smoothest and the smallest residual fields. The mean values of residuals are bigger because of the consistency of gravimetric datums.
The associated variance for the same referent DEM resolution is also the smallest one (see Table 7).

Table 7. Variances of residual free air anomalies for different resolutions of referent DEM

DEM resolution	Variance [mGal^2]
6' x 7.5'	407.725
10' x 15'	368.381
20' x 30'	308.050
30' x 30'	535.461

Using these statistical data as criteria, referent DEM of resolution 20'x30' gives the best results, e.g. this referent DEM gives in remove-restore procedure the smallest and the smoothest residual field for geoid modeling.

6. SRTM Digital Terrain Elevation Data

NASAs Shuttle Radar Topography Mission (SRTM) made in 11 days Space Shuttle flight has scanned nearly a global Earths topography. Space borne Imaging Radar-C (SIR-C) sensors formed an interferometer with a 60-meter long baseline. The data have the potential to provide almost global elevation data in up to 30 m resolutions. SRTM Digital Terrain Elevation Data (DTED) are unrestricted for the area anywhere on the globe in 3" (~100m) resolution, but the resolution 1" (~30m) is publicly available only for the United States and its territories.
SRTM DTED terrain data have voids mainly caused by SIR-C radar shadows in rough terrain. To fill SRTM DTED voids GTOPO30 the terrain model is used (see Figure 3).

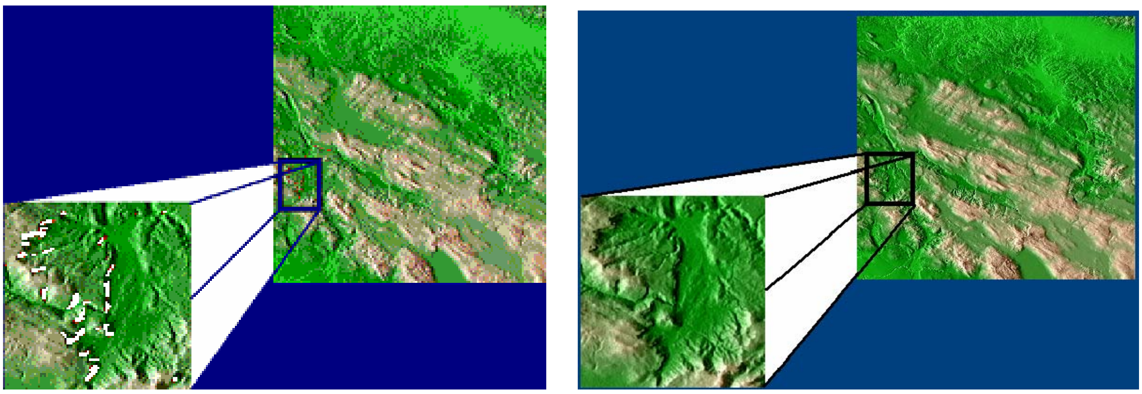

Fig. 3. a) Source SRTM DTED with voids (white holes) and b) SRTM DTED terrain model treated with GTOPO30.

The problem in using SRTM DTED terrain model is that it is related to radar reflecting surface. It does not have to be the primary terrain, but the top of the trees and buildings respectively.

7. Comparison of DEM and SRTM DTED Terrain Models

To judge the quality of DEM and SRTM DTED terrain models in test areas, SRTM DTED is resampled in fine DEM raster of 4"x5". The main statistical characteristics of DEM and SRTM DTED terrain models and their differences are shown in Table 8, and differences are presented on Figure 4.

Table 8. The main statistical characteristics of DEM and SRTM DTED terrain models and their differences

	H_{DEM} [m]	$H_{SRTM\ DTED}$ [m]	Diff. H_{DEM} - $H_{SRTM\ DTED}$ [m]
Mean	229	228	1
St. dev.	181	182	27
Min.	1	44	-309
Max.	1796	1770	357

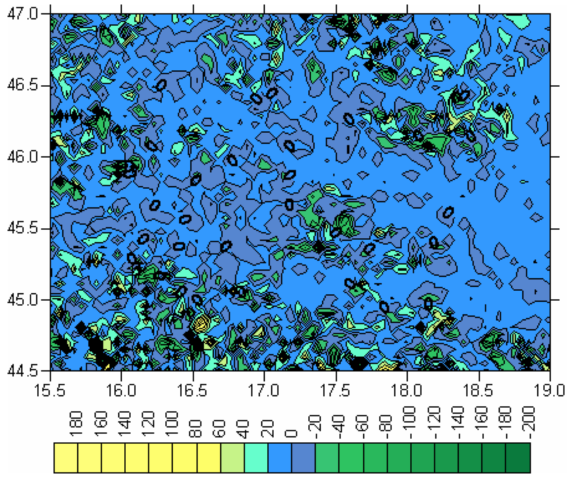

Fig. 4 DEM and SRTM DTED terrain model differences [m].

DEM and SRTM DTED differences have mean value of 1 m. It indicates, in the first approximation, terrain model datum differences. It is caused by datum differences between old Croatian height system datum defined by costal tidal station in Trieste and global geoid EGM96.
This value is showing good agreement with previous comparisons of Croatian height system and global geopotential models, see Hećimović (2001), Hećimović and Bašić (2002). In these investigations there are 121 GPS\leveling undulations well distributed over Croatian territory used. They showed differences between Croatian height system datum and global geoid EGM96 of 1,37 m, and that value has good agreement with the value obtained with DEM and SRTM DTED in table 8.

8. Influence of DEM and SRTM DTED Differences on RTM Gravity Functionals

To check influence of different topography data solutions on gravity field, RTM effects are modeled using DEM and SRTM DTED terrain models. The main statistical characteristics of RTM gravity anomalies for DEM and SRTM DTED terrain models and their differences are presented in Table 9, and on the Figure 5 the differences can be seen.

Table 9. The main statistical characteristics of RTM gravity anomalies for DEM and SRTM DTED terrain models and their differences

	Δg RTM DEM [mGal]	Δg RTM SRTM DTED [mGal]	Diff. Δg RTM DEM – Δg RTM SRTM DTED [mGal]
Mean	-4.74	-4.29	0.13
St. dev.	12.44	13.52	0.83
Min.	-74.58	-74.58	-7.74
Max.	67.37	78.91	6.36

Differences have small bias of 0.13 mGal, as well small dispersion, e.g. standard deviation.

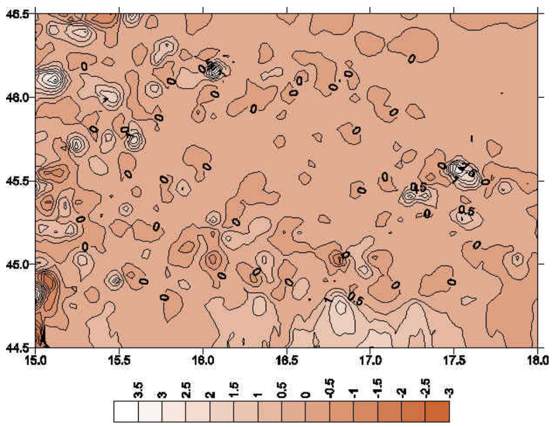

Fig. 5 Differences of DEM and SRTM DTED RTM gravity anomalies [mGal].

The main statistical characteristics of RTM GPS\leveling undulations from DEM and SRTM DTED terrain models and their differences are given in Table 10. The main statistical characteristics and Figure 6 indicate that the influence of different terrain models on RTM GPS\leveling undulations is small.

Table 10. The main statistical characteristics of RTM GPS\leveling undulations for DEM and SRTM DTED terrain models and their differences

	$N_{RTM\ DEM}$ [m]	$N_{RTM\ SRTM\ DTED}$ [m]	Diff. $N_{RTM\ DEM}$ - $N_{RTM\ SRTM\ DTED}$ [m]
Mean	-0.01	-0.01	-0.00
St. dev.	0.06	0.06	0.01
Min.	-0.07	-0.08	-0.02
Max.	0.14	0.15	0.01

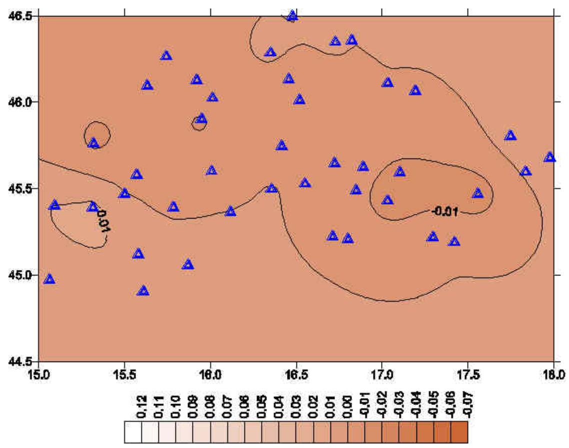

Fig. 6 Differences of DEM and SRTM DTED RTM GPS\leveling undulations [m].

RTM meridian component of deflections of the vertical of DEM and SRTM DTED terrain models and their differences (see Table 11 and Figure 7) are showing small influence of different terrain models. On the Figure 7 it can be seen that the influence is increasing in higher areas.

Table 11. The main statistical characteristic of RTM meridian component of deflections of the vertical for DEM and SRTM DTED terrain models and their differences

	$\xi_{RTM\ DEM}$ [”]	$\xi_{RTM\ SRTM\ DTED}$ [”]	$\xi_{RTM\ DEM}$ - $\xi_{RTM\ SRTM\ DTED}$ [”]
Mean	0.02	0.32	-0.30
St. dev.	1.28	1.40	0.56
Min.	-2.92	-2.33	-2.83
Max.	4.70	4.99	0.45

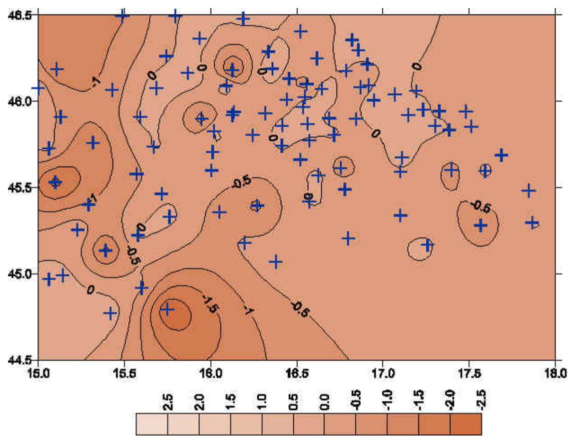

Fig. 7 Differences of DEM and SRTM DTED RTM meridian component of deflections of the vertical [arc sec].

Similar as by RTM meridian component, RTM longitudinal component of deflections of the vertical of DEM and SRTM DTED terrain models and their differences (see Table 12 and Figure 8) show small influence of different terrain models. A small increase of influence can be recognized in higher areas.

Table 12. The main statistical characteristic of RTM longitude component of deflections of the vertical for DEM and SRTM DTED terrain models and their differences

	η RTM DEM [”]	η RTM SRTM DTED [”]	η RTM DEM - η RTM SRTM DTED [”]
Mean	-0.29	-0.04	-0.25
St. dev.	1.58	1.48	0.56
Min.	-5.35	-5.03	-2.52
Max.	5.76	6.17	0.58

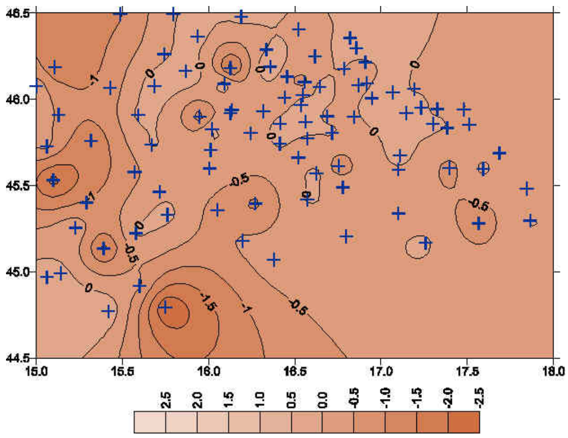

Fig. 8 Differences of DEM and SRTM DTED RTM longitudinal component of vertical deflections [arc sec].

9. Conclusions

The influence of different referent terrain model resolutions on RTM effect for gravity anomalies and GPS\leveling undulations is analyzed for resolutions 6’x7.6’, 10’x15’, 20’x30’ and 30’x30’. The increasing of DEM resolutions influences RTM gravity anomalies standard deviations from 11.42 mGal to 19.12 mGal and mean values from -3.72 mGal to -8.59 mGal. The mean values of RTM GPS\leveling undulations change along with the increasing terrain resolution from 0.01 m to -0.50 m, and standard deviations from 0.03 m to 0.67 m. The changes for RTM undulations are regular up to resolution 30’x30’ where a big jump can be observed. Despite of this irregularity, influence of different resolutions on RTM effect is significant and regular.

The changing of referent DEM resolution affects the covariance function and modeling of gravity signal in collocation technique. Anomalies have the smallest variance for 20’x30’ terrain resolution and residual field of gravity anomalies has the best results in comparison with the results when other terrain resolutions are used for modeling RTM effects. Terrain model of this resolution is giving the smoothest and the smallest residual field for modeling gravity field. Considering the criteria of the smallest variance and the best main statistical characteristic of remove-restore residual field, the optimal resolution of DEM can be found. The smoothest and the smallest residual gravity field are wanted by gravity field modeling using collocation technique.

To judge quality of different terrain models, DEM and SRTM DTED models are compared in the test area. They have vertical bias of 1 m, that is indicating datum differences in the first approximation, and the standard deviation, which is characterizing dispersion of terrain models differences, is 27 m.

To analyze the influence of differences of DEM and SRTM DTED terrain models on gravity field functionals, RTM-effects on gravity anomalies, GPS\leveling undulations and vertical deflections are modeled, and differences are analyzed. Differences of DEM and SRTM DTED terrain models are causing RTM effect on gravity anomalies that have the mean value of 0.13 mGal and standard deviation of 0.83 mGal, RTM GPS\leveling undulations have the mean value of 0.00 m and standard deviation of 0.01 m, meridian vertical deflection components have the mean value of -0.30” and standard deviation of 0.56” and longitudinal vertical deflection component have the mean value of -0.25” and standard deviation of 0.56”. DEM and SRTM DTED terrain models discrepancies cause small differences in geoid modeling data, but they should be considered.
The problem that SRTM DTED is related to radar reflecting surface and not to terrain, should be considered in geoid modeling with centimeter accuracy.

References

Denker, H. (1988). Hochauflösende regionale Schwerefeldbestimmung mit gravimetrischen und topographischen Daten. *Wissenschaftlichen Arbeiten der Fachrichtung Vermessungswesen der Universität Hannover*, Nr. 156, Hannover

Forsberg, R., C. C. Tscherning (1981): The Use of Heights Data in Gravity Field Approximation. *Journal of Geophysical Research* (86), 7843-7854

Forsberg, R. (1984a). Local Covariance Functions and Density Distributions. *The Ohio State University, Department of Geodetic Science and Surveying*, Report No. 356, Ohio

Forsberg, R. (1984b). A Study of Terrain Reductions, Density Anomalies and Geophysical Inversion Methods in Gravity Field Modeling. *Report of the Department of Geodetic Science and Surveying*, Report No. 355, Ohio

Hećimović, Ž. (2001): Modeliranje referentne plohe visinskih sustava. Dissertation. University of Zagreb Faculty of Geodesy (in Croatian)

Hećimović, Ž., T. Bašić (2002). Global geopotential models on the territory of Croatia. *Geodetski list*, 57 (80), Nr. 2, 73-89 (in Croatian)

Hećimović, Ž., T. Bašić (2004). Comparison of CHAMP and GRACE geoid models with Croatian GRG2000 geoid. 1st General Assembly European Geosciences Union (EGU), Nice, France, from 25 - 30 April 2004. Poster presentation. *Geophysical Research Abstracts*, Vol. 6, 02715, 2004. SREef-D: 1607-7962\EGU04-A-02715. European Geosciences Union

Hećimović, Ž., B. Barišić, I. Grgić (2004). European Vertical Reference Network (EUVN) considering CHAMP and GRACE gravity models. Symposium of the IAG Subcommission for Europe. European Reference Frame - EUREF 2004, Bratislava, Slovakia, 2 - 5 June 2004

USGS EROS Data Center (2004). SRTM DTED Level 1, Area 12, CD-ROM